

國立交通大學

材料科學與工程學系

博士論文

鎳鐵圖形化微結構中
自旋傳輸及磁化翻轉行為之研究

Study on Spin Transport and Magnetic Reversal
Behavior in Patterned NiFe Structure



研究生：陳東呈

指導教授：姚永德 博士
韋光華 博士

中華民國 100 年 7 月

中文摘要

本論文的研究以電子束微影及舉離技術，製作次微米級和奈米級的圖形化磁性薄膜樣品。並藉由磁力顯微儀的量化分析及磁阻量測，來研究該圖形化磁性薄膜的磁化翻轉以及自旋傳輸的現象，商業化的磁性穿隧界面元件也在溫度變化的條件下量測其穿隧磁阻的變化。

在一個由兩段不同線寬所組成的磁性長線中，磁力顯微儀的分析結果顯示，不同區域的磁化翻轉現象能被各別地分開並互相比較。寬度越寬的線段，其端點雜散磁力越強；相反地，越細的線段其端點的矯頑場越強，這導因於形狀異向性的效應，也因此在此頸部(粗細線段交接處)的矯頑場易受影響，此影響來自於兩線段的磁化彼此相向時的競爭，在頸部處兩同極性磁極的互斥結果使得此處的矯頑場變弱。在磁性穿隧界面元件的熱效應研究中，磁阻變化率在 140°C 時，降到約為在室溫的 87%。這意味著該元件在一般使用狀況中能適應儀器或電器所產生略高於室溫的溫度 ($60\text{--}80^{\circ}\text{C}$)，而數據顯示在該溫度此元件之磁阻變化率仍能保有在室溫的 90-95%。我們也製作了三層的環形自旋閥及單層的磁性環並量測其磁阻，在單層環中，由電流所驅動的磁區壁移動，其所需的臨界電流密度約 $1.5 \sim 3.5 \times 10^7 \text{ A/cm}^2$ ；在三層環形自旋閥的磁化翻轉過程中，所研究的元件尺寸極可能落在渦旋態和洋蔥態臨界的邊界上。因為觀察到的數據顯示某一暫穩態隨機地出現，該暫穩態是軟磁層處於渦旋態，而硬磁層處於洋蔥態。由於單層及三層的量測方式皆無法提供明確辨認渦旋方向的方法，故我們接著製作橫向的自旋閥，並利用其非局域的量測方式來判斷渦旋態的旋向。此非局域的橫向自旋閥直接探測銅導線中，來自鐵磁環因自旋注入所產生的自旋堆積訊號，也因此能得知鐵磁環的旋向。經由數據推算，該橫向自旋閥在銅質擴散通道裡的自旋級化率約為 2%。而在橫向自旋閥的另一種量測中，局域的量測方式產生一個反對稱於零磁場的訊號，幾乎是等同於一般磁滯曲線的訊號。該訊號顯然來自於磁性跟非磁性交接介

面的電阻訊號。在一系列有系統的尺寸變化研究下，數據結果顯示該訊號來自於磁性跟非磁性交接介面的異常霍爾效應。



ABSTRACT

Submicron- and nano-sized magnetic patterns were fabricated by e-beam lithography with lift-off techniques. The magnetoresistance (MR) measurements and quantitative analysis of magnetic force microscopy (MFM) were used to investigate the spin transports and magnetic reversal behaviors of these magnetic patterns. The commercial magnetic tunnel junctions (MTJs) were also measured at various temperatures to observe its thermal effects.

The MFM were used to investigate a permalloy (Py) strip including two parts with different widths. The results indicated that the magnetic behaviors in different sections of the strip can be separated. The intensity of the phase-shift in the wider end is stronger than that in the narrower one. In contrast, the coercive force in the narrower end (9 Oe) is larger than that in the wider one (8 Oe). This is due to a strong anisotropic effect, and thus the H_c in the neck section could be strongly affected by the competition of the head-to-tail magnetic configurations in the two parts of the strip wire. This results in a small H_c in the neck section.

For the thermal effect measurement of the MTJs, the MR ratio at 140 °C remained roughly 87% of that at room temperature. The operational temperature of electronic equipments is generally around 60–80 °C and the MR ratio of the MTJs at such temperatures be preserved in a considerable portion (90–95%) of that at room temperature.

Single-layered and tri-layered spin valve rings were investigated by MR measurements. The critical current density of current-induced domain wall motion in the single-layered Py ring is about $1.5 \sim 3.5 \times 10^7$ A/cm². With the present size, the tri-layered spin valve was possibly in the critical boundary between the formations of vortex and onion. Within this state, the soft ring was in vortex state and the hard one

was in the forward onion state.

The nonlocal lateral spin valve (NLSV) devices were also constructed to detect the vortex chirality of the ring. The spin polarization induced in Cu diffusive channel of the NLSV devices in the present work was estimated at about 2%. The spin signals were also enhanced by shortening the distance of the diffusive channel.

Finally, we investigated the Cu-Py cross structure through which charge current flows and the resistance of the contact region. The concept of this structure was from the NLSV studies mentioned above. When choosing one voltage electrode as the spin injector itself, the probe arrangement was no longer the nonlocal geometry, and hence the signal from the local contact region was sensed. This signal exhibited a magnetic hysteretic loop, i.e., odd-asymmetric roughly equals to the zero field. We found the variation of the odd-asymmetric signals directly related to the switching of the spin injector at the contact region (the Cu-Py cross). It was attributed to the anomalous Hall effect of the injector at the contact region and the argument was supported by the results of size dependent investigation.

誌謝

It's a long road! 姚永德教授的教誨與鼓勵讓我瞭解到，處境再怎麼艱困總會有轉圜的餘地，永遠都會有別條路可以走。姚老師的教導讓我深深體會，自己一個人轉圈子總是很辛苦，主動積極地透過交流尋求解決之道才是學術研究的精神，也是做人處事的原則。這幾年來承蒙李尚凡老師、劉鏞老師的支持與照顧，以及意見的提供著實讓我受惠不少。實驗室的伙伴們，于淳學長、斯衍、凱文、典蔚、呂圭、良君、昱哲，你們的關懷、鼓勵與實驗上的幫助與意見交流讓東呈得以學到很多東西和觀念。學無止境，我相信這句話不只用在做學問做研究，更重要的是人與人之間相處的態度和關懷，都是必須終身隨時隨地學習的。這幾年受到很多的幫忙，也讓我不斷地成長。感謝每個機緣下所獲得的幫助和體會。再次感謝姚老師的支持與鼓勵，讓我受益匪淺。



Contents

中文摘要	I
Abstract	III
誌謝	V
Contents	VI
List of Figures	VIII
List of Tables	XV
LIST of Symbols	XVI
Chapter 1 Introduction	1
Chapter 2 Basic Theory and Phenomena	8
2.1 Magnetic Domain and Domain Wall	8
2.2 Magnetic Tunnel Junction (MTJ) and Tunnel Magnetoresistance (TMR)	11
2.2.1 Julliere's Model	12
2.2.2 Slonczewski's model	13
2.2.3 Temperature Dependence of TMR	14
2.2.4 Voltage Dependence of TMR	15
2.3 AMR and Hall Effect	19
2.4 Spin Injection and Accumulation in Lateral Spin Valve	22
2.5 Magnetic Reversal Process of Ferromagnetic Ring	24
Chapter 3 Experiments	27
3.1 Sample Preparation	27
3.2 Surface probed by Atomic Force Microscopy (AFM) and Magnetic Force Microscopy	29
3.3 Magnetoresistance (MR) measurement	30
Chapter 4 Results and Discussion	31
4.1 Quantitative analysis of magnetic reversal in patterned strip wire by magnetic force microscopy	31
4.1.1 Fabrication and measurement of the Permalloy (Py) strip	31
4.1.2 AFM/MFM image at a positive field	32
4.1.3 Observation of the phase magnitude for full loop	34
4.1.4 Evaluation of the individual sections	36
4.1.5 Lists of the phase magnitudes and MFM images	38
4.2 Thermal effects on magnetoresistance of magnetic tunnel junction	45

4.2.1 Structure of magneto tunnel junction (MTJ) and measurement	45
4.2.2 Temperature-dependent TMR measurement	46
4.2.3 Bias-dependent TMR measurement	51
4.3 Magnetic reversal process and current-induced domain wall motion in ferromagnetic curve- and ring- shape structure	63
4.3.1 AMR behavior and current-induced domain wall motion of single-layered FM ring	63
4.3.2 MR behavior in FM/N/FM tri-layered-ring spin valve	66
4.4 Determining vortex chirality in ferromagnetic ring by lateral spin valve	71
4.4.1 Structure of ring-wire lateral spin valve	71
4.4.2 AMR measurement of the individual ring	73
4.4.3 NLSV measurement and comparison with AMR result	75
4.4.4 Comparison with the wire spin injector	81
4.4.5 Vortex chirality detection by local lateral spin valve	82
4.5 Observation of Hall-like signal in all-metal lateral spin valve	87
4.6 Observation of Anomalous Hall effect in Cu-Py-crossed structure with in-plane magnetization	90
4.6.1 Proposal of Cu-Py-crossed four-terminal Hall device	90
4.6.2 Observation of size-dependent ΔR	92
4.6.3 Proposal of the detailed geometry explaining the origin of ΔR	95
4.6.4 Estimation of AHE in Py	97
4.6.5 Estimation of ordinary Hall effect in Cu	98
4.6.6 Estimation of inverse Spin Hall effect (ISHE) in Cu	99
Chapter 5 Conclusions	101
Reference	103
List of Publication	112

List of Figures

2.2-1	11
First observation of reproducible, large room temperature MR in a CoFe/Al ₂ O ₃ /Co MTJ. The arrows indicate the relative magnetization orientation in the CoFe and Co layers. After Moodera <i>et al.</i> [109].	
2.2-2	14
Spin polarization of the tunneling conductance as a function of the normalized potential barrier height for various values of k/k^- . After Slonczewski [19].	
2.2-3	15
Temperature dependence of TMR for a Co/Al ₂ O ₃ /Co MTJ (circles) along with a fit to the model of Shang <i>et al.</i> [28] (solid line).	
2.2-4	16
Original demonstration of the tunneling magnetoresistance effect. The relative conductance change due to an applied magnetic field versus applied bias in a Fe/Ge/Co junction at 4.2 K. After Julliere [17].	
2.2-5	18
The bias dependence of (a) the dI/dV in the AP (solid line) and P (dotted line) configurations, and (b) TMR. Arrows mark the local minima in the AP and P configurations. (c) The energy-dependent DOS function $[N(E_x)]$ for P (squares) and AP (circles) configurations. (d) The fitted energy-dependent DOS for FeNi majority (solid squares), FeNi minority (solid circles), Co majority (open squares), and Co minority (open circles). After Xiang <i>et al.</i> [38-39].	
2.3-1	20
Illustration of the Hall Effect.	
2.3-2	21
Hall effect in ferromagnetic materials. After Volmera <i>et al.</i> [113].	
2.4-1	22
Illustration of DOS in a ferromagnet (a) and nonmagnet (b).	
2.4-2	23
Illustrations of the spin splitting in the chemical potential induced by spin injection.	
2.4-3	23
(a) SEM image of the mesoscopic spin valve junction. The two wide horizontal strips are the ferromagnetic electrodes Py1 and Py2. The vertical arms of the Cu cross (contacts 3 and 8) lie on top of the Py strips; the horizontal arms of the Cu cross form contacts 5 and 6. Contacts 1, 2, 4, 7 and 9 are attached to Py1 and Py2 to allow four terminal AMR measurements of the Py electrodes. (b)	

	Schematic representation of the non-local measurement geometry. Current is entering from contact 1 and extracted at contact 5. The voltage is measured between contact 6 and contact 9. (c) The results of nonlocal measurements. Upper curve: An increase in resistance is observed, when the magnetization configuration is changed from parallel to anti-parallel. The solid (dashed) lines correspond to the negative (positive) sweep direction. Middle and bottom curves: The minor loops. After Jedema [45].	
2.5-1		25
	Reversal process of a ferromagnetic ring. Switching sequence is from left to the right sides. The small circles indicate domain walls. The left ring is the first “onion” state also named “forward onion”. Vortex state (middle) can either be CW or CCW. The right is the reverse onion state.	
2.5-2		25
	SEM micrographs of rings (a) before and (b) after deposition. After Rothman, et al. [94]. (c) and (d) Typical in-plane MOKE hysteresis loops measured on rings with the same outer and inner diameter of 700 nm and of 300 nm, respectively, but for different thickness of (c) 50 nm and (d) 20 nm. (i) and (ii) represent the forward and vortex state. (e) and (f) Calculated hysteresis loops. After Li, et al. [116].	
2.5-3		26
	Transverse MR curves of Permalloy ring obtained by (a) theoretical and (b) experimental methods. The spatial relationship between the domains and leads is shown in the inset. The metastable states observed in the sweep-down process are schematically represented in the lower part of each figure. After Lai [101].	
3.1-1		28
	SEM image of the pad substrate. There are 16 contact pads (labeled by numbers) on a chip substrate. The four rings at the center are magnetic patterns.	
3.2-1		29
	Schematic illustration of AFM measurement system.	
4.1-1		31
	SEM image of the pattern with different widths of strip wire.	
4.1-2		33
	AFM/MFM image and MFM magnitude of phase. (a) AFM image (upper), MFM image (middle) and a profile (lower) of line scan in MFM image which was observed at a 140 Oe field which was initially at 250 Oe and varied to –250 Oe. (b) A schematic diagram of the magnetic configuration in accordance with that in (a).	

4.1-3	35
Phase magnitude for full loop and MFM image at a negative field. (a) Magnetic hysteresis loops (upper) for different local sections presented in values of phase; its zoom in (lower). (b) Schematic diagram of the configuration of the magnetization in the magnetic process of -20 to -200 Oe. (c) MFM image (upper) at -200 Oe and profile (lower) of the line scan in the MFM image.	
4.1-4	36
Phase Intensity (absolute value) varying with distance in the pattern near the magnetic saturation ($20 \sim 200$ Oe and $-20 \sim -200$ Oe).	
4.1-5	37
The switching field (or coercive force) H_c for each individual local section.	
4.1-6	38
List of phase magnitudes at different field (a) ~ (d) for $+250$, $+230$, $+200$, and $+180$ Oe.	
4.1-6	39
List of phase magnitudes at different field (e) ~ (l) for $+160$, $+140$, $+120$, $+80$, 40 , 0 , -10 , and -15 Oe.	
4.1-6	40
List of phase magnitudes at different field (m) ~ (q) for -20 , -25 , -30 , -35 , and -45 Oe.	
4.1-7	41
List of AFM/MFM images at different field: $+250$, $+230$, $+200$, and $+180$ Oe.	
4.1-7	42
List of AFM/MFM images at different field: $+160$, $+140$, $+120$, and $+100$ Oe.	
4.1-7	43
List of AFM/MFM images at different field: $+80$, 40 , 20 , 0 , -10 , and -15 Oe.	
4.1-7	44
List of AFM/MFM images at different field: -20 , -25 , -30 , -35 , and -45 Oe.	
4.2-1	46
Layered structure and lateral size of the MTJ cell.	
4.2-2	47
Typical TMR minor loops measured at 50 mV and room temperature.	
4.2-3	48
Temperature dependence of TMR loop.	
4.2-4	48
Temperature dependence of TMR ratio.	
4.2-5	49
Temperature dependence of resistance for P and AP configuration.	

4.2-6	49
Comparison of ΔR and MR %.	
4.2-7	50
Coercivities variation with temperature. Left: original value. Right: normalized value.	
4.2-8	50
Annealing effect on resistance.	
4.2-9	51
Annealing effect on MR ratio.	
4.2-10	52
Series of bias-dependent MR loops. (a)~(d) for bias voltage of 5 mV ~ 250 mV.	
4.2-10	53
Series of bias-dependent MR loops. (e) ~ (j) for bias voltage of 300 mV ~ 1.2 V.	
4.2-10	54
(k) full range.	
4.2-11	55
I-V curve for the MTJ device measured at 25°C .	
4.2-12	55
Dynamic conductance dI/dV . Derived from Figure 4.2-11 by differentiating I with V.	
4.2-13	57
Bias dependence of resistance.	
4.2-14	57
Bias dependence of ΔR and MR ratio.	
4.2-15	58
I-V curve dependence on temperature. (a) Full range (b) zoom in range from 0.4 V to 0.8 V.	
4.2-15	59
(c) zoom in range from -0.4 V to -0.8 V.	
4.2-16	59
Temperature dependence of dynamic conductance.	
4.2-17	60
Temperature dependence of resistance.	
4.2-18	60
Temperature dependence of MR ratio.	
4.2-19	61
Comparison between positive and negative voltage polarities of dynamic conductance.	

4.2-20	62
MR ratio dependence on temperature and bias voltage.	
4.3-1	63
AMR measurement of a single-layered Py ring with thickness 40 nm and width 225 nm. The measuring current was 10 μ A at room temperature. The inset is the SEM image of the sample and the direction of applied field is indicated by the double-head arrow.	
4.3-2	64
The AMR minor loop. The arrows indicate the direction of field sweeping.	
4.3-3	65
Field-dependent current-induced domain wall motion measurement.	
4.3-4	66
Field dependence of critical current density J_c .	
4.3-5	67
(a) MR measurement of Py/Cu/Py tri-layered-ring Spin valve. The inset is the full loop. Each circle labeled with number represents a magnetic configuration (or state) which is shown in (b). The single-head arrows indicate the sweep direction. (b) Illustration of each magnetic configuration. The numbers correspond to the labeled circles in (a). The upper ring represents the Py-10nm layer (soft layer), and the bottom one the Py-20nm (hard layer).	
4.3-6	69
Minor loop of the measurement of Py/Cu/Py tri-layered-ring spin valve initially saturated in positive field. The arrows indicate the field sweep directions. The circle represents the intermediate state illustrated in the inset. The upper ring represents the Py-10nm layer (soft layer), and the bottom one the Py-20nm (hard layer).	
4.4-1	72
SEM image of the lateral spin-valve structure. The premalloy (Py) ring and the Py narrow wire are indicated by the arrows. Cu contacts are labeled as 1 through 8. The double-headed arrow on the left side defines the direction of applied field.	
4.4-2	74
(a) The AMR loop of the ring. The arrows indicate the direction of the proceeding process on the loop. The left inset shows the full range of field -1500 ~ +1500 Oe. Vortex directions are schematically indicated in the right inset. Each number with its solid circle is employed to represent each magnetization state and the sequence in process, which is also shown in schematic diagram (b) and (c), in which, the magnetization reversal process is	

schematically represented.

- 4.4-3 76
(a) The full MR loop of the NLSV device (top curve) and the minor loops (middle and bottom curves). The arrows indicate the direction of the proceeding process on the loops. The numbers (correspondent with that in (b) and (c)) represent the sequence in reversal process and the magnetic configurations of the NLSV. (b) Magnetic configurations in the reversal process from positive field to negative. (c) The same as (b) but in reverse sweep.
- 4.4-4 78
(a) The full MR loop of the NLSV device (top curve) and the minor loops (middle and bottom curves). The arrows indicate the direction of the proceeding process on the loops. The numbers (correspondent with that in (b) and (c)) represent the sequence in reversal process and the magnetic configurations of the NLSV. (b) Magnetic configurations in the reversal process from positive field to negative. (c) The same as (b) but in reverse sweep.
- 4.4-5 79
The NLSV loops for the probe arrangement in which the current probes were set as 7 and 8. The depictions for the arrows are the same with that in Figure 4.4-3 and Figure 4.4-4. (a) The CCW-CW loop: CCW in sweep from positive to negative field (forward sweep); and CW in the opposite (backward) sweep (b) The CCW-CCW loop: CCW in both forward and backward sweeps.
- 4.4-6 81
SEM image of a wire-ring lateral spin valve with multi terminals.
- 4.4-7 82
Results of NLSV measurement for device in Figure 4.4-6.
- 4.4-8 85
(a) SEM image of wire-ring spin valve. The numbers indicates the four terminals. (b) Schematic illustrations of the two different voltage probe arrangements. Left: alternative geometry, right: the conventional nonlocal geometry as in the previous section.
- 4.4-9 86
MR measurement of a wire-ring device. The thickness is 22nm for Py, and the width is 120 nm for the wire and 150 nm for the ring with an outside diameter of 1.7 μ m. The wire-ring space is about 40nm, and is bridged by a diffusive channel (Cu) with 170nm in width and 50nm in thickness. (a) Measurement in alternative arrangement with DC current 500 μ A. The numbers indicate each magnetic state in accordance with that in (e). The inset illustrates electrodes arrangement and the relative direction of applied field. (b) Measurement of

conventional AMR for the ring, with DC current $20\mu\text{A}$. (c) and (d) Minor loops to approach the switching field from vortex state to reverse onion state. Before switching (c), and after switching (d). (e) schematic illustrations for the reversal process of the device. The numbers are in accordance with that in (a).

4.5-1 89

MR measurement of the same one two-wire device [(a)~(c)] with DC $500\mu\text{A}$. The thickness is 20nm for Py, and the width is 110 nm for the injector and 200 nm for the detector. The space is about 85nm . The diffusive channel is 210 nm in width and 66nm in thickness. (a) Nonlocal arrangement. (b) Arrangement without voltage probe contact on the detector. (c) Alternative arrangement. (d) MR measurement of single Py wire with AC $150\mu\text{A}$. The Py wire is 30 nm in thickness and 220 nm in width. Diffusive channel is 44 nm in thickness and 200 nm in width.

4.6-1 91

(a) 3D geometry of Cu-Py-crossed structure. The direction is denoted by the 3D coordinate. (b) Top view of the device. Upper-left: the original geometry of Jedema's "contact" measurement. Upper-right: geometry in the present work. All the directions are relative to the coordinate (bottom-left). Bottom-right: Schematic MR loop. Both geometries exhibit the same configuration of this MR loop. ΔR is defined as the difference in resistance between positive and negative magnetization at 0 Oe .

4.6-2 93

Measured MR loops of device for positive (a) and negative (b) current. The thickness is 65 nm for Cu, and 31 nm for Py. The insets denote the arrangements of current and voltage probes, and direction of applied field. To clearly present the polarity of measured voltage, resistance is calculated by dividing the measured voltage by the **absolute** value of current, $R=V/|I|$. (c) Resistance recorded at 0 Oe , with successively alternating magnetization of Py. The odd numbers represent positive magnetization, and the evens represent negative one. (d) Current-dependent ΔR .

4.6-3 94

Cu-width-dependent ΔR s for differently constant widths (a) 200 nm (b) 420 nm and (c) 700 nm of Py wires. (d) Merging all data of (a), (b), and (c). The solid-down triangles represent the estimated values by our roughly simple model. (e) Py-width-dependent ΔR s for differently constant widths (165 nm and 145 nm) of Cu. All the thicknesses are 50 nm for Cu, and 20 nm for Py.

4.6-4 96

Detailed geometry to explain the generated AHE. Left: with electron flow in $+Y$

and M_x in $-X$, positive and negative charges are respectively induced on top and bottom surfaces of Py layer. Right: with M_x reversed, the polarity of charge accumulation also reverses. The horizontal distance between the two vertical dashed lines denotes the width of Cu.

4.6-5 98

Left: Measurement of Hall effect of Cu. Right: Geometry illustrating the required effective field for ordinary Hall effect to induce ΔR in Cu.

4.6-6 100

Geometry of ISHE. (a) Top view. (b) View in X-Z plane. (c) View in Y-Z plane.

4.6-7 100

Geometry of ISHE with perpendicular magnetization and spin-current transport in plane. The d in plane denotes the distance for spin to diffuse from ferromagnet into diffusive channel (here is Au) and to be sensed by voltage electrodes. After Seki [67].

List of Tables

Table 4.4-1 List of distribution of vortex chiralities

80



List of Symbols

E_{ex}	exchange energy
J_{ex}	exchange integral
$\mathbf{S}_i, \mathbf{S}_j, S_i, S_j$	angular momentum vectors of spins
φ	the angle between two spins
\vec{M}, M	magnetization
E_d	demagnetizing energy
\vec{H}_d	demagnetizing field
N_d	demagnetizing factor
E_k	crystalline anisotropic energy
K_0, K_1, K_2	crystalline anisotropic coefficient
$\alpha_1, \alpha_2, \alpha_3$	cosines of angles between the magnetic moment and crystal axes
E_z	Zeeman energy
\vec{m}, m	magnetic moment
\vec{H}_{ex}	external field
G_P	conductance for parallel alignment
G_{AP}	conductance for antiparallel alignment
$\rho_i^\uparrow, \rho_i^\downarrow$	“tunneling” density of states of the ferromagnetic electrodes (designated by index $i = 1, 2$) for the majority- and minority-spin electrons
R_P	resistance for parallel alignment
R_{AP}	resistance for antiparallel alignment
P_i	polarization of the ferromagnetic electrodes (designated by index $i = 1, 2$)
P	effective spin polarization of tunneling electrons
κ	decay constant of wave functions into the barrier
m_e	mass of electron
\hbar	Plank constant
E_F	Fermi energy
ϕ	barrier height
T	temperature
A	parameter of Bloch $T^{3/2}$ law
v	volume
e	electron charge

E, E_x	energy of electron (in x direction)
V	applied bias, voltage
$f(E), f(E - eV)$	Fermi distribution function
J, j	current density
$N(E_x)$	density of states (DOS) as a function of E_x
$\rho, \rho_0, \Delta\rho$	resistivity
I	current
V_{Hall}	Hall voltage
R_{Hall}	Hall resistance
α_{Hall}	Hall coefficient
α_E	anomalous Hall coefficient
$n_{\downarrow}, n_{\uparrow}$	concentrations of up- and down-spin electrons in ferromagnets
ρ_H	Hall resistivity
t	thickness
W	width
α_H	Hall angle
λ	spin diffusion length
P	effective polarization of spin current (injecting from Py into Cu)



CHAPTER 1

Introduction

In the past decades, magnetoelectronic device has attracted much attention both in the applications to spin electronics (or spintronics) and in the fundamentals of spin physics. Its versatile applications in information storage, non-volatile memory, and magnetic sensors have been well studied and developed. With the property in which resistance changes from one level to the other one, multilayered spin valves such as giant magnetoresistance (GMR) and magnetic tunnel junction (MTJ) have been successfully implanted as the memory cell [1-2]. In spite of these devices operating based on clear switching of electric resistance and converting to digital signals of “1” or “0”, the physical background of resistance switching actually originates from the magnetization states of the individual magnetic layers in the multilayered devices. Hence, not only the mechanism of spin transport in magnetoelectronic device but also the magnetization reversal process in ferromagnet need to be studied in detail.

Micromagnetics was, therefore, established to investigate the magnetization reversal process, magnetic domain, and domain wall in micro- or nano-scale ferromagnets; and many experimental studies on magnetic thin-film patterns were also reported [2-12]. With the advantages of direct relation to the distribution of magnetization in real space, magnetic force microscopy [13] (MFM) is an effective tool to observe magnetic image of micromagnetic structure in thin-film patterns [4, 9]. In addition, combined with the real-time sweeping magnetic field, the *in-situ* detection of MFM images can also investigate the process of magnetization reversal [14-16]. Among these studies, quantitative MFM analysis [16] reveals the magnetization reversal process for local parts of a patterned magnetic film by using the statistical calculating of phase shift, and hence promotes MFM usage to relevant

studies.

Unlike the clear understanding on the relations between magnetic images and magnetic structure, the indirect relation between magnetoresistance (MR) signal and magnetic structure, usually cannot be intuitively understood. However, MR measurement provides a more sensitive reflection from the interactions between conducting spin-polarized electrons and local moments in magnetic materials. Besides, in practical applications of magnetoelectro devices, information transport and transmission of actuating energy are mainly based on the electrical operation. Therefore, with both interests in physical origin and feasible applications, a variety of MR phenomena have always been the attractive topics in spintronics.

As the promising applications to spintronics and interests on physics, tunnel magnetoresistance (TMR) phenomena and MTJ devices have caught much attention and many studies have been carried out. Julliere [17] first dedicated to the MTJ experiments and proposed the first theoretic model describing the origin of TMR. According to his assumptions, spin of electrons is conserved during the tunneling process. It infers that up-spin and down-spin electrons tunnel the barrier independently with each other, and hence the conductance occurs in the two independent spin channels. Moreover, the conduction of each spin direction is proportional to the densities of states of that spin in each electrode. This model successfully explained the common TMR phenomenon that the conducting current is larger for parallel alignment of the two ferromagnetic layers than antiparallel one of that, but did not provide the information describing bias voltage and temperature dependence of TMR ratio (%). Julliere's contribution inspired other researchers to further investigate in this field. Although the results were not reproduced by others and Julliere's model is not accurate for realistic TMR phenomena, this simple two-current model still provides a substantial understanding on TMR and even used to

interpret the similar phenomenon of GMR [18]. Later in 1989, Slonczewski [19] proposed the first accurate theoretical explanation of TMR. By extending the free electron model [20], he proposed that, the polarization of tunneling electrons depends not only on the density of states at that ferromagnet, but also on the height of the tunnel barrier. For these free electron models, however, the lattice structure of ferromagnetic electrodes and the variation of the band structure near the insulating barrier are not considered, hence the predictions for TMR are quantitatively unreliable. The most common property for MTJ is the TMR decreasing with increasing bias voltage and temperature. Zhang et al. [21] proposed that spin excitations localized at the interface between ferromagnet and tunneling barrier cause the decrease of TMR ratio. This model was later used by Han et al. [22] to study the conductance and magnetoresistance as a function of voltage and temperature for $\text{Co}_{75}\text{F}_{25}/\text{Al}_2\text{O}_3/\text{Co}_{75}\text{Fe}_{25}$ tunnel junctions. Another mechanism, which could contribute to the voltage dependence of conductance and TMR, is related to the electronic structure of the ferromagnets [23-25]. LeClair et al. [26] proposed a relationship between the magnetotransport properties and the calculated density of states (DOS) for the two different crystallinities of Co. Another crystalline-dependent TMR were also reported [27]. Shang et al. [28] assumed that spin polarization decreases with increasing temperature due to spin-wave excitations, as does the surface magnetization. They then performed the work with fitting to the well known Bloch $T^{3/2}$ law, and obtained a satisfactory explanation for the temperature dependence of TMR. Other studies on explanation by Bloch $T^{3/2}$ law were also discussed [29-36]. By modifying Brinkman model [37], Xiang et al. [38-39] calculated the bias dependence of DOS for majority and minority spin bands by fitting to the measured resistance, and named the conductance minima shifts (CMS) which can also be correlated to the voltage dependence of DOS. The similar fitting works were also carried out by other

researchers [31, 40-43]. For MTJ devices during operation, the possibly encountered high temperature could be near $70 \sim 100 \text{ }^\circ\text{C}$. It is our interest to study the temperature dependence of TMR for MTJ devices around this range of temperature to examine the thermal stability of the devices.

In addition to the spin-dependent tunneling, other phenomena of spin transport such as spin injection and accumulation in normal metal also attract much attention due to the interests in physics and the applications to spintronics. It was Johnson and Silsbee [44] who first demonstrate the spin injection into normal bulk metals. Since then, spin injection into nanometer-sized patterns of a variety of normal metals such as Cu, Al, Au, and Ag [45-60] has been achieved. The description of theoretical model for spin injection dates back to Fert and Campbell [61]. Van Son et al. [62] extended the model to describe transport through ferromagnet-normal metal (F/N) interface. Later, Valet and Fert [63] applied the model based on Boltzmann transport equation to describe the effect of spin accumulation and current-perpendicular-plane GMR.

The significant experiments of another spin transport phenomenon, Spin Hall effect (SHE), has been demonstrated in metallic system [64-67] latter than previously mentioned nonlocal measurement of spin accumulation because the observation of SHE requires advanced experimental technique. However, SHE has been theoretically predicted four decades ago [68]. Later in 1999, Hirsch [69] developed the phenomenological theory with impurity scattering, and then Zhang [70] extended it to the diffusive transport regime. SHE describes a spin current generated in the transverse direction of a charge current and a spin accumulation at lateral boundaries of that conductor. For nonlocal measurements or the crossed geometry, SHE could more or less contribute to the measured signal. Therefore, one might consider and evaluate the magnitude of signal generated by the SHE.

Compared with single domain devices such as MTJs or GMRs used in MRAM, the

domain wall devices are more complicated in reversal process usually associated with single domain wall (bi-domain) or multi domain walls. Hence, the understanding on domain wall motion and the driving source of motion is an important topic for the research and development of domain wall devices. Parkin [71-72] proposed the racetrack memory based on domain wall motion. Moreover, the feasibility to logic gates has also been reported [73-75]. The common feature of these studies is that the ferromagnetic patterns carrying domains and domain walls are narrow wires either in straight- or curved- line shapes. The narrow wire makes domain wall and domain-wall motion clearly defined due to the shape anisotropy along the directions of curve or straight line. In addition, for a curve shape, it is easily for one to manipulate the initial domain wall position by properly choosing the relative direction between the pattern and the applied field. This useful approach has been achieved to study the phenomenon of domain wall motion in narrow wires [76-79]. As the physical interest and the requirement of electric operation for a magnetoelectro device, the phenomenon of current-induced (or current-driven) domain wall motion have also given rise to a great interest to explore for single-layered ferromagnetic narrow wires [80-85]. For these investigations, the approaches to detect domain wall motion are MFM and AMR measurements which may be constrained by the electric operation when used as a device. For tri-layered (ferromagnetic/normal-metaleel/ferromagnetic; F/N/F) spin valves [86-90], although the measurement fits to the application of the device, the tri-layered structure makes the behaviors of domain wall motion more complicated since the interaction between the two ferromagnetic (FM) layers affects the domain wall motion which is different from that in single-layered FM.

The vortex state of a ferromagnetic ring features a bi-direction of degeneracy: clockwise (CW) or counter clockwise (CCW). This chirality could serve as a memory bit by considering the direction CW or CCW as “1” or “0” signal. Besides, with its

advantages of the almost zero stray field out of the ring structure, FM-ring memory cell can be a stable and low noise device. Therefore, FM ring-shaped structure has attracted much attention and many studies on basic behaviors of reversal process of FM rings have been carried out [91-95]. Since the transition of onion-to-vortex in ring structure is completed by domain wall propagation, the behavior the domain wall motion plays an important role in FM-ring device when observing the reversal process in tri-layered [96-100] or single-layered [101-102] rings by MR measurement. The current-induced domain wall motion in FM ring was also performed for single-layered [102] and tri-layered [103] structures. The detection of vortex chirality of FM rings can be performed by tri-layered structure [98-100, 103]. For the single-layered, however, the measurement with only AMR provides no crucial information for determining the chiralities. It was Kimura [6, 104] first carried out the detection of vortex chirality of a single-layered structure by using nonlocal spin valve (NLSV) measurement to sense spin accumulation in the normal-metal diffusive channel and determine the spin orientation of the spin injector adjacent to the spin diffusive channel.

In this dissertation, we review the researches related to the voltage and temperature dependent TMR of MTJ devices, reversal process of magnetic patterns, and spin dependent transport such as spin injection, spin accumulation and AMR behaviors in Chapter 1. The basic theory and some phenomena that relate to the investigations in this dissertation are described in Chapter 2. Chapter 3 presents the principle and methodology of the experiments. In Chapter 4 we discuss the experimental results and compare with the results reported by other researchers for satisfied explanations. Section 4.1 presents the results of the quantitative MFM analysis. We investigated a magnetic patterned strip with two-different-width parts by analyzing its MFM phase changes, and focused on the two ends of the strip and the region in which the wider

part changes to the narrower one. Section 4.2 presents the temperature and voltage dependent TMR measurements of MTJs. The possible physical origins of both dependences were discussed. In Section 4.3, we describe the magnetization states and reversal behaviors of the single-layered Py ring and the tri-layered spin valve Py ring. Inspired by the drawback of the incapability of detecting the chirality of the ferromagnetic rings (mentioned in Sec. 4.3), we further fabricated and measured the nonlocal lateral spin valve (NLSV) including a Py wire and ring to sense the spin accumulation signals and determine the direction of circulating vortex in the ring. The results are shown in Section 4.4. Besides, to obtain the larger spin signals in the lateral spin valve (LSV), we shortened the distance of spin diffusive channel by removing the Cu cross inserted in between the Py ring and the wire. The structure is no longer a nonlocal geometry. However, the spin accumulation can still be detected and enhanced but with an extra signal that exhibits asymmetric MR behavior. In Section 4.5, we tried extracting the spin accumulation signals by replacing the ring with a second wire but in different width with the first one. We then measured the three different geometries in this two-wired LSV. In Section 4.6, we systematically studied the physical origin of the asymmetric signals found in section 4.4 and 4.5. The results of the size dependent measurement suggests the physical origin is most possibly from the anomalous Hall effect of the in-plane magnetization Py wire (the spin injector).

CHAPTER 2

Introduction to Basic Theory and Phenomena

2.1 Magnetic domain and domain wall

A stable magnetic state consists of domains and domain walls existing within a ferromagnetic material (bulk, film, or patterned film) and reaching an equilibrium state without varying with time in macroscopic scale. The stable state is a result of competition among exchange energy, demagnetizing energy, anisotropic energy (usually the crystalline anisotropy), and Zeeman energy in that material in which the total energy stays at the minimum under the stably applied magnetic field.

Exchange interaction and energy The exchange interaction comes from a consequence of a quantum effect that the atomic magnetic moments tend to align to the same direction with each other in ferromagnetic. This interaction affects the alignment between two adjacent spin elements in a short range of few atoms. Hence, the exchange energy of the alignment between two spin elements (usually the atomic magnetic moments) is given by [108]

$$E_{ex} = -2 J_{ex} \mathbf{S}_i \cdot \mathbf{S}_j = -2 J_{ex} S_i S_j \cos\varphi, \quad (2-1)$$

where \mathbf{S}_i and \mathbf{S}_j represent the angular momentum vectors of two adjacent spins, J_{ex} is called the exchange integral, which occurs in the calculation of exchange effect, and φ is the angle between the two spins.

Demagnetizing energy The demagnetizing energy is caused by demagnetizing field which is induced by the magnetization of a ferromagnet. The direction of the demagnetizing field is usually opposite to the magnetization in the ferromagnet, and

hence the field tends towards reducing the total magnetization, i.e., “demagnetizing” the ferromagnet itself. It also gives rise to the *shape anisotropy*. The energy of the demagnetizing field is completely determined by an integral over the volume of the magnet and can be expressed as

$$E_d = -\frac{1}{2} \int_{\text{magnet}} \vec{M} \cdot \vec{H}_d dv, \quad (2-2)$$

where \vec{H}_d is demagnetized field and is given by $\vec{H}_d = -N_d \vec{M}$. N_d is the demagnetizing factor [108] which depends on the geometric shape of the ferromagnet. For a ferromagnetic strip or narrow wire, N_d is very small ($N_d \ll 1$) along the direction of wire axis. It results in that the magnetization along the wire direction maintains little demagnetized at the remanence, i.e., most of the moments is aligned to the wire direction in the absence of applied field. With this shape anisotropy, magnetic wires are usually used to study domain wall motion.

Crystalline anisotropy When an applied field turns the magnetization vector of a crystal away from the easy direction in that crystal, the field must do work against the anisotropic force. Hence, there must be *crystal anisotropy energy* (E_k) stored in the crystal in which the saturated magnetization (M_s) points in a noneasy direction. E_k can be expressed as [108]

$$E_k = K_0 + K_1(\alpha_1^2 \alpha_2^2 + \alpha_2^2 \alpha_3^2 + \alpha_3^2 \alpha_1^2) + K_2(\alpha_1^2 \alpha_2^2 \alpha_3^2) + \dots, \quad (2-3)$$

where $K_0, K_1, K_2 \dots$ are constants for a particular material. Higher powers are generally neglected. K_0 is independent of angle and is usually ignored. α_1, α_2 , and α_3 are the cosines of angles between the magnetic moment and crystal axes.

Zeeman energy The Zeeman energy (E_z) is resulted from the interactions between magnetic moments and an applied field. For a single moment, the energy is

expressed as

$$E_z = -\vec{m} \cdot \vec{H}_{ex} = -mH_{ex} \cos\theta, \quad (2-4)$$

where H_{ex} is the externally applied field, and θ is the angle between the moment and the applied field. For the whole volume of a ferromagnet, the Zeeman energy per unit volume is then calculated by integrating each local magnetization over the whole volume and is given by

$$E_z = -\int \vec{M}(v) \cdot \vec{H}_{ex} dv. \quad (2-5)$$



2.2 Magnetic tunnel junction (MTJ) and Tunnel Magnetoresistance (TMR)

The phenomenon of TMR is from the measurement for an MTJ, which consists of two ferromagnetic layers separated by an insulating tunnel barrier. The insulating layer is thin enough (usually few Å ~ 15 Å) for conducting electrons to quantum mechanically tunnel through the barrier. When a bias voltage applied across the MTJ, a net tunneling current is flowing through the junction. The measured MTJ resistance is usually higher when the two ferromagnetic layers are in anti-parallel alignment than that when they are in parallel alignment. This is the general TMR phenomenon observed. Figure 2.2-1 shows a TMR loop of a pseudo-spin-valve MTJ.

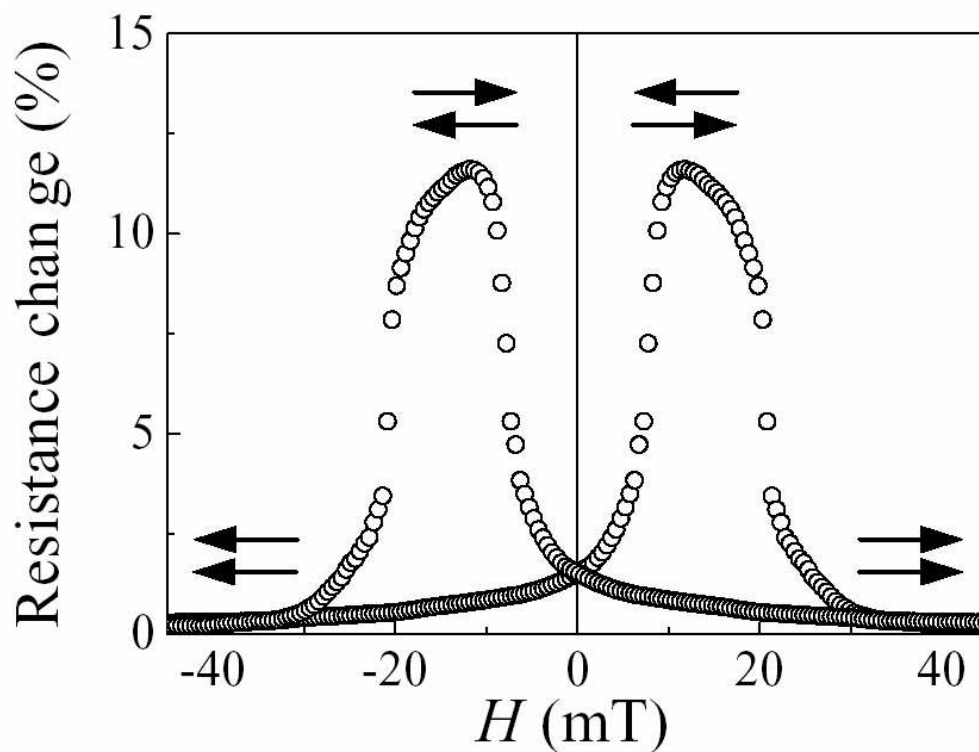


Figure 2.2-1 First observation of reproducible, large room temperature MR in a CoFe/Al₂O₃/Co MTJ. The arrows indicate the relative magnetization orientation in the CoFe and Co layers. After Moodera *et al.* [109].

2.2.1 Julliere's Model

Julliere [17] assumed that tunneling of up-spin and down-spin electrons are two independent processes, so that the conductance occurs in the two independent spin channels. The assumption also mentioned that conductance for a particular spin orientation is proportional to the product of the effective (tunneling) density of states of the two ferromagnetic electrodes. According to these assumptions, the conductance for the parallel and antiparallel alignment, G_P and G_{AP} , can be written as follows:

$$G_P \propto \rho_1^\uparrow \rho_2^\uparrow + \rho_1^\downarrow \rho_2^\downarrow, \quad (2-6a)$$

$$G_{AP} \propto \rho_1^\uparrow \rho_2^\downarrow + \rho_1^\downarrow \rho_2^\uparrow, \quad (2-6b)$$

where ρ_i^\uparrow and ρ_i^\downarrow are the tunneling density of states (DOS) of the ferromagnetic electrodes (designated by index $i = 1, 2$) for the majority- and minority-spin electrons. According to the majority of researchers, the TMR can be defined as the conductance difference between parallel and anti-parallel magnetizations, normalized by the anti-parallel conductance, i.e.

$$TMR \equiv \frac{G_P - G_{AP}}{G_{AP}} = \frac{R_{AP} - R_P}{R_P}. \quad (2-7)$$

With Eqs. (2-6) and (2-7), Julliere's formula can be expressed as

$$TMR \equiv \frac{2P_1P_2}{1 - P_1P_2}, \quad (2-8)$$

which expresses the TMR in terms of the effective spin polarizations (SPs) of the two ferromagnetic electrodes

$$P_i = \frac{\rho_i^\uparrow - \rho_i^\downarrow}{\rho_i^\uparrow + \rho_i^\downarrow}, \quad (2-9)$$

where $i = 1, 2$.

2.2.2 Slonczewski's model

Slonczewski [19] considered the tunneling between two identical ferromagnetic electrodes separated by a rectangular potential barrier assuming that the ferromagnets can be described by two parabolic bands shifted rigidly with respect to one another to model the exchange splitting of the spin bands. In the limit of thick barrier, he found that the conductance is a linear function of the cosine of angle θ between the magnetic moments of the films,

$$G(\theta) = G_0(1 + P^2 \cos \theta). \quad (2-10)$$

Here P is the effective spin polarization of tunneling electrons given by

$$P = \frac{k^\uparrow - k^\downarrow}{k^\uparrow + k^\downarrow} \frac{k^2 - k^\uparrow k^\downarrow}{k^2 + k^\uparrow k^\downarrow}, \quad (2-11)$$

where κ is the decay constant of the wave function into the barrier which is determined by the potential barrier height ϕ , $k = \sqrt{(2m_e / \hbar^2)(\phi - E_F)}$. In the limit of a high barrier it tends to unity reducing Slonczewski's result for TMR to Julliere's formula. However, if the barrier is not very high and the decay constant is comparable to or less than the wave vectors of electrons in the ferromagnetic metals, the magnitude of TMR decreases with decreasing ϕ and even changes sign for sufficiently low barriers, which is illustrated in Figure 2.2-2.

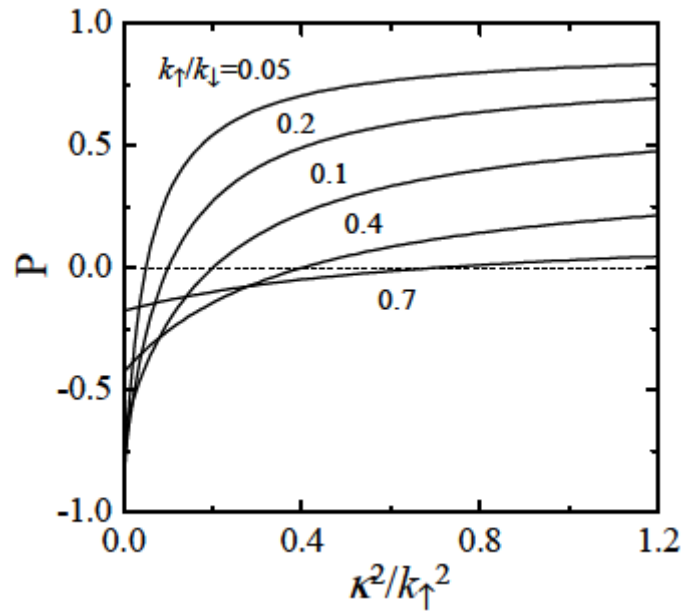
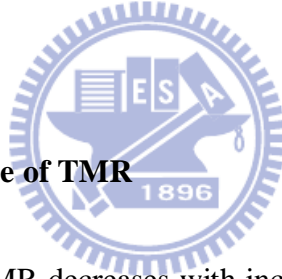


Figure 2.2-2 Spin polarization of the tunneling conductance as a function of the normalized potential barrier height for various values of k_+/k_- . After Slonczewski [19].



2.2.3 Temperature dependence of TMR

In all tunnel junctions the TMR decreases with increasing temperature. Shang [28] et al. assumed that the tunneling spin polarization P decreases with increasing temperature due to spin-wave excitations, as does the surface magnetization. They thus assumed that both the tunneling spin polarization and the interface magnetization followed the same temperature dependence, the well-known Bloch $T^{3/2}$ law, $M(T) = M(0)(1-AT^{3/2})$. By fitting parameter A , Shang et al. obtained a satisfactory explanation for the temperature dependence of TMR, as demonstrated by the fitting in Figure 2.2-3.

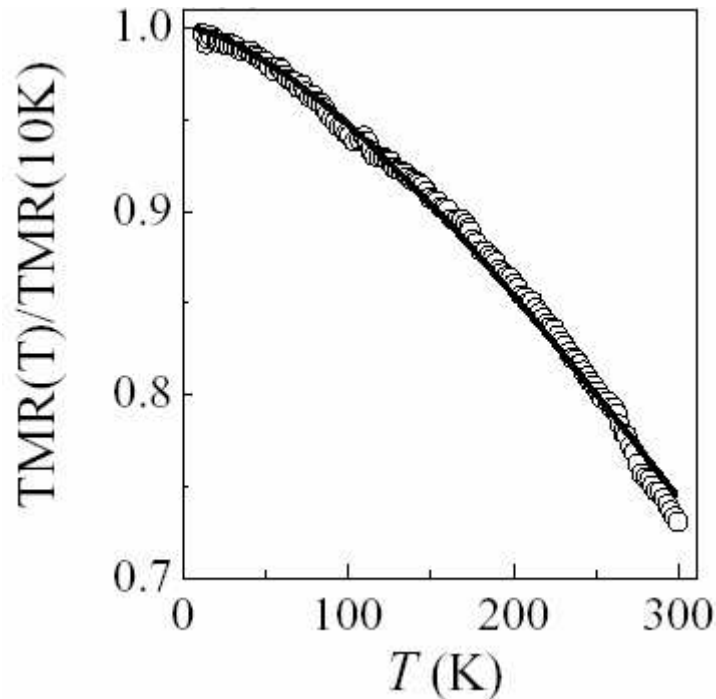


Figure 2.2-3 Temperature dependence of TMR for a Co/Al₂O₃/Co MTJ (circles) along with a fit to the model of Shang *et al.* [28] (solid line).

2.2.4 Voltage dependence of TMR

In most MTJ's the magnitude of TMR decreases strongly with increasing bias voltage, similar to that observed originally by Julliere (Figure 2.2-4). Zhang *et al.* [21] proposed that spin excitations localized at the interface between ferromagnet and tunneling barrier cause the decrease of TMR ratio. However, experiments by Wulfhekel *et al.* [110] seem to be inconsistent with this plausible explanation. Here we introduce another explanation by Xiang *et al.* [38-39]. By modifying the Brinkman model [37], they calculated the bias dependence of DOS for majority and minority spin bands by fitting to the measured resistance, and named the conductance minima shifts (CMS) which can also be correlated to the voltage dependence of DOS.

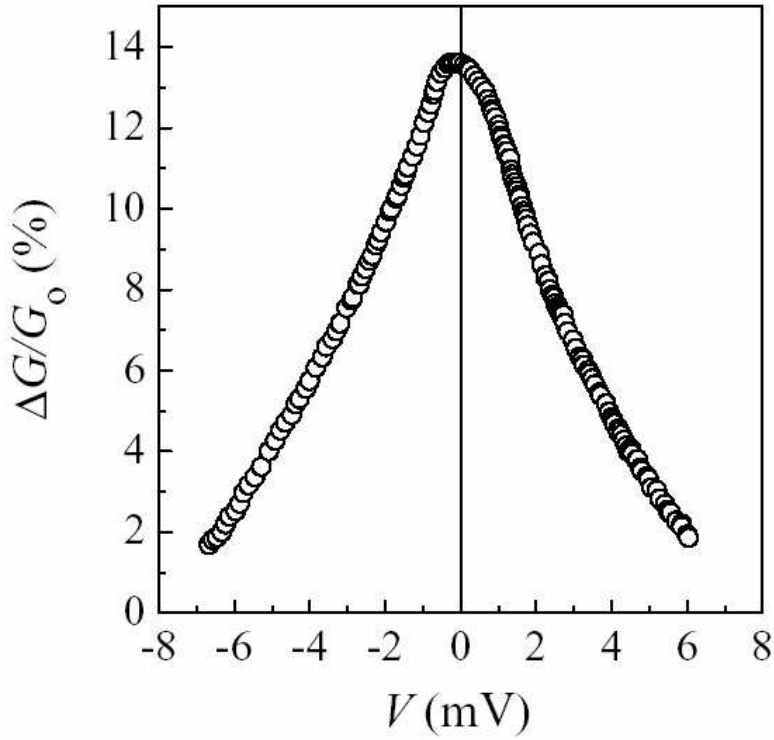


Figure 2.2-4 Original demonstration of the tunneling magnetoresistance effect. The relative conductance change due to an applied magnetic field versus applied bias in a Fe/Ge/Co junction at 4.2 K. After Julliere [17].

Brinkman model and its modification Brinkman's model [37] calculates the tunnel barrier conductance of a metal-insulator-metal structure. Consider two metals a and b separated by an arbitrary potential barrier $\phi(x)$. Assuming the WKB approximation inside the barrier the tunneling current density is given by [111]

$$j = \frac{4\pi e}{\hbar} \sum_{k_i} \int_{-\infty}^{+\infty} dE_x N_a(E) N_b(E - eV) \tau(E_x) \times [f(E) - f(E - eV)], \quad (2-11)$$

where $N_a(E)$ and $N_b(E)$ are the density of states for a given transverse momentum k_i and total energy E for systems a and b , respectively. $f(E)$ is the usual Fermi distribution function. E_x is the total energy in the direction perpendicular to the barrier, $\tau(E_x)$ is the tunneling probability which has the form

$$\tau(E_x) = C \exp\left(-\frac{2}{\hbar} \int_0^d \{2m_e[\phi(x', V) - E_x]\}^{1/2} dx'\right), \quad (2-12)$$

where d is the barrier thickness and $\phi(x',V)$ is the barrier height at the voltage V and the position x in the barrier. The preexponential factor C may depend on E_x .

Xiang et al. [38-39] later introduced the spin- and energy-dependent DOS into Brinkman's model. The current density is then expressed as

$$J \propto \int_{-\infty}^{+\infty} \exp\left(-\frac{2}{\hbar} \int_0^d \{2m_e[\phi(x,V) - E_x]\}^{1/2} dx\right) N(E_x) [f(E) - f(E - eV)] dE_x, \quad (2-13)$$

where $\phi(x,V) = \phi_1 + (x/d)(\phi_2 - eV - \phi_1)$, ϕ_1 and ϕ_2 are the barrier height at each interface, d is the barrier width, V is the applied bias, and x is the distance from the interface with barrier height ϕ_1 . $N(E_x)$ is the DOS function and can be expressed as

$$N(E_x) = N_{1\uparrow}(E_x)N_{2\uparrow}(E - eV) + N_{1\downarrow}(E_x)N_{2\downarrow}(E - eV), \quad (2-14a)$$

$$N(E_x) = N_{1\uparrow}(E_x)N_{2\downarrow}(E - eV) + N_{1\downarrow}(E_x)N_{2\uparrow}(E - eV). \quad (2-14b)$$

(2-14a) is for parallel configuration, and (2-14b) for anti-parallel configuration. Here, 1 and 2 represent the two FM electrodes.

With the extended Brinkman model, the DOS of Co and FeNi electrodes was derived (cases of Co(3.6nm)/AlOx/Co(3.6nm) and FeNi(8nm)/AlOx/FeNi(16nm) in [39]), and are shown in Figures 2.2-5 (c) and (d). It is clear that the DOS functions in both configurations are bias dependent. In the negative bias region of the parallel (P) configuration, the DOS function decreases with increasing bias. This results in a CMS to the left. Compared to P configuration, the DOS function in anti-parallel (AP) configuration has a weaker dependence on bias. Thus, not only does the barrier height contribute to the CMS, but the bias dependence of the DOS function also affects the shift. We can see from the experimental results that this contribution is quite significant. Since the bias dependence of the DOS function is different between the P and AP configurations, the shifts in the conductance minima are different. In a symmetrical junction, the DOS function is always symmetric about zero bias.

Consequently there is no CMS.

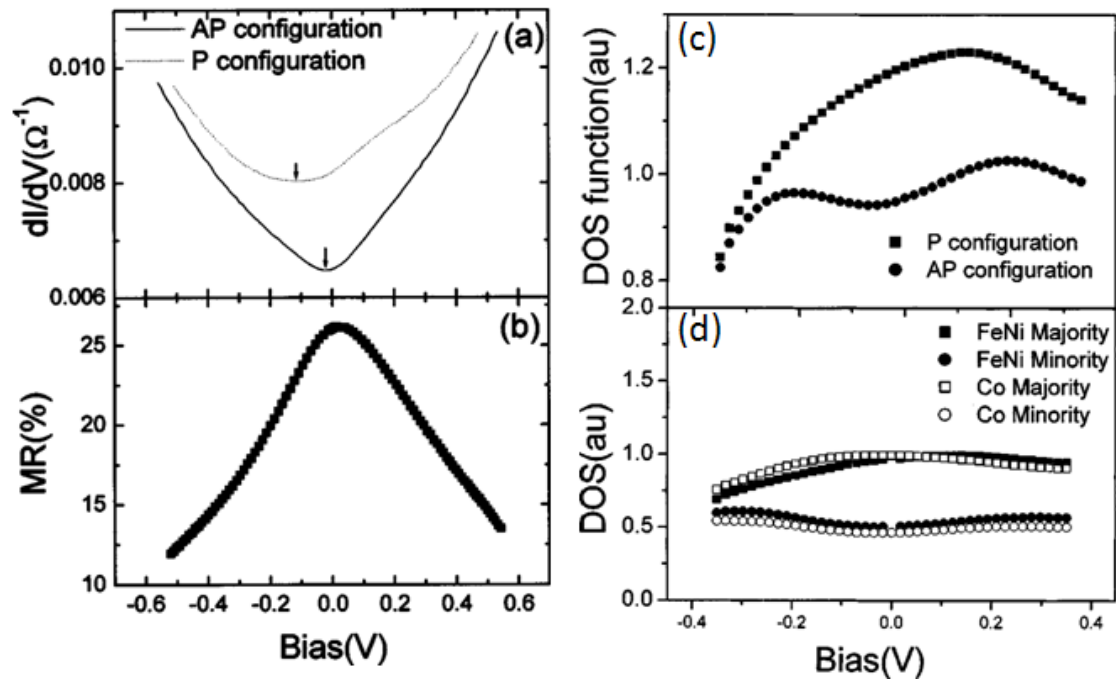


Figure 2.2-5 The bias dependence of (a) the dI/dV in the AP (solid line) and P (dotted line) configurations, and (b) TMR. Arrows mark the local minima in the AP and P configurations. (c) The energy-dependent DOS function $[N(E_x)]$ for P (squares) and AP (circles) configurations. (d) The fitted energy-dependent DOS for FeNi majority (solid squares), FeNi minority (solid circles), Co majority (open squares), and Co minority (open circles). After Xiang et al. [38-39].

2.3 AMR and Hall Effect

In this section, we consider other effects of an applied magnetic field.

Anisotropic magnetoresistance (AMR) AMR describes the effect in which the electric resistance depends on the relative orientation, θ , between the local moment and the direction of charge current in a ferromagnetic material. The phenomenological dependence of the resistance on θ is given by

$$\rho(\theta) = \rho_0 + \Delta\rho \cos^2(\theta), \quad (2-15)$$

where ρ_0 is the zero-field resistivity and $\Delta\rho \equiv \rho_{\parallel} - \rho_{\perp}$ in which parallel and perpendicular refer to the orientation of the in-plane magnetization and current in the material.

Ordinary and Anomalous Hall effect In 1879, E. Hall [112] discovered that a voltage difference is produced across an electric conductor, transverse to an electric current in that conductor with a magnetic field perpendicular to the current (Figure 2.3-1). The voltage difference or, the Hall voltage (V_{Hall}) can be expressed in a phenomenological form,

$$V_{Hall} = E_{Hall} a = \alpha_{Hall} H \frac{I}{t}, \quad (2-16)$$

where E_{Hall} is the electric field generated in the direction transverse to the current, a is the transverse distance of the conductor, t is the conductor thickness perpendicular to a , I is the electric current, H is the applied magnetic field perpendicular to the current, and α_{Hall} is the Hall coefficient which is usually a constant depending on materials. Since Equation (2-16) describes a linear relationship between V_{Hall} and I . We then further derive the Hall resistance, R_{Hall} , as

$$R_{Hall} = \frac{V_{Hall}}{I} = \alpha_{Hall} H \frac{1}{t}. \quad (2-17)$$

This relation indicates that R_{Hall} is proportional to the applied field and reciprocal to the

size parameter t in the direction of the field, and is useful for experimental measurement to determine the α_{Hall} of a material. Hence, the Hall resistivity, ρ_{Hall} , can be expressed as

$$\rho_{Hall} = \frac{V_{Hall}}{I} = \frac{R_{Hall} I}{I} = \alpha_{Hall} H. \quad (2-18)$$

Equation (2-18) describes the linear relation between the Hall resistivity and the applied field. The Hall coefficient α_{Hall} can be either positive or negative, depending on the material type.

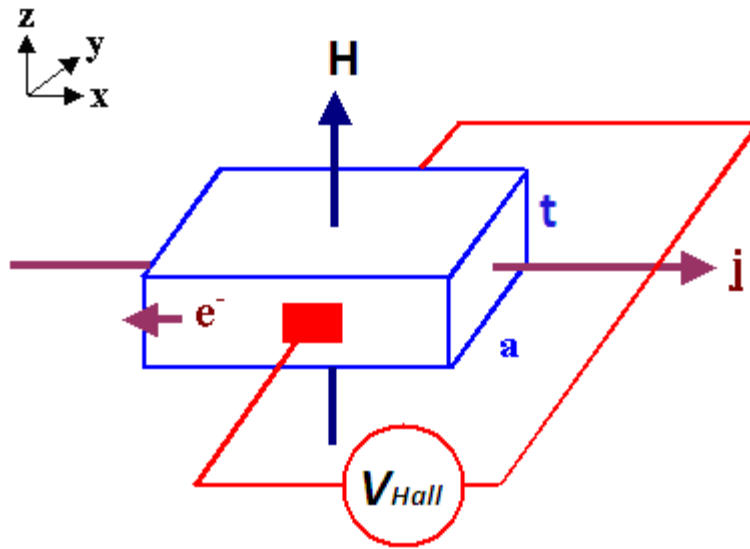


Figure 2.3-1 Illustration of the Hall Effect.

We then discuss the Hall Effect in ferromagnetic materials. The Hall voltage consists of a sum of two terms. The first term is proportional to the magnetic field, as we mentioned above, and has been called the ordinary Hall Effect. Its order of magnitude and sensitivity to variations in temperature and in composition are comparable with Hall Effect in non-ferromagnetic materials. The second term is proportional to the magnetization and has been called the anomalous or extraordinary Hall effect. Equation (2-17) can then be extended to a ferromagnetic case [113-115]

$$R_{Hall} = \frac{V_{Hall}}{I} = \frac{1}{t} \{ \alpha_{Hall} H + \alpha_E M(H) \}, \quad (2-19)$$

where α_E is anomalous Hall coefficient, and $M(B)$ is the magnetization which is the function of field. By neglecting the ordinary term, the R_{Hall} - B curve exhibits almost a magnetization process like M-B curve since $M(B)$ is directly proportional to the R_{Hall} . A measurement of Hall effect in ferromagnets is shown in Figure 2.3-2.

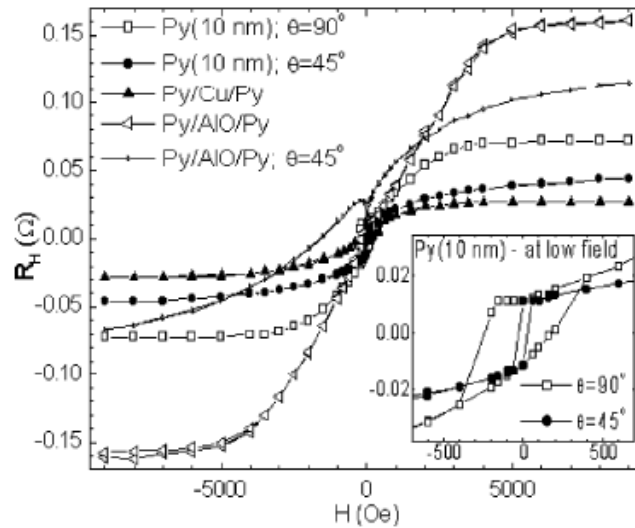


Figure 2.3-2 Hall effect in ferromagnetic materials [113].



2.4 Spin injection and accumulation in lateral spin valve

Spin current [56] is generated in a ferromagnet with unequal popularities of conducting up- and down-spin electrons. This inequality is mainly due to the unequal DOS of up- and down-spin bands near the Fermi level (Figure 2.4-1(a)). The spin

$$\text{current } I_s \text{ can be expressed as } I_s = \frac{n_\uparrow - n_\downarrow}{n_\uparrow + n_\downarrow} I_C = P_F I_C, \quad (2-20)$$

where $P_F = (n_\uparrow - n_\downarrow)/(n_\uparrow + n_\downarrow)$ is spin polarization (SP) which is defined by Equation (2-9), n_\uparrow and n_\downarrow are the concentrations of up- and down-spin electrons in the ferromagnet, and I_C is the total charge current. Whereas, in nonmagnet (Figure 2.4-1(b)), the DOS is equal for up- and down-spin bands, and the current is un-polarized.

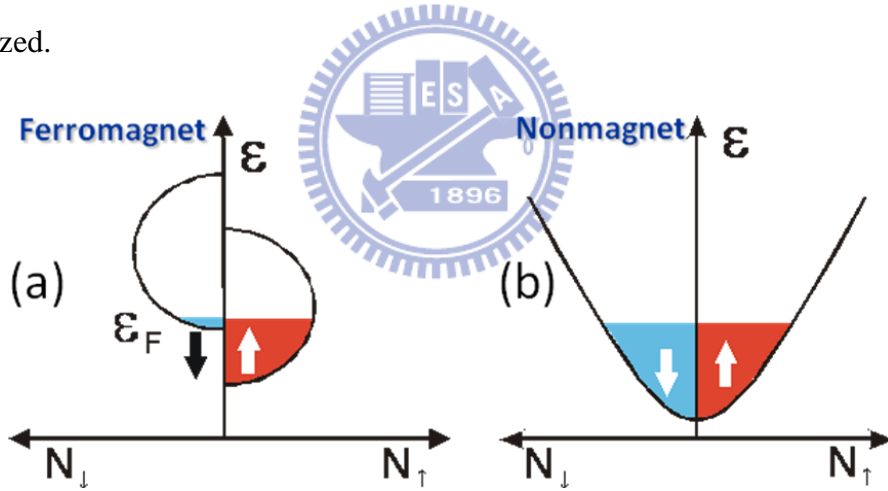


Figure 2.4-1 Illustration of DOS in a ferromagnet (a) and nonmagnet (b).

When the spin current flows across the F/N junction (Figure 2.4-2), however, the spin splitting in the chemical potential is induced in both F and N subsection, and hence the non-equilibrium spin accumulation is induced in nonmagnet. The spin dependent chemical potential without voltage drop due to charge current can be measured by nonlocal spin valve [45].

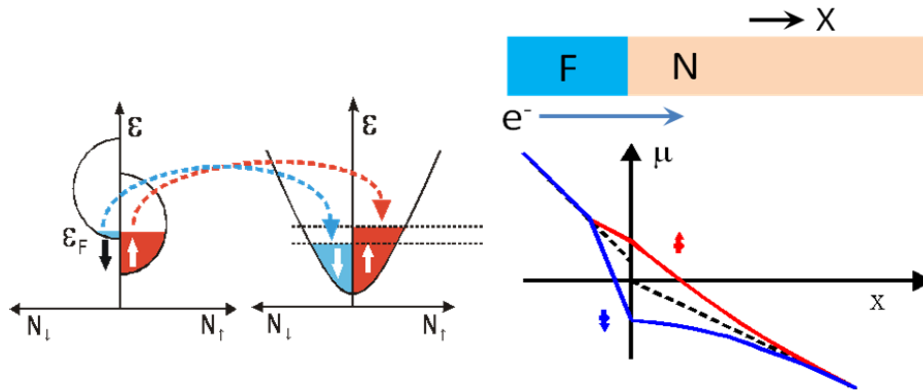


Figure 2.4-2 Illustrations of the spin splitting in the chemical potential induced by spin injection.

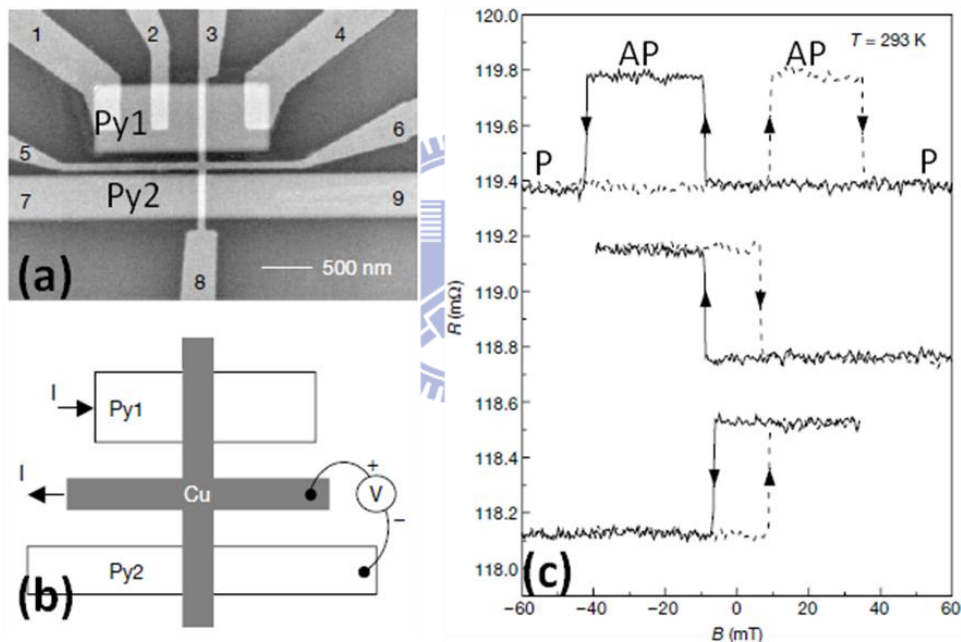


Figure 2.4-3 (a) SEM image of the mesoscopic spin valve junction. The two wide horizontal strips are the ferromagnetic electrodes Py1 and Py2. The vertical arms of the Cu cross (contacts 3 and 8) lie on top of the Py strips; the horizontal arms of the Cu cross form contacts 5 and 6. Contacts 1, 2, 4, 7 and 9 are attached to Py1 and Py2 to allow four terminal AMR measurements of the Py electrodes. (b) Schematic representation of the non-local measurement geometry. Current is entering from contact 1 and extracted at contact 5. The voltage is measured between contact 6 and contact 9. (c) The results of nonlocal measurements. Upper curve: An increase in resistance is observed, when the magnetization configuration is changed from parallel to anti-parallel. The solid (dashed) lines correspond to the negative (positive) sweep direction. Middle and bottom curves: The minor loops. After Jedema [45].

2.5 Magnetic reversal process of ferromagnetic ring

During released from saturation to low field, the magnetization of a ferromagnetic ring gradually forms a bi-domain state in which a pair of head-to-head and tail-to-tail domain walls positioned at both sides aligned to the initial saturated direction (Figure 2.5-1). This bi-domain is called “onion” state. It is a consequent result of the shape anisotropy, since most of the local moments are aligned to the perimeter direction of the ring. With the applied field continuing swept to the opposite direction, the two domain walls start moving towards each other, resulting in the annihilation of the domain walls. In this state, all the local moments are still aligned to the perimeter and in the same circulation without domain walls. The whole magnetization is thus in a vortex formation. This state is named “vortex” state. It is reasonably to understand that the chirality of the vortex can either be clockwise (CW) or counterclockwise (CCW), since there is no preference chirality for a symmetric ring. When increasing stronger field magnitude in opposite direction, the vortex state is destroyed and two domain walls nucleate at both sides of the ring aligned to the field direction. Hence, the bi-domain forms again but its magnetization is opposite to that of the first onion state mentioned previously. This state is called “reverse onion” state, whose direction is opposite to the initial saturated field. For clear identification, one can also names the first onion state as “forward onion” state when describing the magnetic switching of a ferromagnetic ring.

However, the size dependence strongly affects the reversal process. With a larger aspect ratio of diameter (or radius) to width of the ring, the vortex state tends to no existence during a regular reversal sequence. Besides, the thinner film of ferromagnetic ring also prefers no existence of the vortex. The switching phase diagrams of the magnetic rings have been reported [91, 93] with varying sizes.

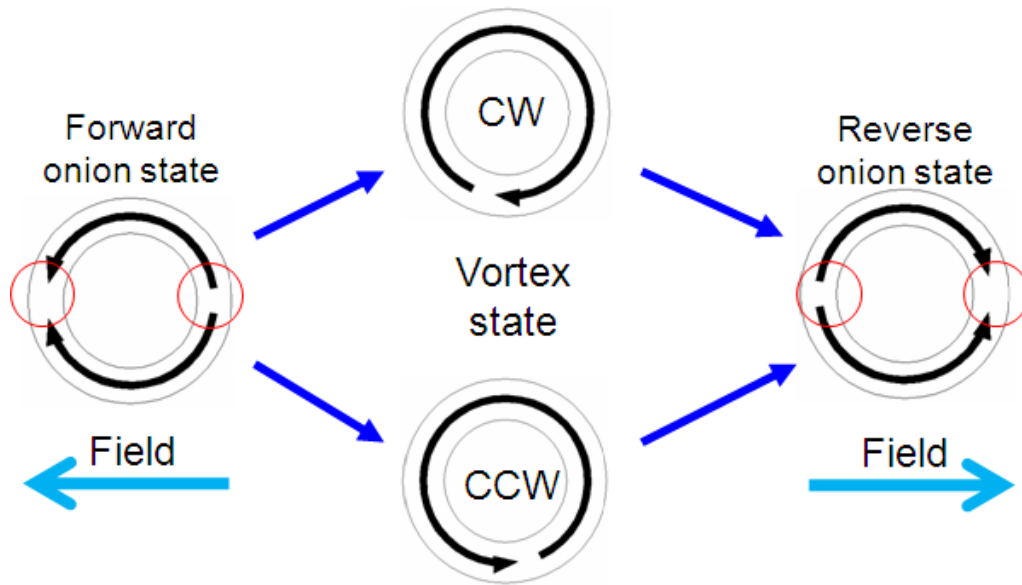


Figure 2.5-1 Reversal process of a ferromagnetic ring. Switching sequence is from left to the right sides. The small circles indicate domain walls. The left ring is the first “onion” state also named “forward onion”. Vortex state (middle) can either be CW or CCW. The right is the reverse onion state.

The SEM images and typical magnetic hysteretic loops of ferromagnetic rings are shown in Figure 2.5-2.

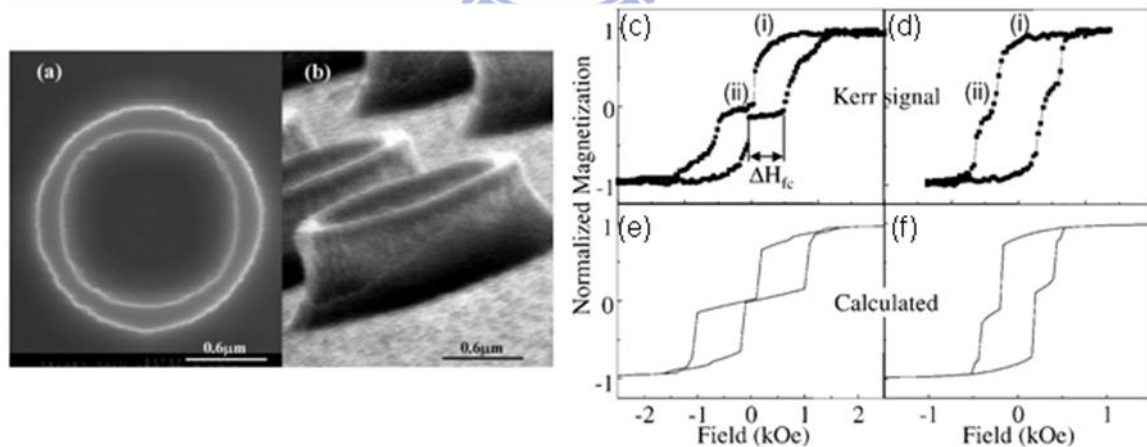


Figure 2.5-2 SEM micrographs of rings (a) before and (b) after deposition. After Rothman, et al. [94]. (c) and (d) Typical in-plane MOKE hysteresis loops measured on rings with the same outer and inner diameter of 700 nm and of 300 nm, respectively, but for different thickness of (c) 50 nm and (d) 20 nm. (i) and (ii) represent the forward and vortex state. (e) and (f) Calculated hysteresis loops. After Li, et al. [116].

AMR measurement of ferromagnetic rings has been systematically studied by Lai, et al. [101]. In their studies, the vortex states can be characterized by in AMR loop of a ferromagnetic ring as shown in Figure 2.5-3.

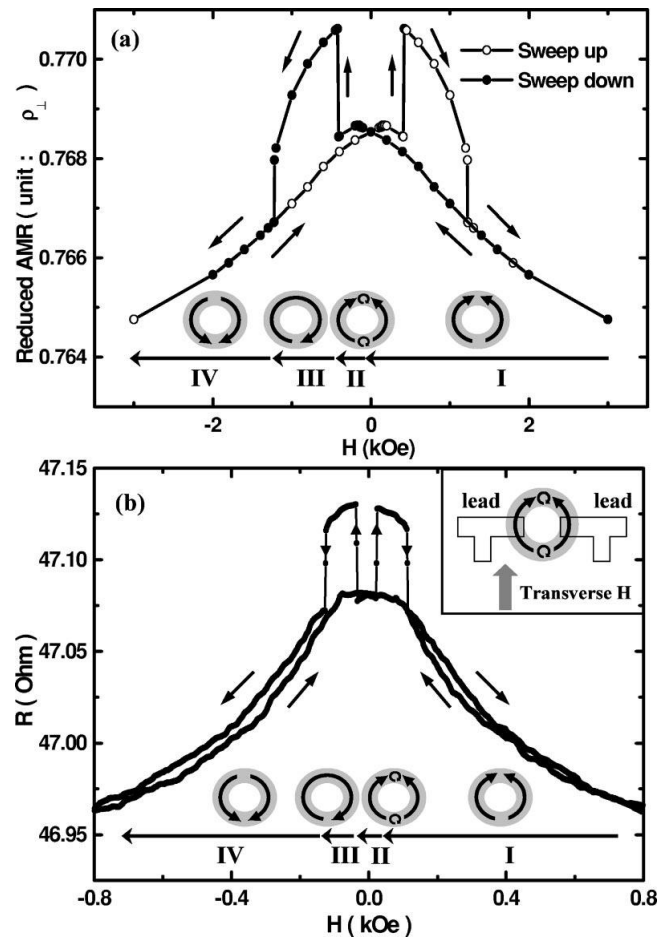


Figure 5.2-3 Transverse MR curves of Permalloy ring obtained by (a) theoretical and (b) experimental methods. The spatial relationship between the domains and leads is shown in the inset. The metastable states observed in the sweep-down process are schematically represented in the lower part of each figure. After Lai [101].

CHAPTER 3

Experiments

3.1 Sample preparation

Patterned magnetic thin films in submicron and nano sizes were fabricated mainly by electron beam (E-beam) lithography. These patterned magnetic devices were constructed on SiO₂(50 nm)/Si substrates on which electrical contact pads were formed by photolithography. Both E-beam lithography and photolithography were followed by series processes of deposition and lift-off techniques.

Photolithography to fabricate contact pads The SiO₂/Si substrates were first coated with positive photoresist (LOR 10B), spined at speed of 4000 rpm for 25 sec, and baked at temperature of 190°C for 5 min. Then, the substrates was coated S1813 photoresist at the same spin conditions as LOR 10B and baked at temperature of 120 °C for 3 min. After exposing and developing, the Au(40nm)/Ti(10nm) films were deposited on the substrates. The lift-off technique was performed to complete the pad patterns as shown in figure. 3.1-1. The EVG620 mask aligner was used as photoresist exposure with intensity = 15 mw/cm² for 5.7 sec.

E-beam lithography to fabricate magnetic devices The PMMA electron resist were first coated on the pre-deposited pad substrates at the conditions of spin speed = 4000 rpm for 25 sec and baked at temperature of 135°C for 1hr. The following processes were the same as the photolithography process. E-beam source was provided by an FEI model XL30 SFEG SEM. The exposure dose was 0.3 ~ 0.6 nC/cm depending on the desired widths. Both center-to-center distance and line spacing were 10 nm.

Deposition of thin films DC magnetron sputtering was used to deposit the Cu, and Permalloy (Py: Ni₈₀Fe₂₀), Au, and Ti thin films. The base pressure of the vacuum system was about $5.0 \sim 7.0 \times 10^{-7}$ torr, and the working pressure $1.0 \sim 1.2 \times 10^{-3}$ torr with introducing Ar gas into the vacuum chamber.

Ar-ion milling Before depositing Cu leads on magnetic patterns, the Ar-ion beam was used to pre-clean the surface of magnetic thin films at the working pressure of 1.0×10^{-5} torr.

Fabrication of MTJ The MTJ samples were provided by ERSO, ITRI (Electronics Research & Service Organization, Industrial Technology Research Institute, Hsinchu, Taiwan), and hence detailed manufacturing process of the MTJs we measured is not discussed in this dissertation. Instead, the brief processes will be presented in section 4.2.1.

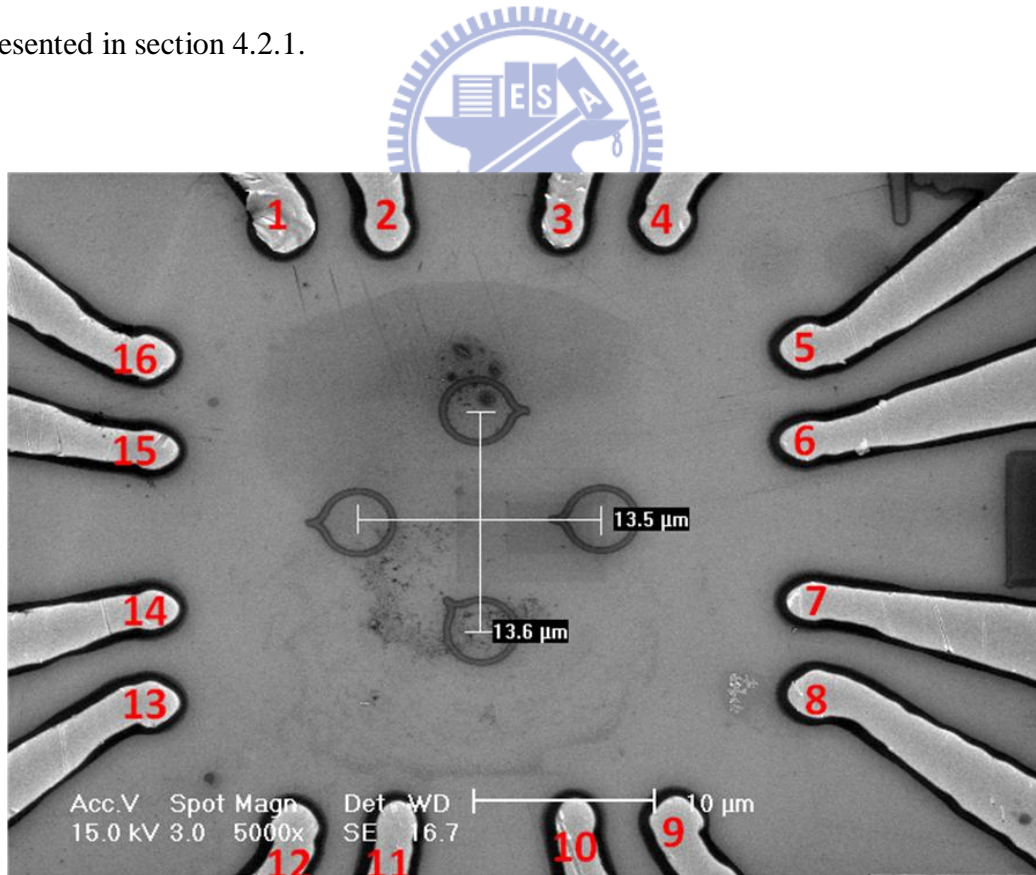


Figure 3.1-1 SEM image of the pad substrate. There are 16 contact pads (labeled by numbers) on a chip substrate. The four rings at the center are magnetic patterns.

3.2 Atomic force microscopy (AFM) and magnetic force microscopy (MFM)

The used AFM/MFM equipment was NT-MDT model Solver P47H. The probes were Nanosensor model PPP-MFMR tips with force constant = 2.8 N/m and resonant frequency = 75 kHz. The scanning method was semi-contact (or tapping) mode with lift height = 80nm between AFM and MFM scans. The schematic illustration of AFM measurement system is shown in Figure 3.2-1.

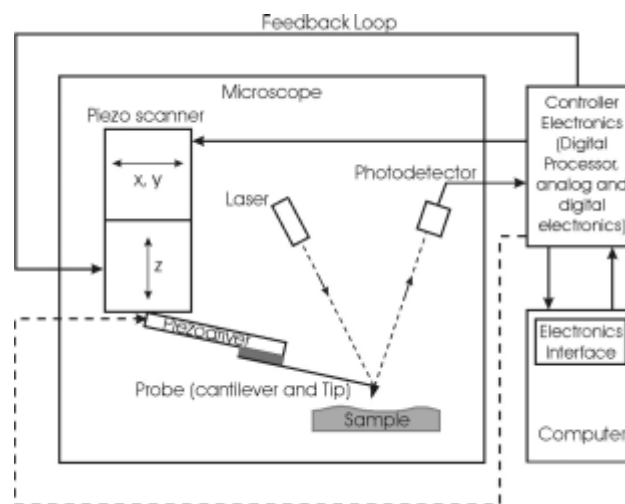


Figure 3.2-1 Schematic illustration of AFM measurement system.

3.3 Magnetoresistance (MR) measurement

The MR measurements were carried out by introducing a constant current with sensing voltage at an external magnetic field. The current was usually less than 0.1 mA for local measurement, and 0.15~1 mA for nonlocal measurement. The field dependence of resistance (R-H loop) was recorded by sampling a value of resistance at a stable magnetic field, and then changed the field to the next one, sampling the next value of the resistance.

Electric measurement For DC measurement, the current source was provided by a Keithley Model 2400 sourcemeter, and the voltage meter was Keithley Model 2000 multimeter whose resolution is $\pm 0.1 \mu\text{V}$. As the devices whose physical signal less than $5 \text{ m}\Omega$ such as NLSV devices, it is hard to obtain clear spin signals by only using Keithley Model 2000 multimeter. Instead, the Keithley Model 2182A Nanovoltmeter whose resolution can reach $\pm 1 \text{ nV}$ is suitable for low signal measurement. Another accurate equipment is the Model LR-700 AC resistance bridge with built-in lock-in technique and an AC current source of constant frequency 16 Hz. The resistance resolution LR-700 is near $\pm 1 \mu\Omega$. For current-induced measurement, however, only DC source can provide pulse (or very short time) current into the magnetic devices. Hence in our studies, either DC or AC source equipments was used to measure the MR.

Measurement of magnetic field In the R-H curve measurement, the resistance value of each sample was measured along with the magnetic field at the same time. This simultaneous field was measured by a magnetic field probe whose analogue signal was converted into digital by the Gauss meter and collected by computers.

The generation of magnetic field The magnetic field was generated by an Tamagawa model TM-YSV5509C-031 electromagnet with provided current $-10 \sim +10 \text{ A}$ by a Kepco power supply model BOP 72-14MG.

CHAPTER 4

4.1 Quantitative analysis of magnetic reversal in patterned strip wire by magnetic force microscopy

4.1.1 Fabrication and measurement of the Permalloy (Py) strip

We fabricated the patterned Py thin film composed of two strip wires with different widths as shown in Figure 4.1-1. The widths of the narrower wire and the wider one were 187 and 463 nm, respectively, and the lengths were 4500 and 5500 nm, respectively, while the thickness was 30 nm. Measurements were performed by AFM/MFM tapping mode to detect the topographic and magnetic images of the pattern at a simultaneously applied magnetic field of $-200 \text{ Oe} \sim 200 \text{ Oe}$ aligned to the longitudinal direction of the strip wires.

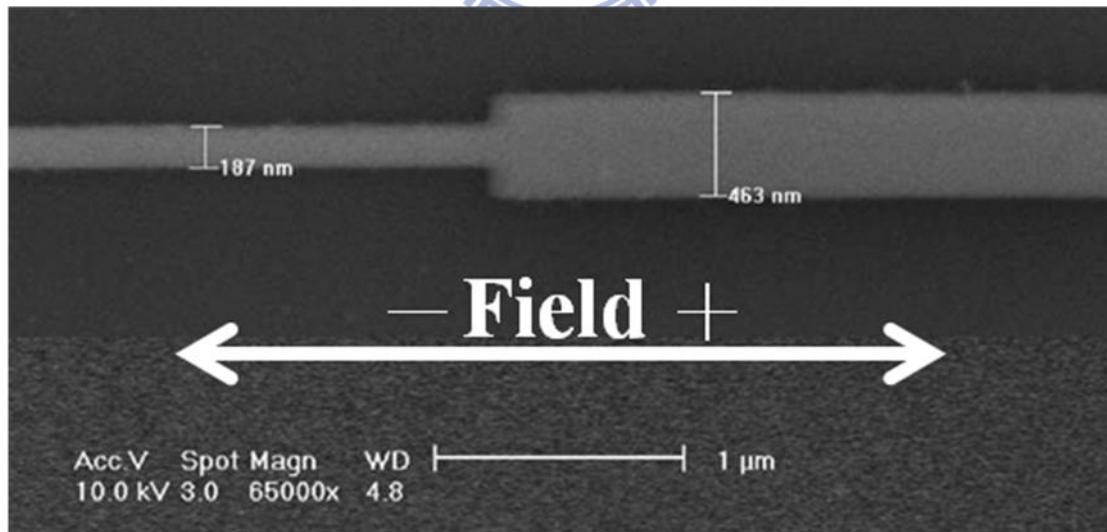


Figure 4.1-1 SEM image of the pattern with different widths of strip wire.

4.1.2 AFM/MFM image at a positive field

Figure 4.1-2(a) shows AFM (upper diagram) and MFM (middle diagram) images, and the profile (lower diagram) of the phase of the line scan in the MFM image as well.

This image was detected at a 140 Oe field which was initially at 250 Oe and varied to -250 Oe. The configuration of magnetization in the pattern (as shown in 4.1-2(b)) is briefly considered as macroscopic uniform, and in the same direction of magnetizations in both parts with different widths. Since only the vertical component of the interactively magnetic force between the MFM tip and the sample contributes to the signals of the MFM image, the relatively darker or brighter signals in the MFM image can only appear at the regions in which magnetic flux strays out of the film plane. In our case, these regions are at both ends of the pattern as well as in the section in which the width changes abruptly. Although the strong anisotropy in long strip wire causes a briefly uniform configuration, this section forms a geometric discontinuity (indicated as b in 4.1-2(b)) in the pattern, thus causing a locally different magnetic configuration and resulting in a stray field out of the film plane. It is reasonable to consider that the magnitude (absolute value) of the phase at the wider section (labelled c) is stronger than that at the narrower one (labelled a), because the quantity of the magnetic moment is proportional to the volume of the magnetic material, and the more moment the material contains, the stronger magnetic flux it radiates into an equal volume of space near the material. Furthermore, in this magnetic configuration, since the section b connects the wider and the narrower parts, which are supposed to have negative and positive values of phase, respectively, the totally combined value is negative (as shown in 4.1-2(a), labeled b). Although it can be reasonably understood that peak c is stronger than peak b (in 4.1-2(a), lower diagram), both in experimental results and theoretical prediction, here we still could not estimate or predict the certain relationship between peak a and peak b without

further quantitative investigation of the relationship between the value of the phase and the magnitude of the stray field.

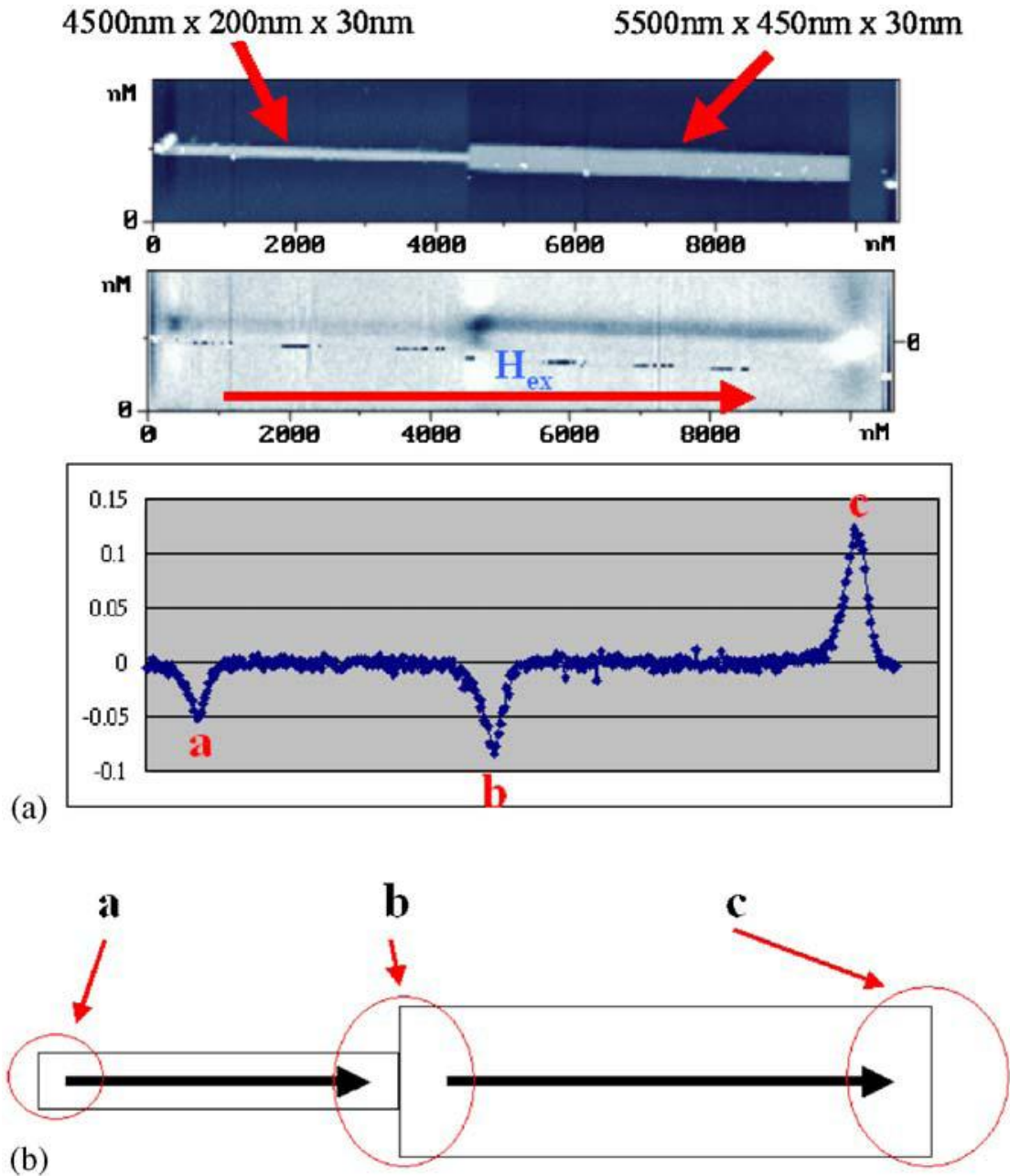
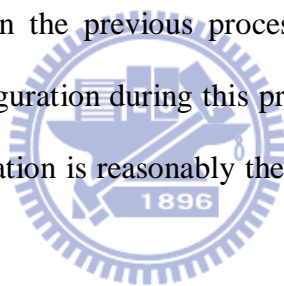


Figure 4.1-2. AFM/MFM image and MFM magnitude of phase. (a) AFM image (upper), MFM image (middle) and a profile (lower) of line scan in MFM image which was observed at a 140 Oe field which was initially at 250 Oe and varied to -250 Oe. (b) A schematic diagram of the magnetic configuration in accordance with that in (a).

4.1.3 Observation of the phase magnitude for full loop

By measuring the completed magnetic reversal loop of the pattern, we analyzed the values of the phases. As shown in Figure 4.1-3(a), the magnetic reversal behaviors in the three sections can be individually separated. During the process of changing in magnetization from field 200 to 15 Oe, the phase intensity remains roughly unchanged. During this process, the value of the phase in section c is positive, that of b is negative, and that of a is also negative. They retain a relationship of peak $c > \text{peak } b > \text{peak } a$. This also means that a certain configuration of magnetization which is in accordance with that in 4.1-2(b) is retained. While in the process of -20 to -200 Oe, the phase values respectively reverse to opposite signs, i.e., c negative, b positive, and a positive (shown in Fig. 3(c), lower diagram), but their absolute values still retain the same relationship mentioned in the previous process. The schematic diagram and MFM image of magnetic configuration during this process are shown in 4.1-3(b) and (c), respectively. This configuration is reasonably the opposite direction of that in the previous process.



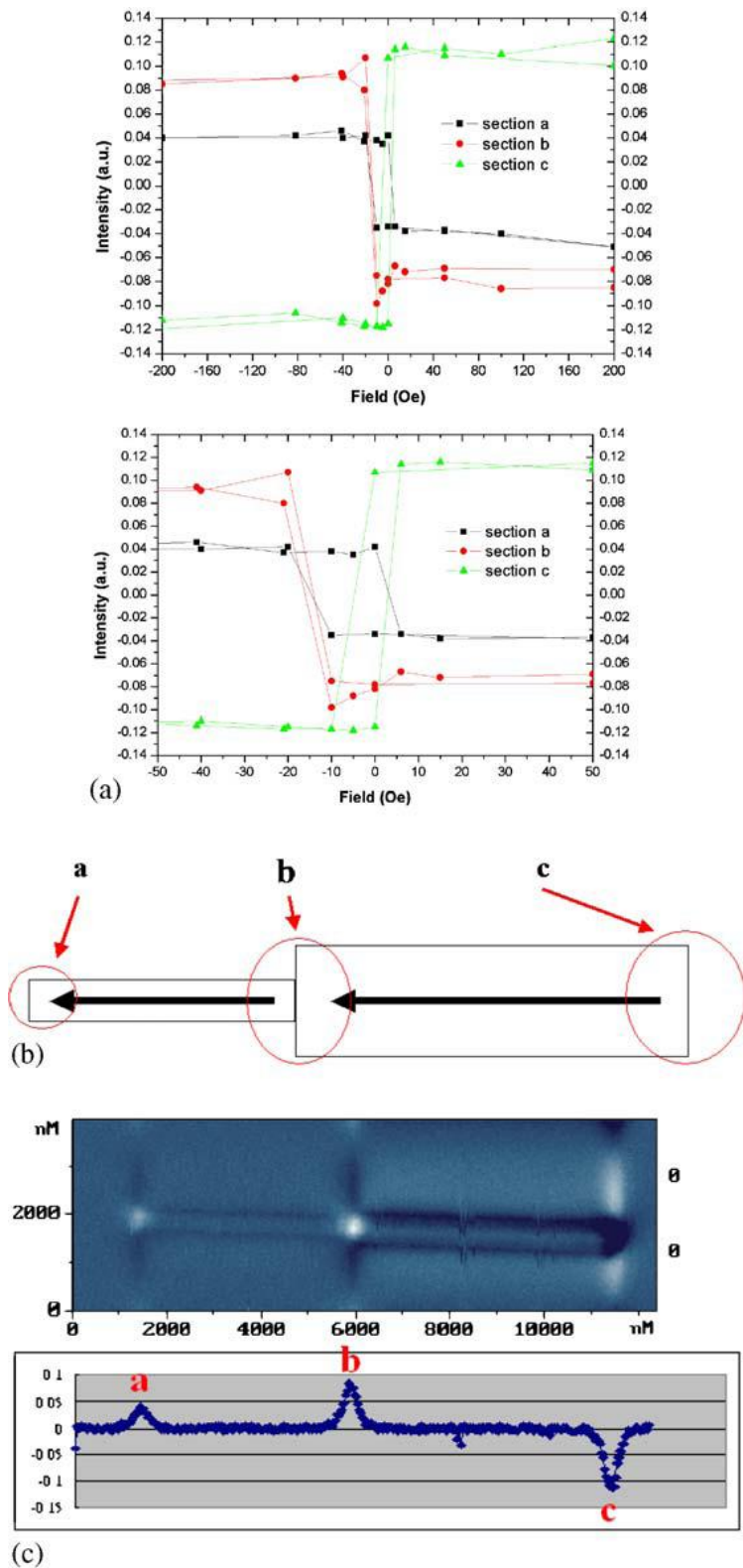


Figure 4.1-3 Phase magnitude for full loop and MFM image at a negative field. (a) Magnetic hysteresis loops (upper) for different local sections presented in values of phase; its zoom in (lower). (b) Schematic diagram of the configuration of the magnetization in the magnetic process of -20 to -200 Oe. (c) MFM image (upper) at -200 Oe and profile (lower) of the line scan in the MFM image.

4.1.4 Evaluation of the individual sections

The absolute values of the phases were presented with the longitudinal distance in the pattern, as shown in Figure 4.1-4. As we mentioned above, phase-shift can obviously present only in the regions in which magnetic flux strays out of the film plane. Since sections c, b, and a radiate relatively strong magnetic fluxes, the phase intensities (absolute values) appear more evidently at the centers of these regions, and rapidly decrease at areas away from the centers. The result of analysis of phase intensity shows that the magnitude is about 0.05 in section a, 0.09 in b, and 0.117 in c. After normalization (choosing 0.117 as 1), we have 0.427 in a, 0.769 in b, and 1 in c. In addition, the width in section a is about 200 nm, and that in section c about 450 nm, hence the volume ratio of about 0.44. That means the ratio of the quantity of magnetic moment contained in sections a to c might be near 0.44, slightly in accordance with the value 0.427 (the ratio of phase intensity in sections a to c).

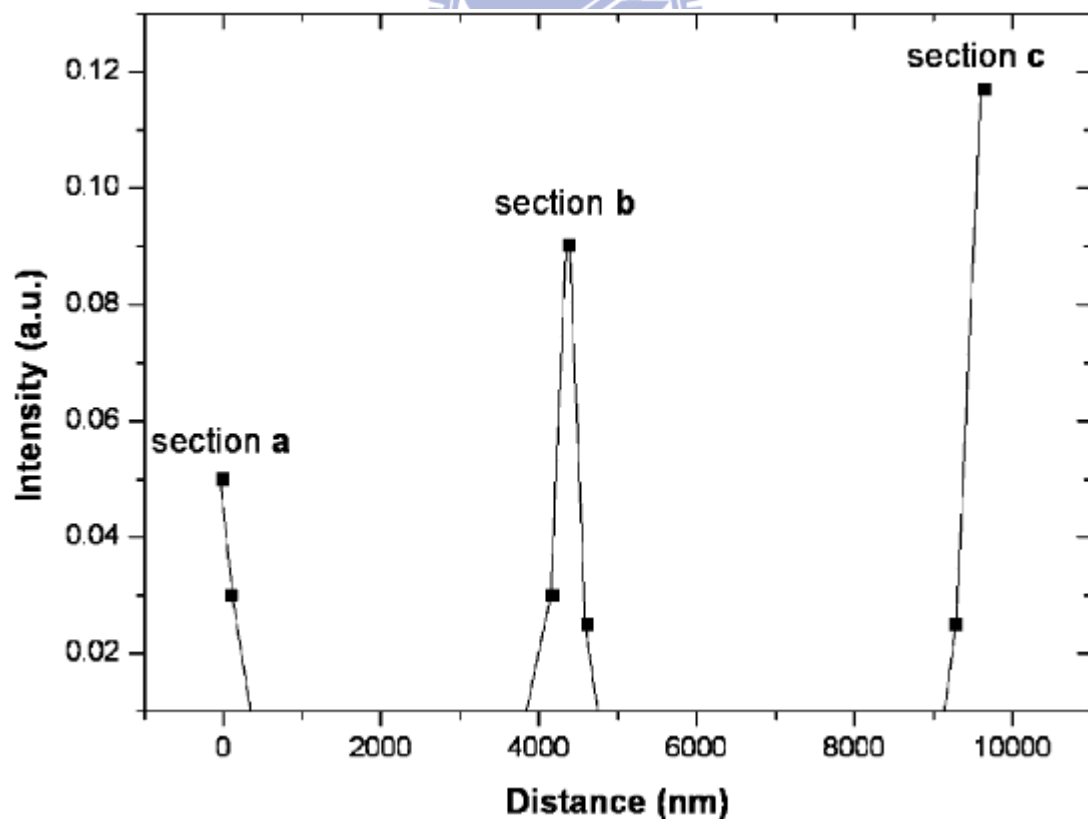


Figure 4.1-4 Phase intensity (absolute value) varying with distance in the pattern near the magnetic saturation (20 ~ 200 Oe and -20 ~ -200 Oe).

Furthermore, the switching field (H_c , or coercive force) for each individual local section is also analyzed with the distance in the pattern, as shown in Figure 4.1-5. The diagram shows that H_c in sections a and c are 9 and 8 Oe, which is much larger than that in section b, in which H_c is almost zero. Additionally, at the areas away from the centers of these sections, there is no so-called switching field, since at these areas there is not even an identifiable hysteresis loop observed. Our results are quite consistent with previous reports [105-107]. Due to the shape anisotropy, the value of the H_c should strongly depend on the width of the wire; therefore, we have quantitatively determined the H_c in sections a, b, and c.

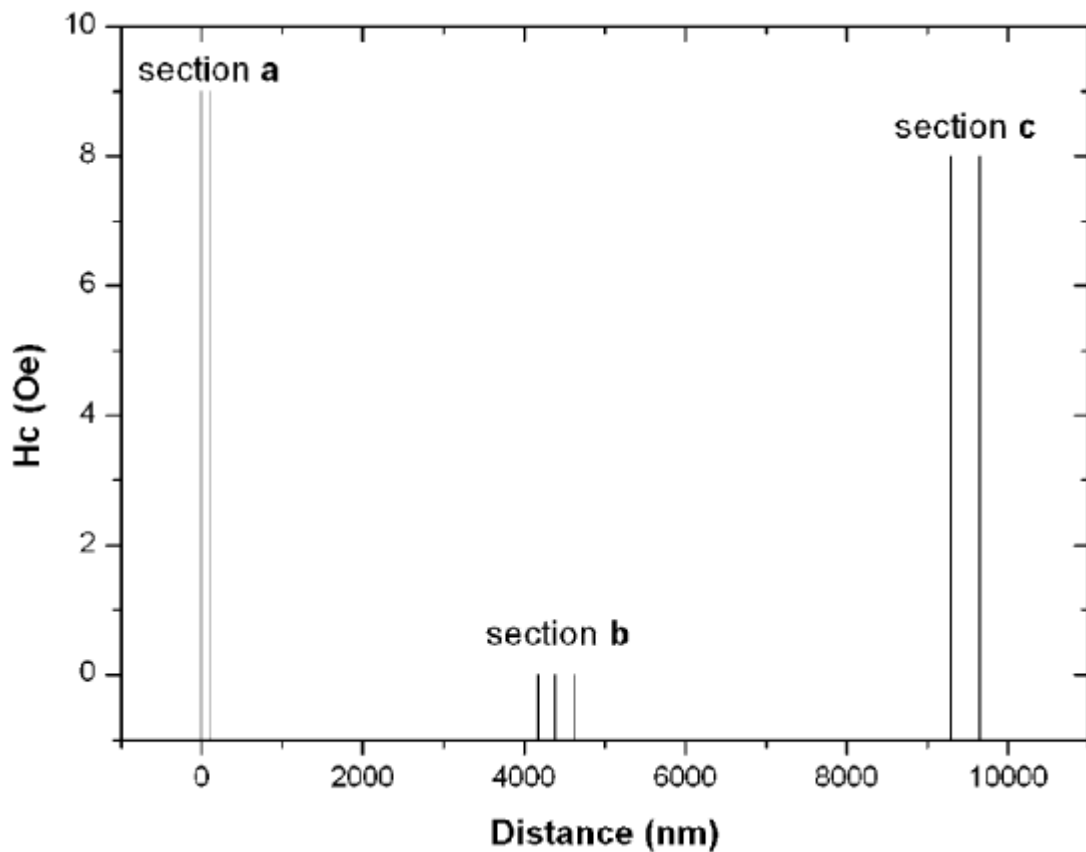


Figure 4.1-5 The switching field (or coercive force) H_c for each individual local section.

4.1.5 Lists of the phase magnitudes and MFM images

We have demonstrated that the magnetic behaviors in different local sections of a patterned strip wire can be individually separated and compared with each other. The intensity of the phase-shift in the wider end is stronger than that in the narrower one. In contrast, the coercive force (which is defined by the reverse in the signs of the values of phase-shifts) in the narrower end (9 Oe) is larger than that in the wider one (8 Oe). This is due to a strong anisotropic effect, and thus the H_C in the neck section (i.e., section b) could become strongly affected by the competition of the head-to-tail magnetic configurations in the two parts of the strip wire. This results in a small H_C in the neck section. Furthermore, with a simple neck shape connection in a strip Py wire, we can easily to change a single domain configuration to a two single domain magnetic configuration. Finally, we list the phase magnitudes and the MFM images with its corresponding AFM images below.

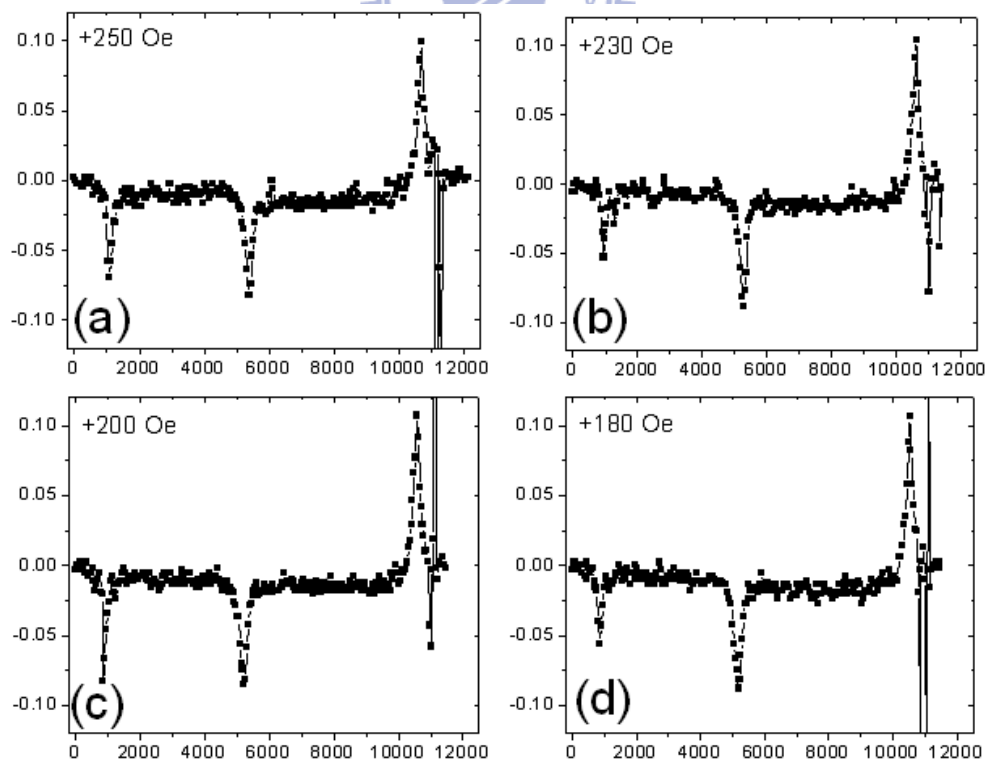


Figure 4.1-6 List of phase magnitudes at different field (a) ~ (d) for +250, +230, +200, and +180 Oe.

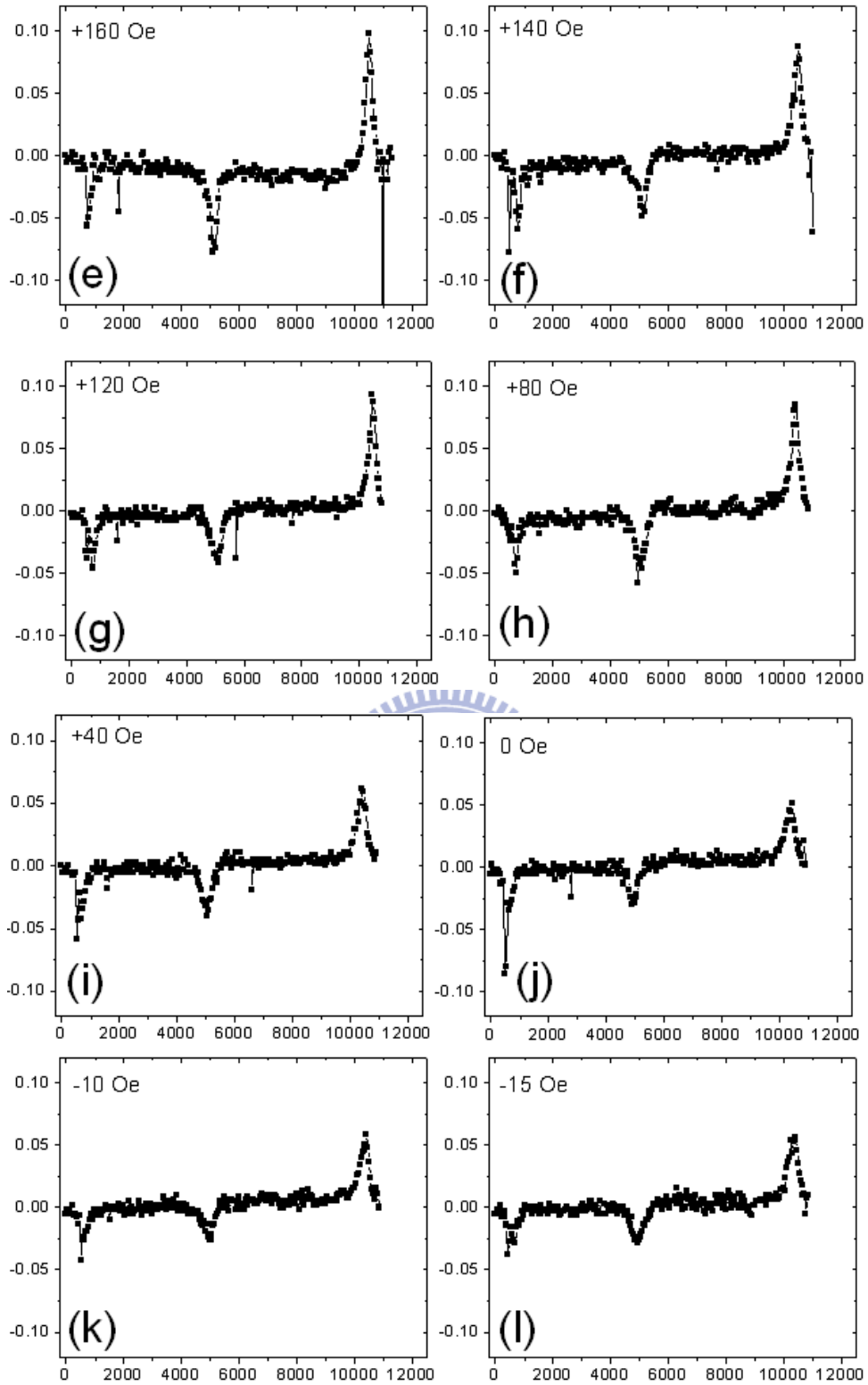


Figure 4.1-6 List of phase magnitudes at different field (e) ~ (l) for +160, +140, +120, +80, 40, 0, -10, and -15 Oe.

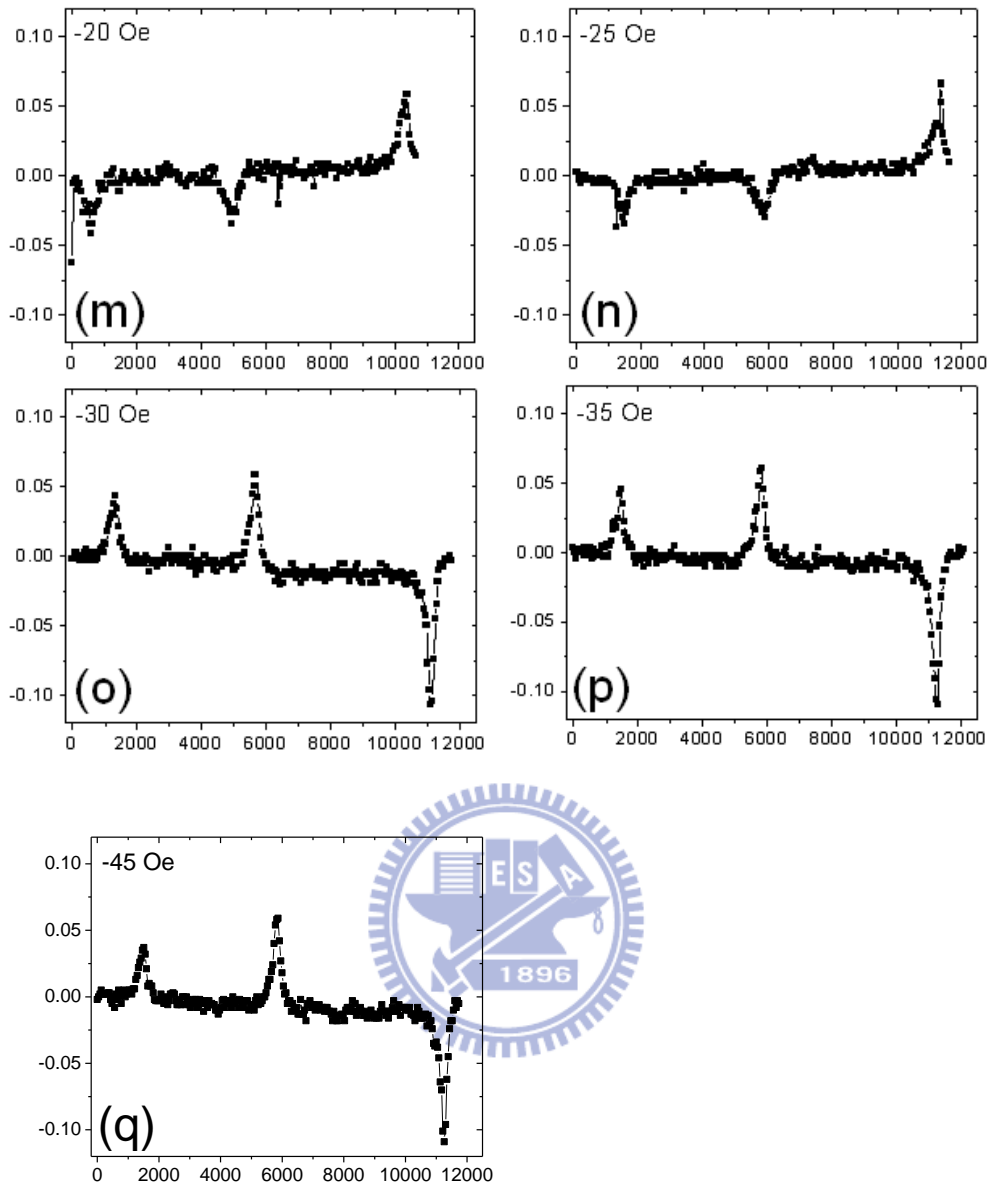


Figure 4.1-6 List of phase magnitudes at different field (m) ~ (q) for -20, -25, -30, -35, and -45 Oe.

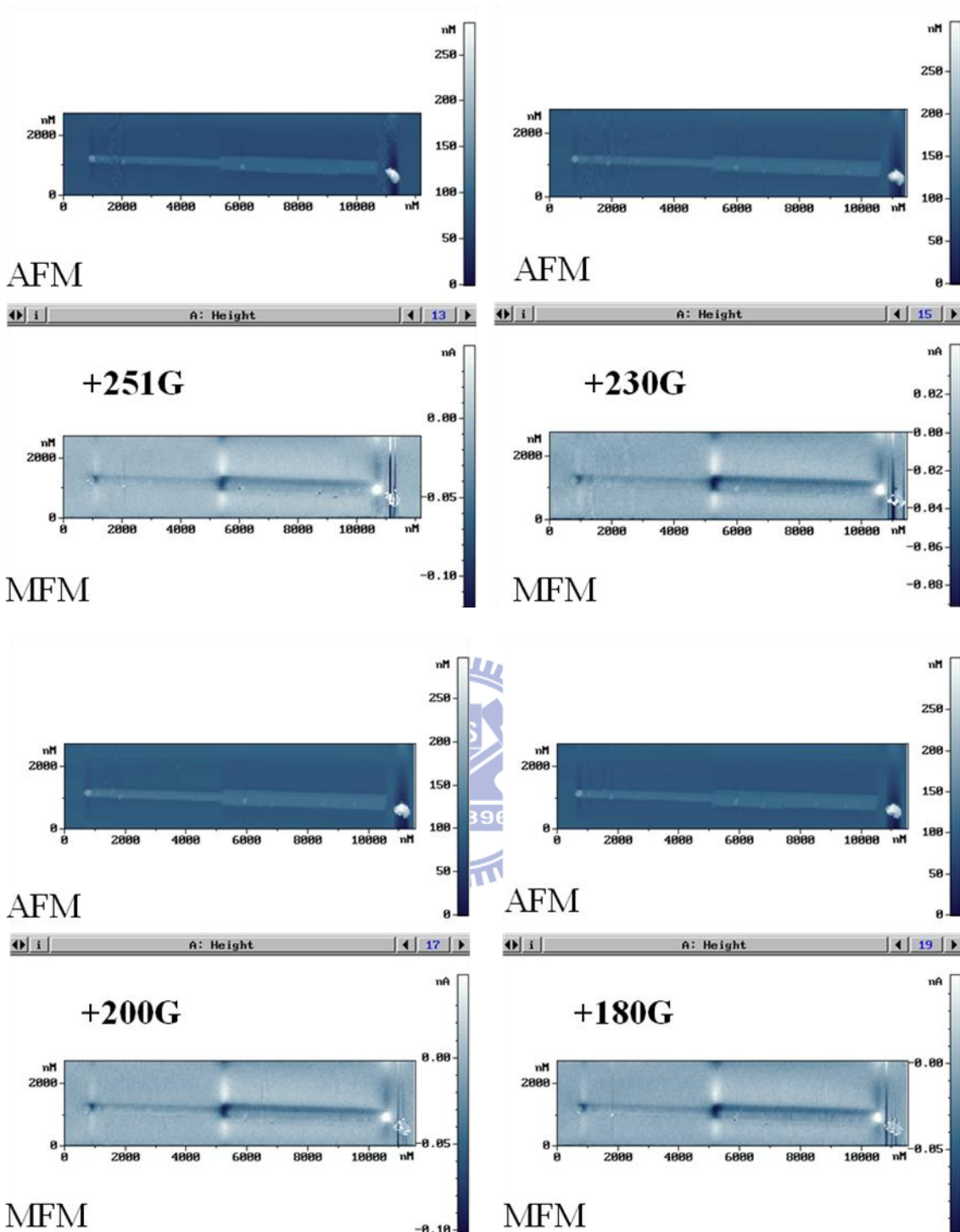


Figure 4.1-7 List of AFM/MFM images at different field: +250, +230, +200, and +180 Oe.

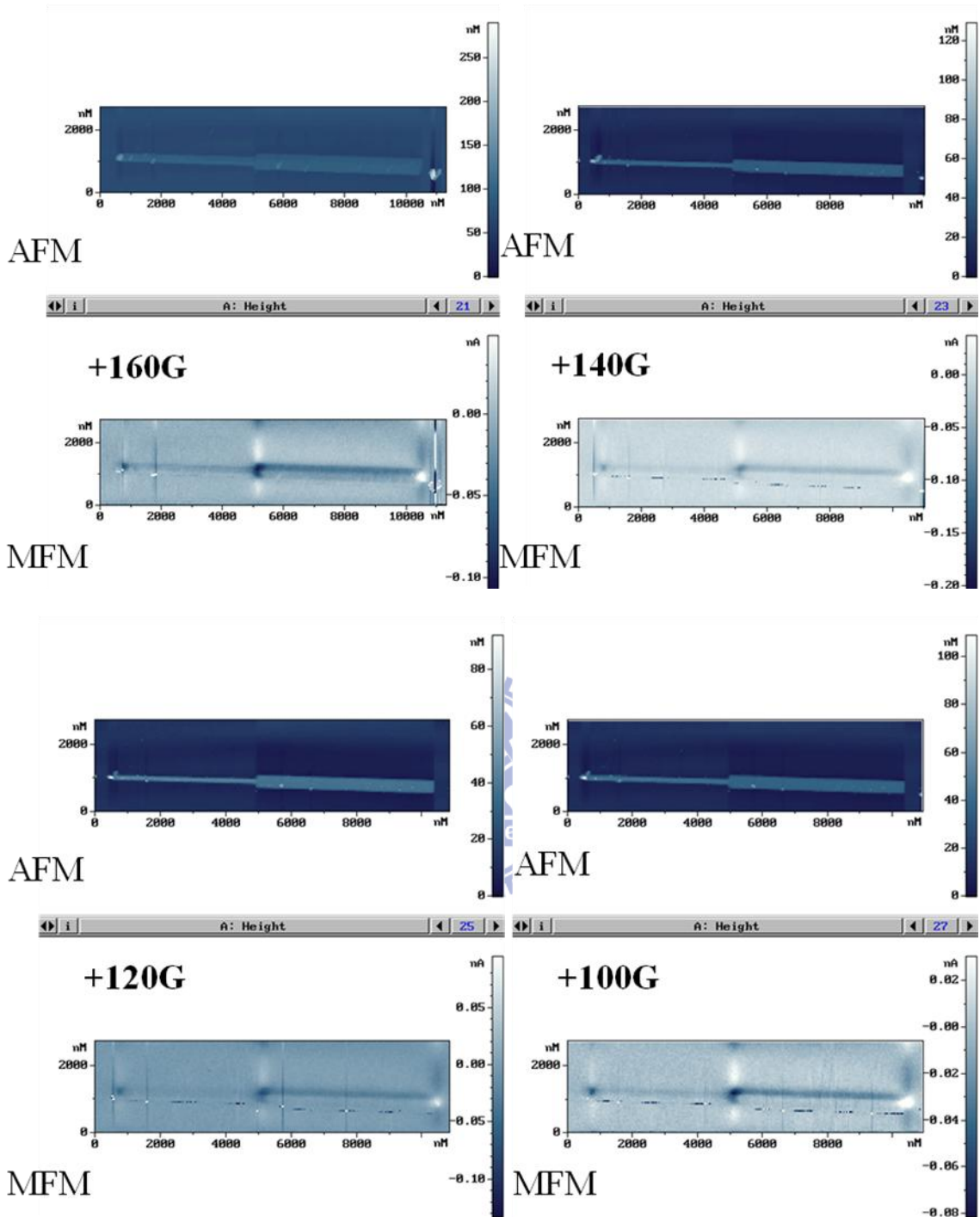


Figure 4.1-7 List of AFM/MFM images at different field: +160, +140, +120, and +100Oe.

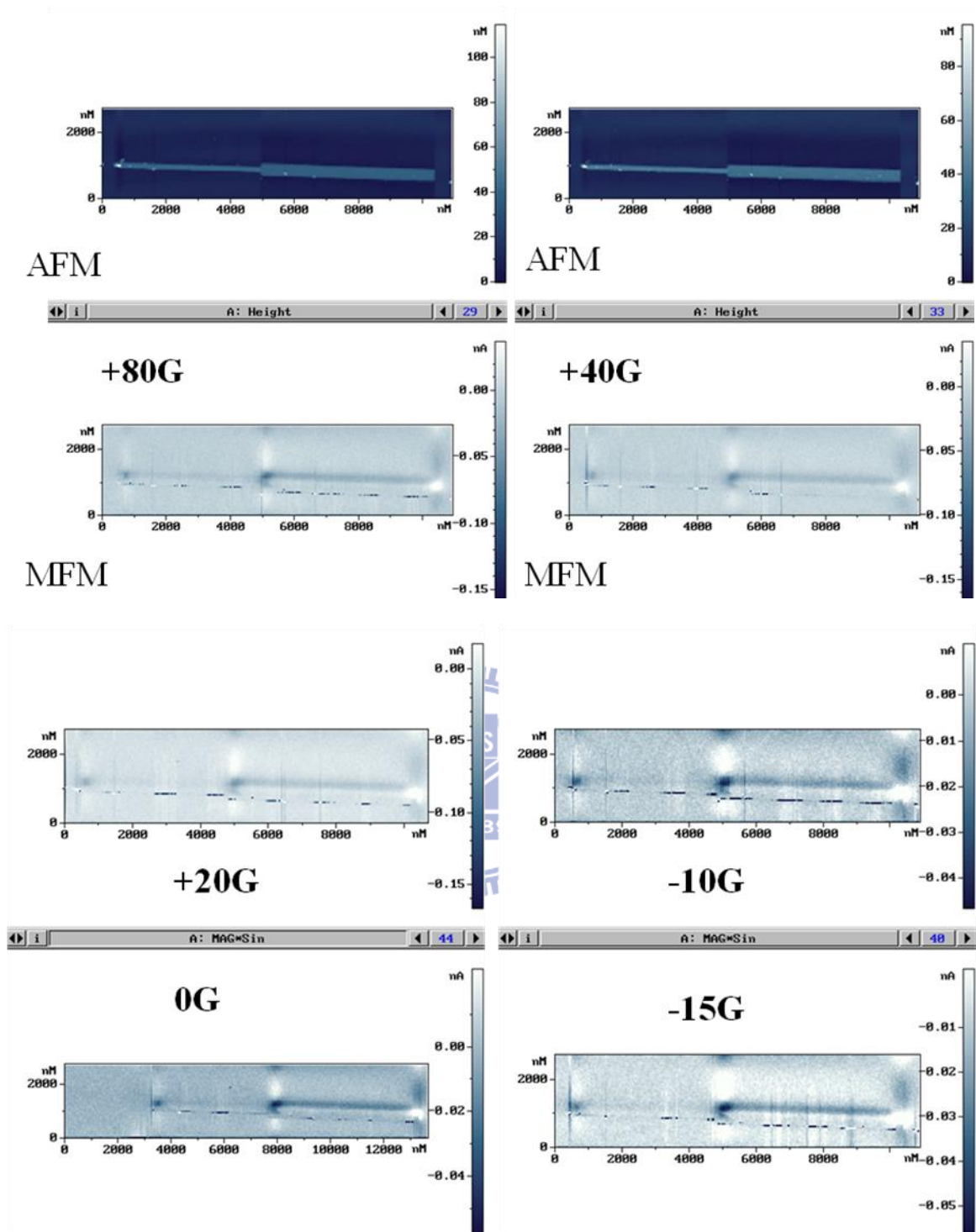


Figure 4.1-7 List of AFM/MFM images at different field: +80, 40, 20, 0, -10, and -15 Oe.

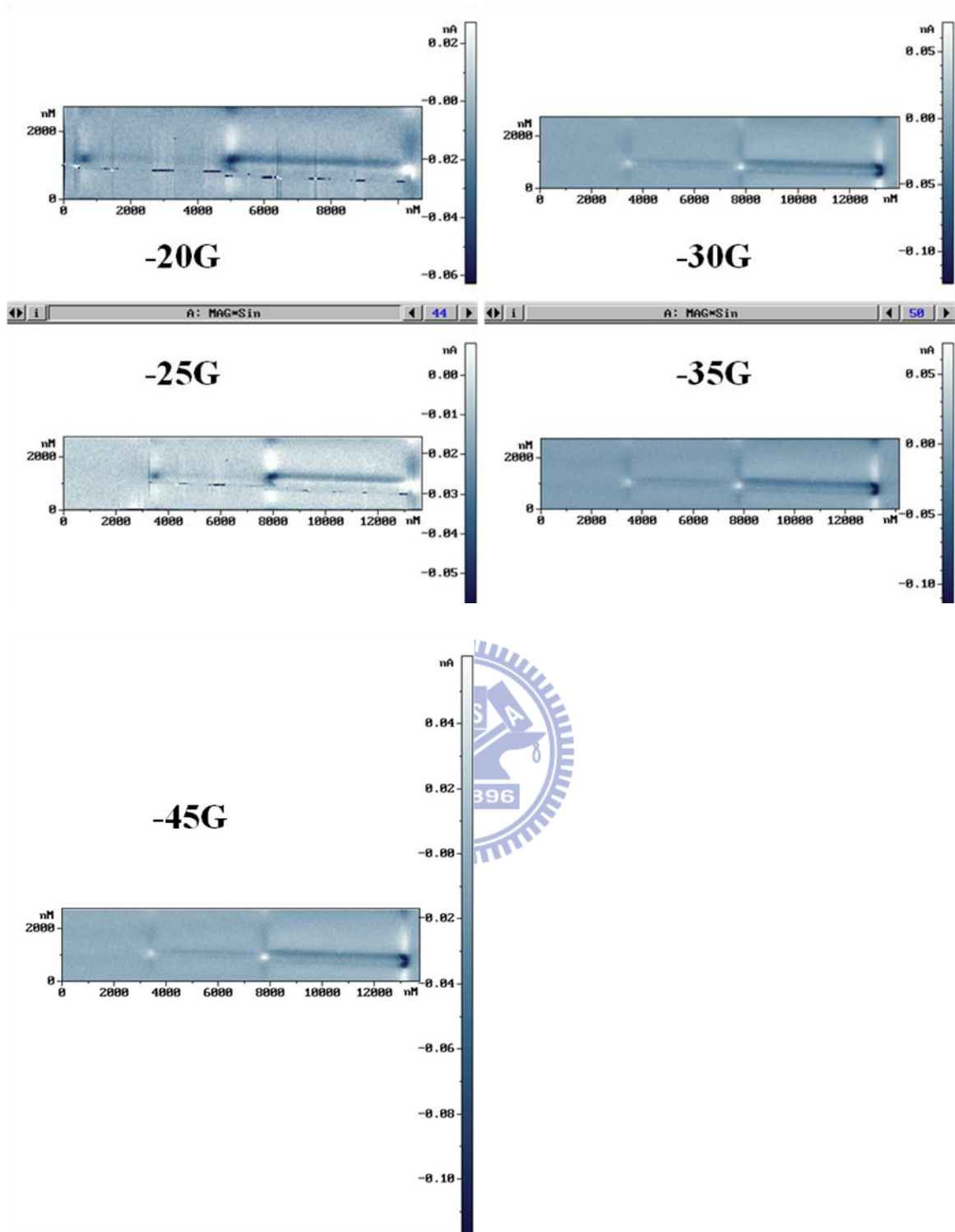


Figure 4.1-7 List of AFM/MFM images at different field: -20, -25, -30, -35, and -45 Oe.

4.2 Thermal effects on magnetoresistance of magnetic tunnel junction

4.2.1 Structure of MTJ and measurement

The MTJ cell with elliptic shape were studied (Figure 4.2-1). Standard commercial manufacturing processes including photolithography, oxidization, etching, and metallization were used to prepare the samples. SiO₂/Si were chosen as the substrate, and multiple metal layers were deposited on substrates by sputtering. For structure **2**, the first layer is Ta (20nm) used as a bottom electrode. PtMn (15nm) serves as an antiferromagnetic layer which pins the following tri-layered synthetic antiferromagnet (SAF) structure, CoFe(2nm)/Ru(0.8nm)/CoFe(3nm). During the depositing of PtMn layer, an external magnetic field was also applied to define the direction of magnetization of antiferromagnetic layer. Due to the exchange coupling effect, the two CoFe layers in tri-layered SAF structure can be aligned at anti-parallel with each other, and hence the tri-layered SAF structure can be used as a pinned layer. The insulator layer was made of Al-O_x (~1.2 nm) which was manufactured by pre-depositing an Al thin layer (~9 Å) followed by introducing O₂ gas for 25~30 seconds to oxidize the Al layer. Then CoFe(1nm)/NiFe(3nm) bilayer is deposited to serve as a free layer. Finally, Ta (60nm) was deposited as the top electrode layer. In order to ensure the function of the PtMn layer, a process of magnetic annealing was applied to the wafer. The condition of magnetic annealing was at 275 °C, and 8000 Oe for 5 hours. After thin film depositing, the process of photolithography and dry etching were used to pattern the MTJ structure and testing circuits. Electrical properties including TMR and current-voltage relation (I-V curve) were measured by using a DC source at various temperatures from 25°C through 140°C and magnetic field aligned to long axis of ellipse of the MTJ cell.

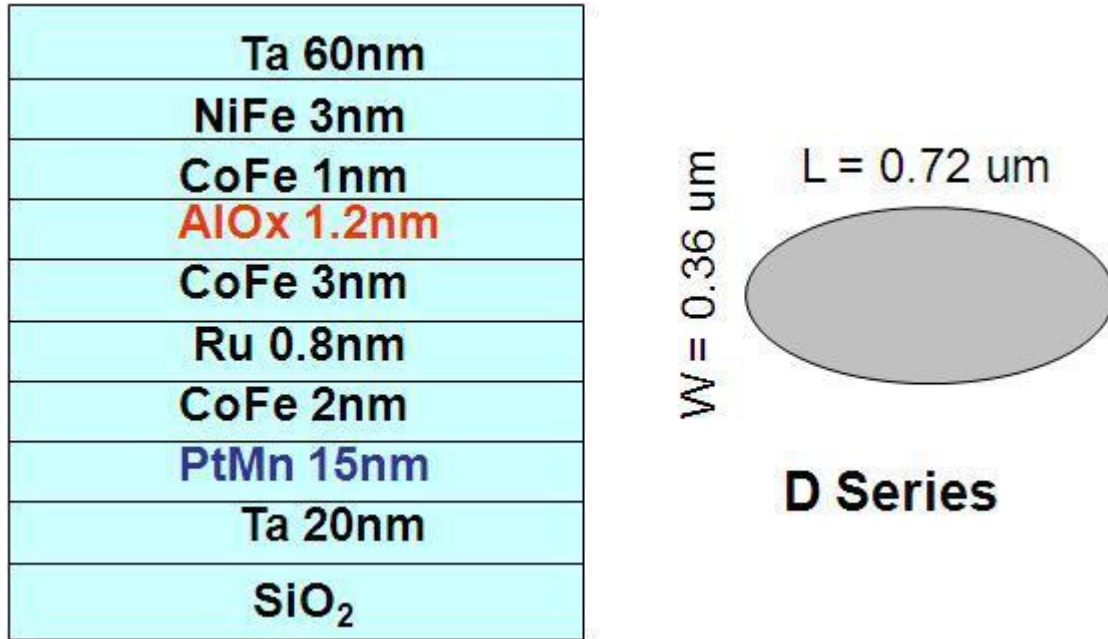


Figure 4.2-1 Layered structure and lateral size of the MTJ cell.

4.2.2 Temperature-dependent TMR measurement

Typical TMR minor loop with only free layer switching at room temperature is shown in Figure 4.2-2. The applied voltage is 50 mV and MR ratio about 33.25%. Temperature dependence of TMR loop of MTJ is shown in Figure 4.2-3. The whole loop shifts to low resistance with temperature climbing up. MR ratio behaves in a similar tendency to the resistance (Figure 4.2-4). To more clearly inspect the MR behavior, we extract the resistance for P and AP configuration separately, and compare them with each other (Figure 4.2-5). It indicates that the resistance for AP configuration decreases faster than that for P configuration with temperature, and hence resulting in the decline tendency of MR ratio. Dependence of difference in resistance (ΔR) between the two configurations on temperature is shown in Figure 4.2-6 to be compared with MR ratio. Both roughly exhibit linear relation with temperature from 25 to 140°C.

Coercivities of free layers were also extracted out from MR loops. The coercivity

decreases by 35% from room temperature to 140°C (Figure 4.2-7). Another important thermal effect is the annealing effect. Compared to the intentionally annealed process of MTJ devices, in which the annealing temperature is usually higher than 200°C to about 350°C, 130°C~ 140°C is considerably low temperature and could not crucially influence the material structure in MTJ. It is still our interest to explore the non-intentionally annealing effect on MTJ devices, i.e., the encountered temperature higher than room temperature could more or less affects the performance of the devices during operation or other post-stepped manufacturing. Figure 4.2-8 shows the resistance variation with annealing temperature for P and AP configurations. Not surprisingly, the resistance behaves no obvious changes and the MR ratio varies by less than 1% in normalized ratio (Figure 4.2-9).

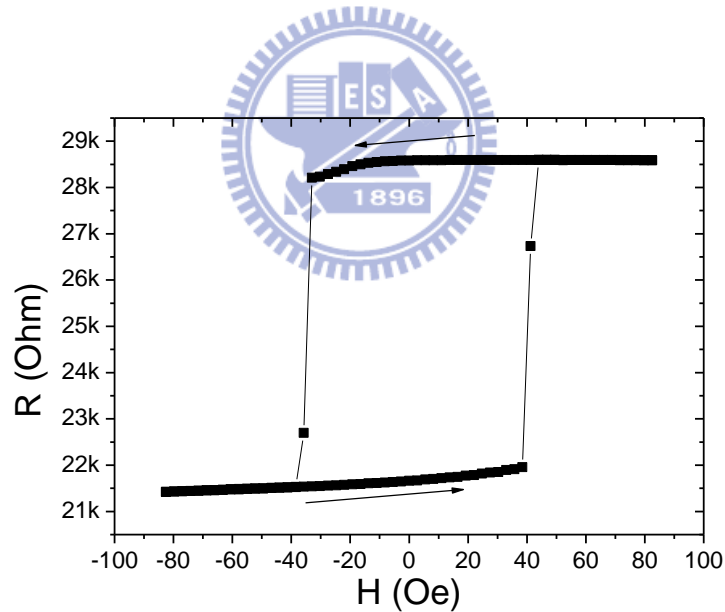


Figure 4.2-2 Typical TMR minor loops measured at 50 mV and room temperature.

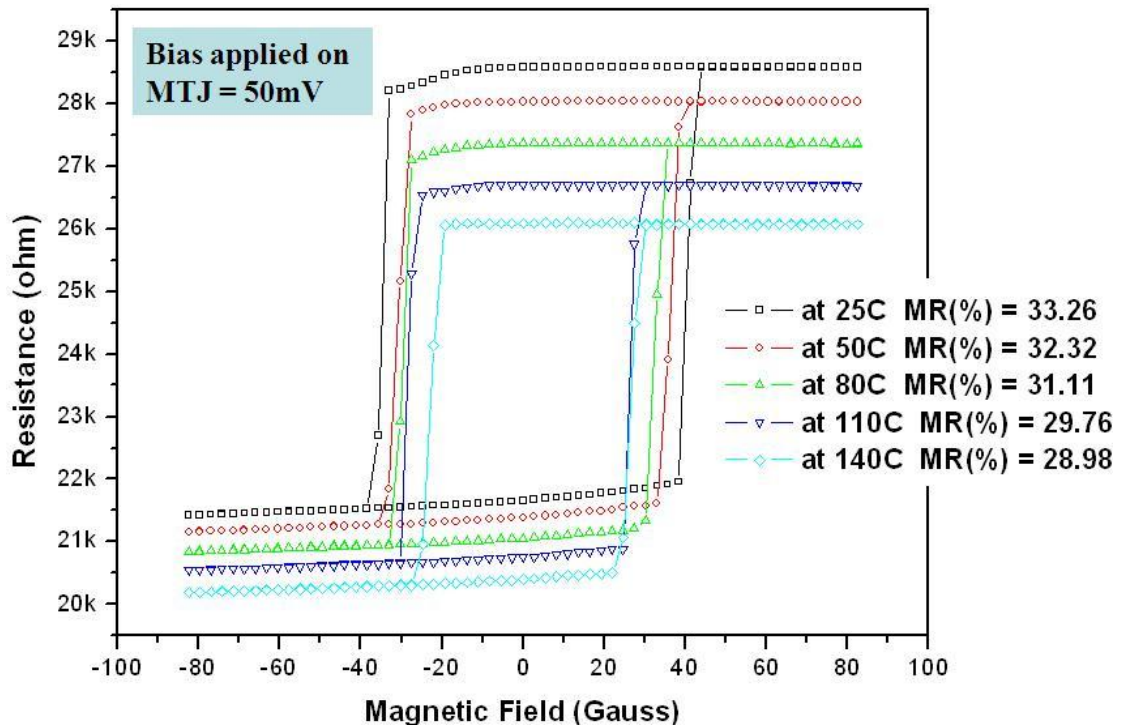


Figure 4.2-3 Temperature dependence of TMR loop.

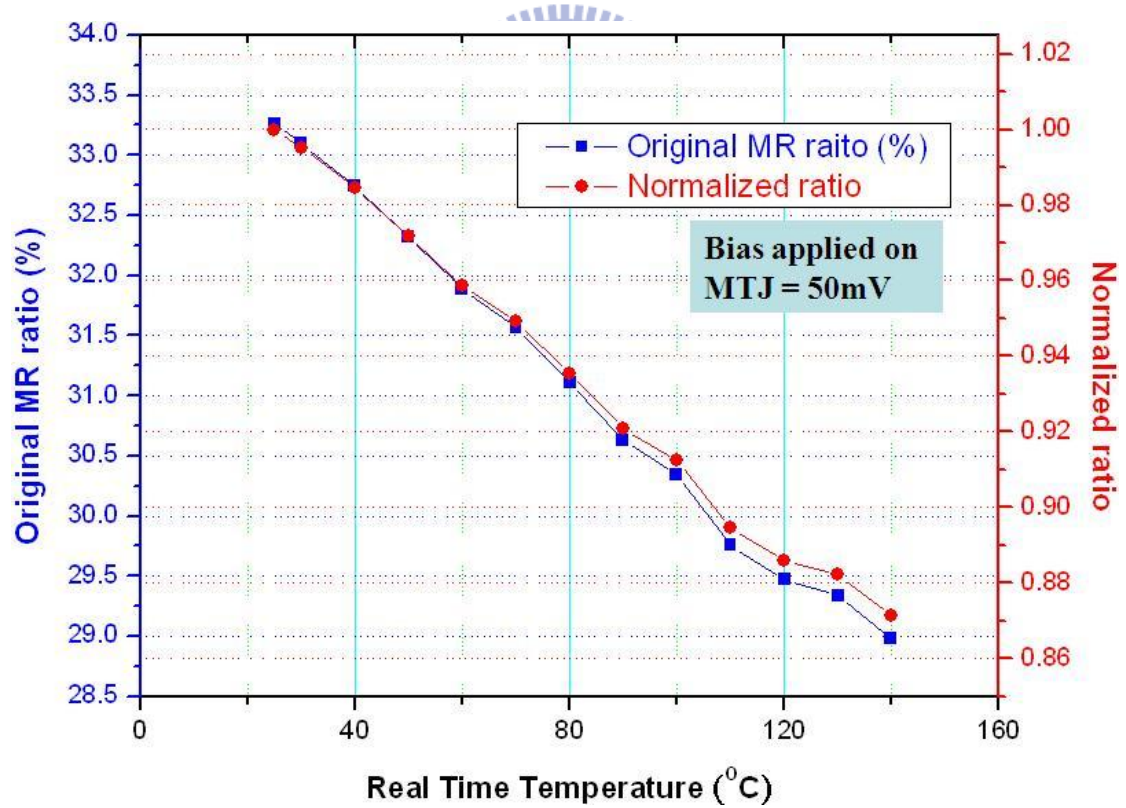


Figure 4.2-4 Temperature dependence of TMR ratio.

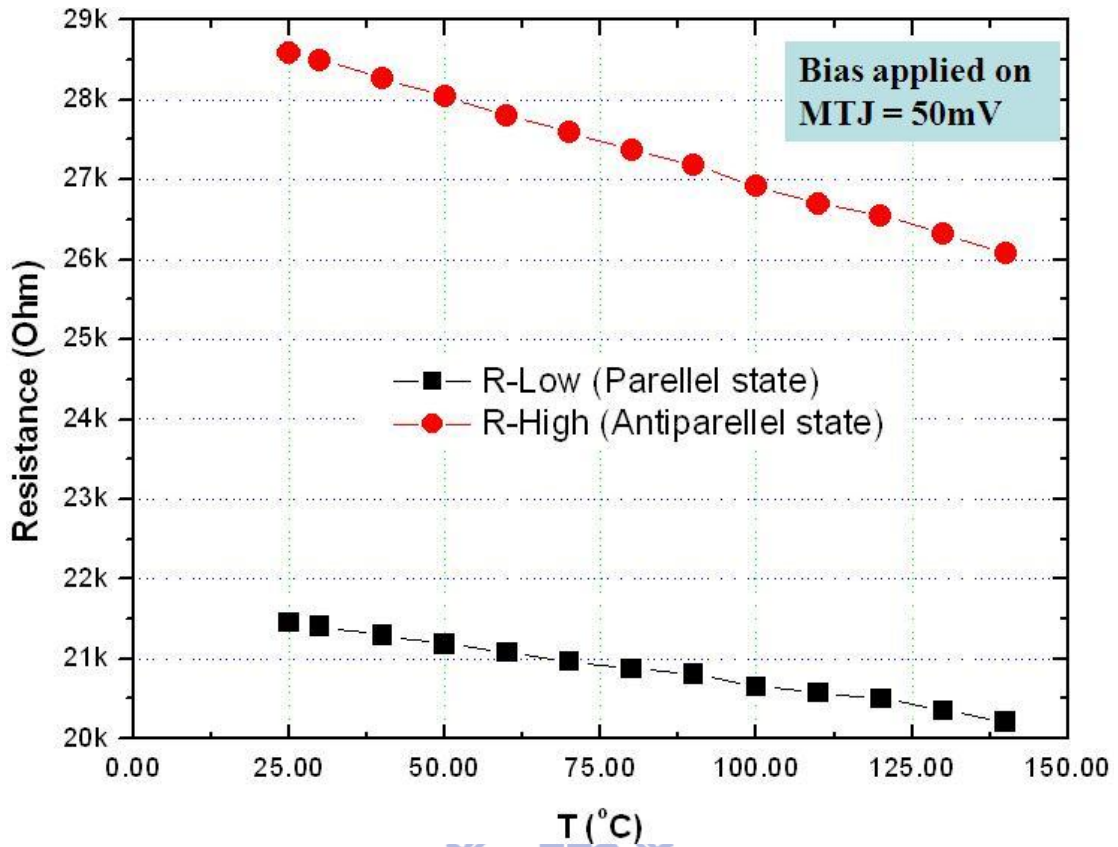


Figure 4.2-5 Temperature dependence of resistance for P and AP configuration.

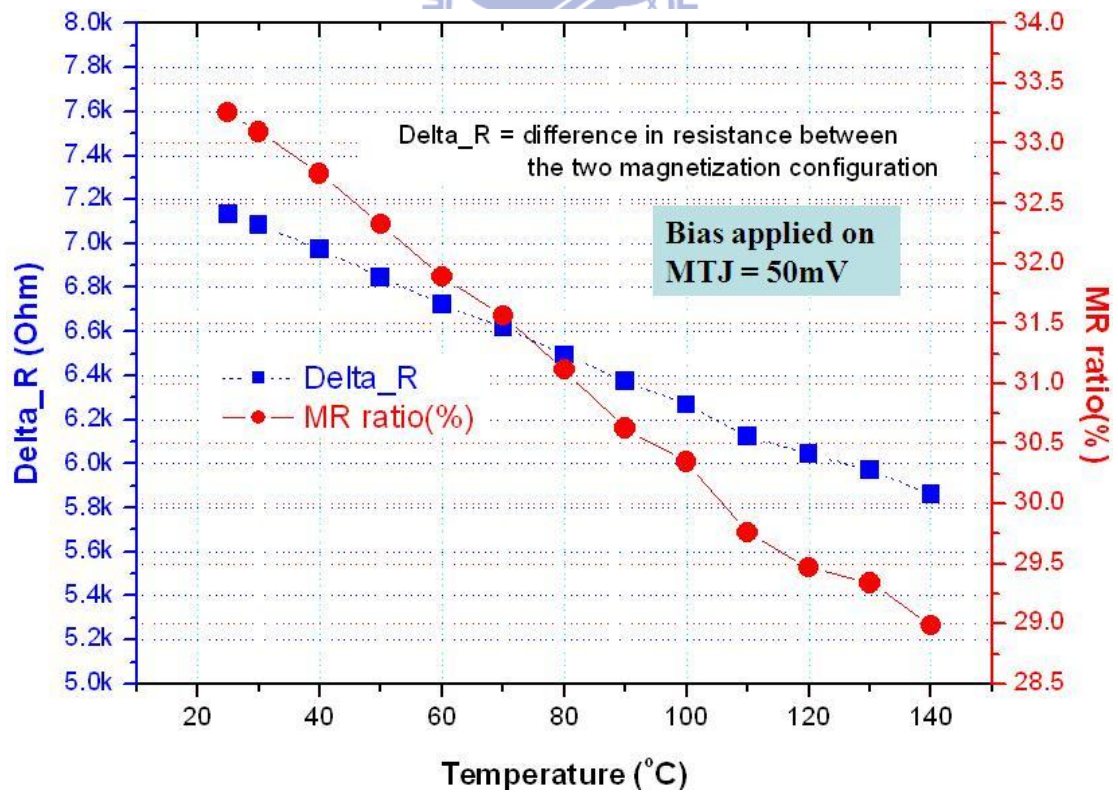


Figure 4.2-6 Comparison of ΔR and MR%.

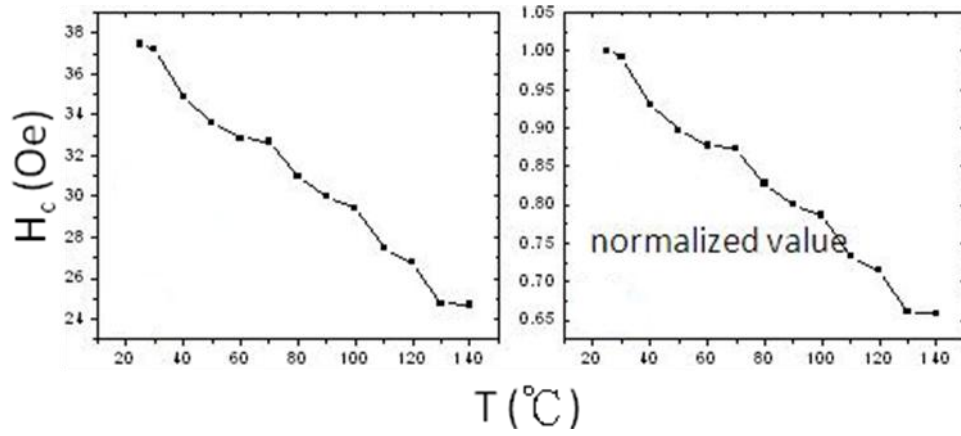


Figure 4.2-7 Coercivities variation with temperature. Left: original value. Right: normalized value.

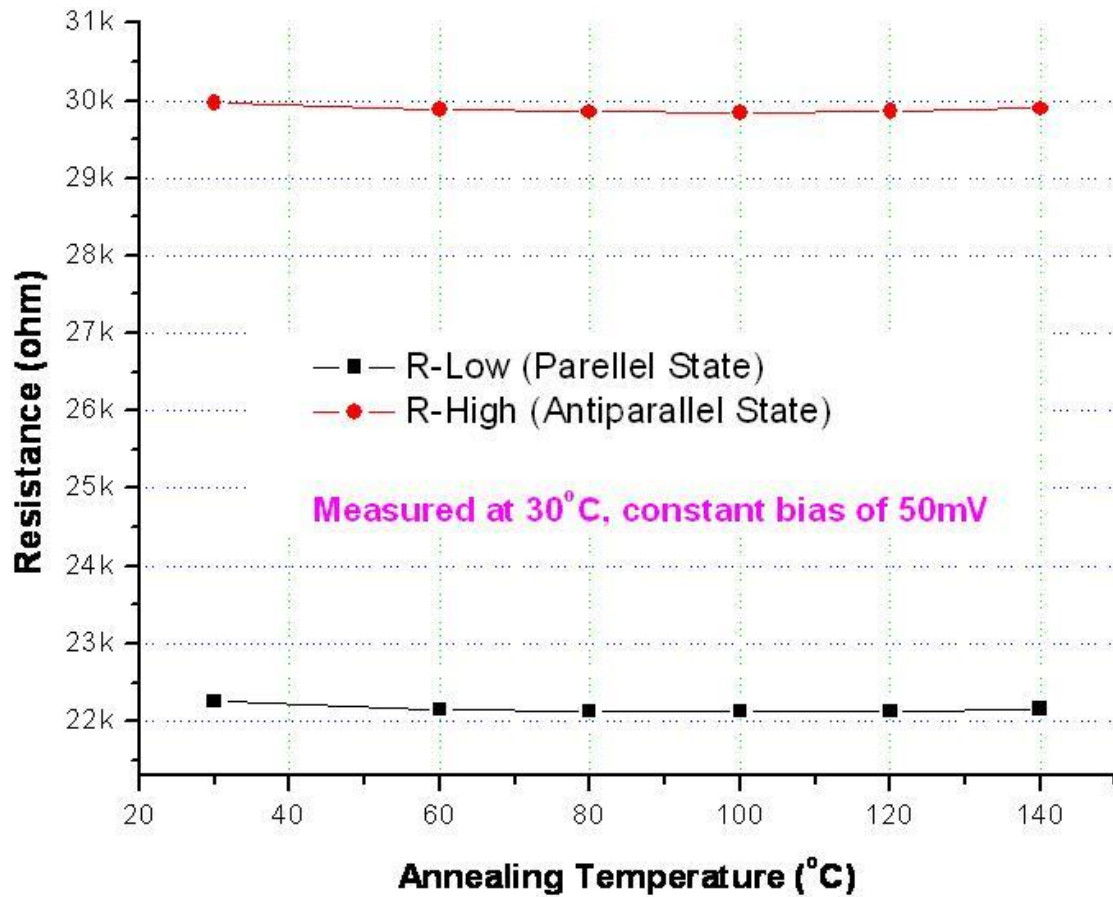


Figure 4.2-8 Annealing effect on resistance.

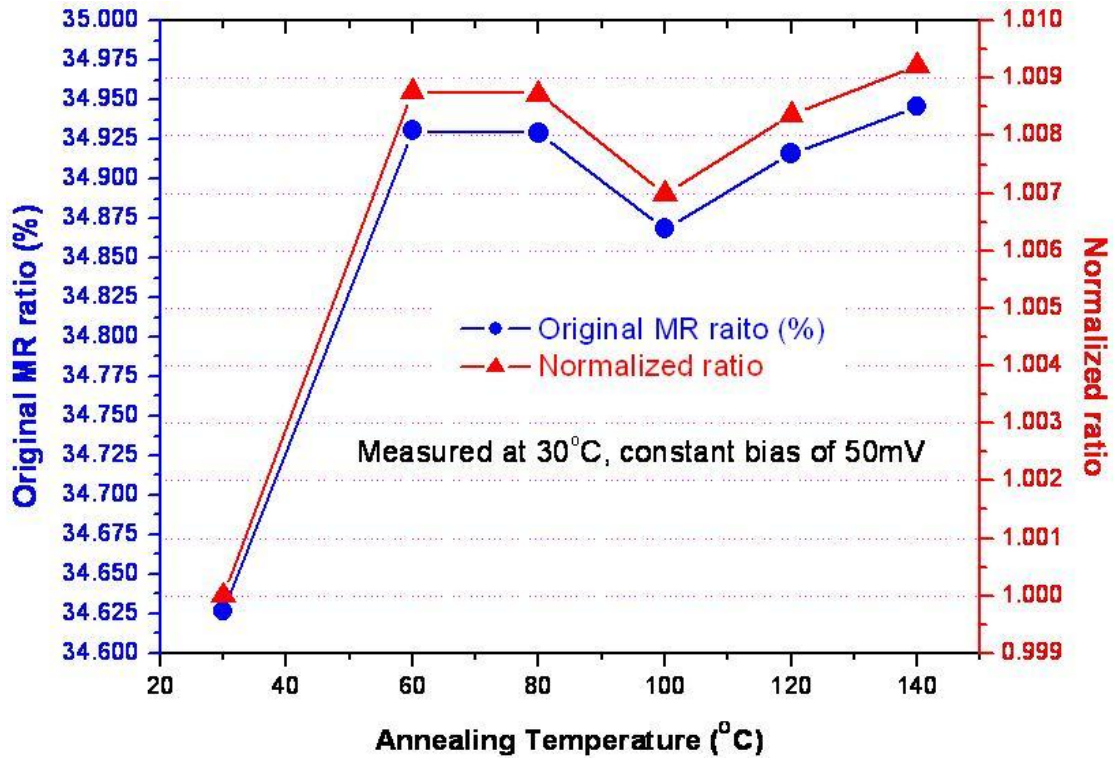


Figure 4.2-9 Annealing effect on MR ratio.

4.2.3 Bias-dependent TMR measurement

MR loops of the MTJ device was measured with changing bias voltage from 5 mV to 1.2 V. For detailed inspection of each loop, the data are separated into several diagrams (Figures 4.2-10 (a) ~ (j)), and the loops of full voltage range are shown in Figure 4.2-10 (k) to observe the tendency of bias-dependent MR loop. In the same trend with the temperature dependence, the whole MR loop also shifts towards low resistance with increasing bias voltage. The current-voltage measurement (I-V curve) was also carried out, and the dynamic conductance (dI/dV) was derived to further understand the relation between MR ratio and the density of states (DOS) of the two ferromagnetic layers on both sides of the tunnel barrier.

Figure 4.2-11 shows the typical TMR I-V curves for P and AP configuration at room temperature. It is easily to obtain the dynamic conductance, dI/dV , by

differentiating I with V . The dI/dV - V relation in Figure 4.2-12 shows an obvious difference between AP and P configurations. For P configuration, a conductance minima shifts (CMS) appears at around 250 mV which is significantly larger than that for AP configuration. This obvious asymmetry about zero bias ranges between -0.9 V \sim $+0.9$ V. On the contrary, the AP configuration exhibits more symmetric about zero bias than P configuration. The CMS for AP is less than 5 mV. Such a spin-dependent asymmetry is reasonably considered as the contribution from the variation of DOS of ferromagnetic layers on both sides of the tunnel barrier (oxide layer).

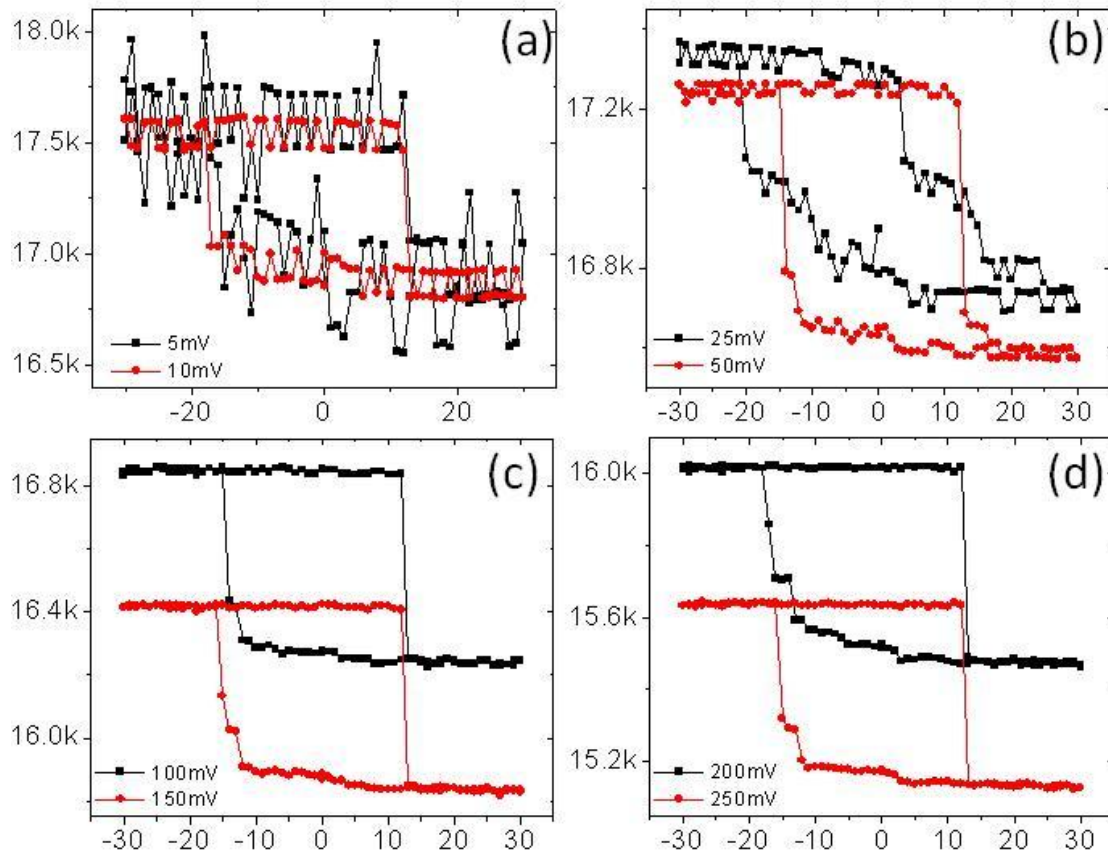


Figure 4.2-10 Series of bias-dependent MR loops. (a)~(d) for bias voltage of 5 mV \sim 250 mV.

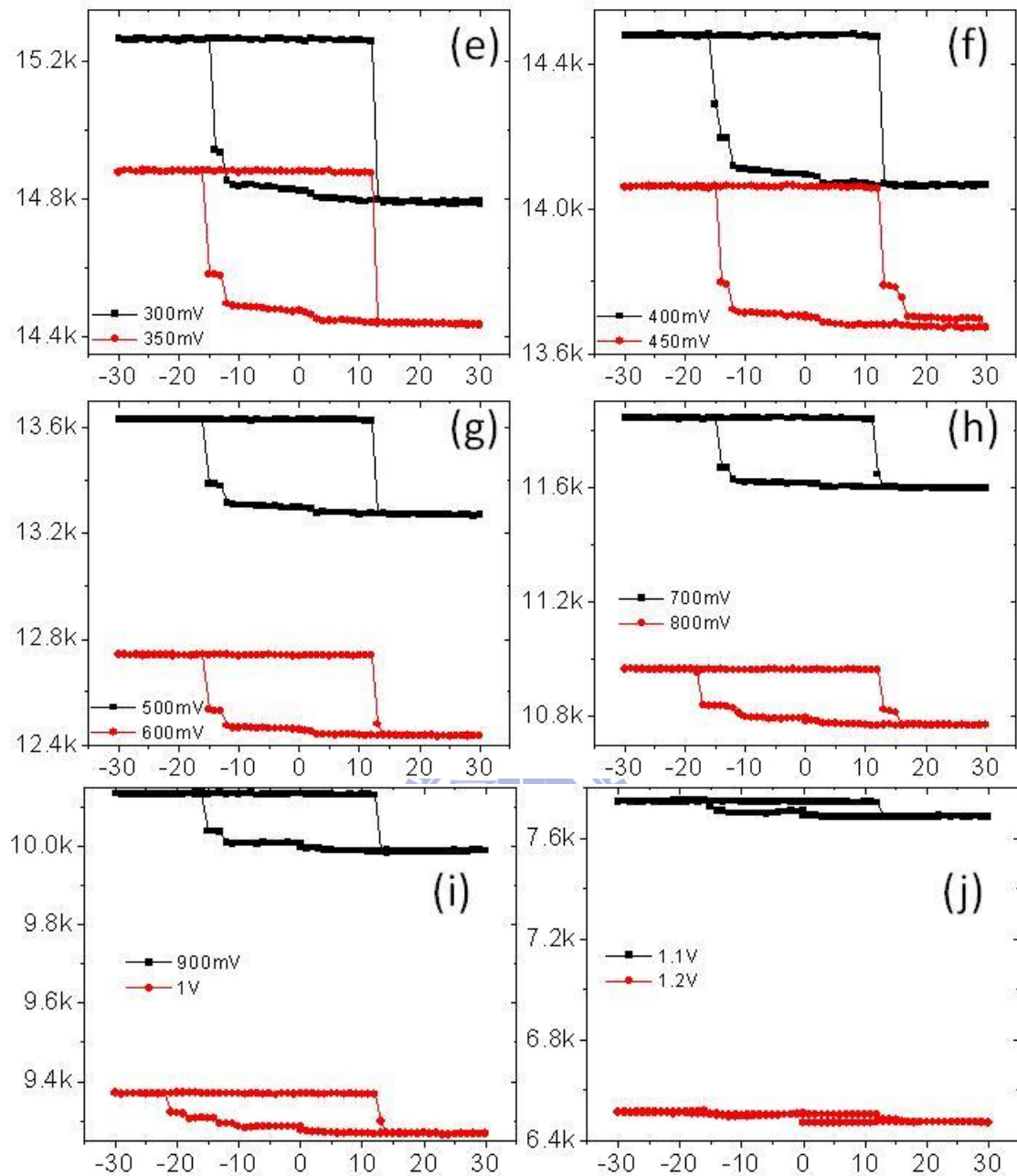


Figure 4.2-10 Series of bias-dependent MR loops. (e) ~ (j) for bias voltage of 300 mV ~ 1.2 V.

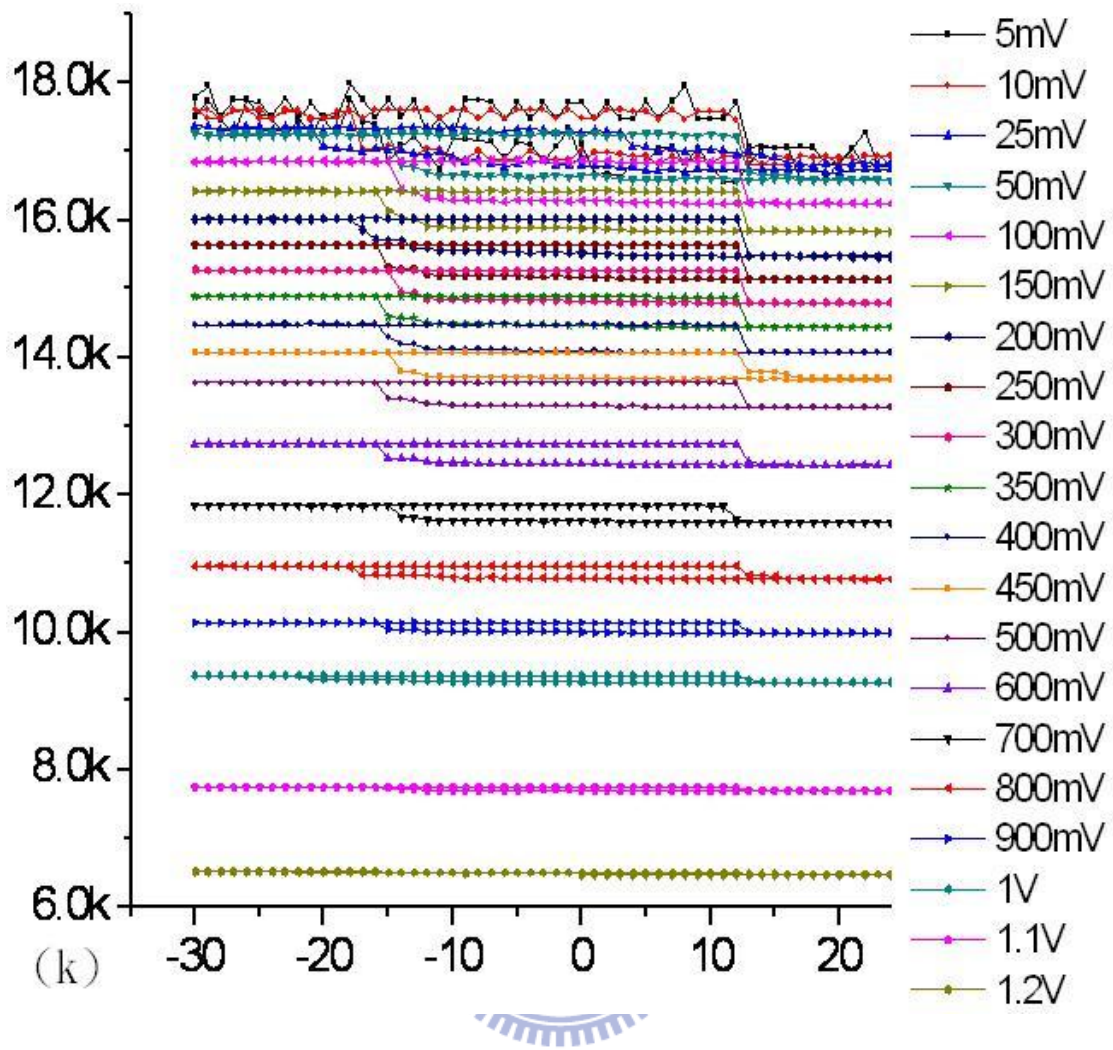


Figure 4.2-10 (k) full range.

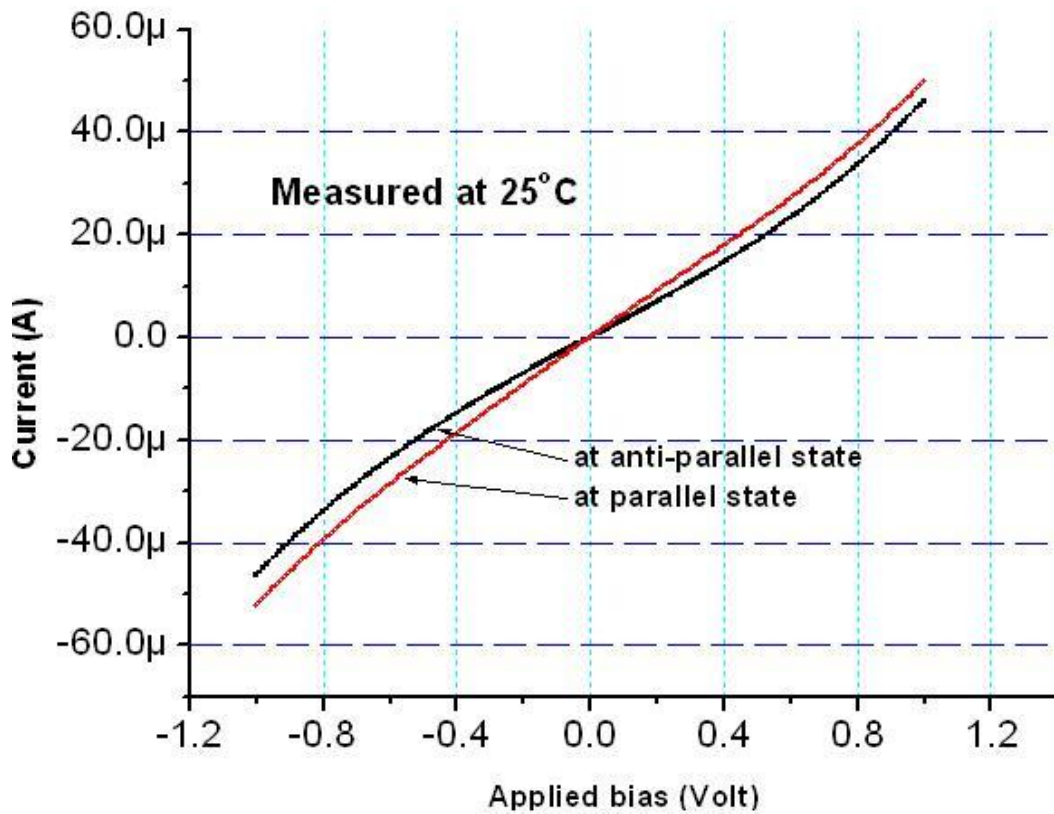


Figure 4.2-11 I-V curve for the MTJ device measured at 25°C.

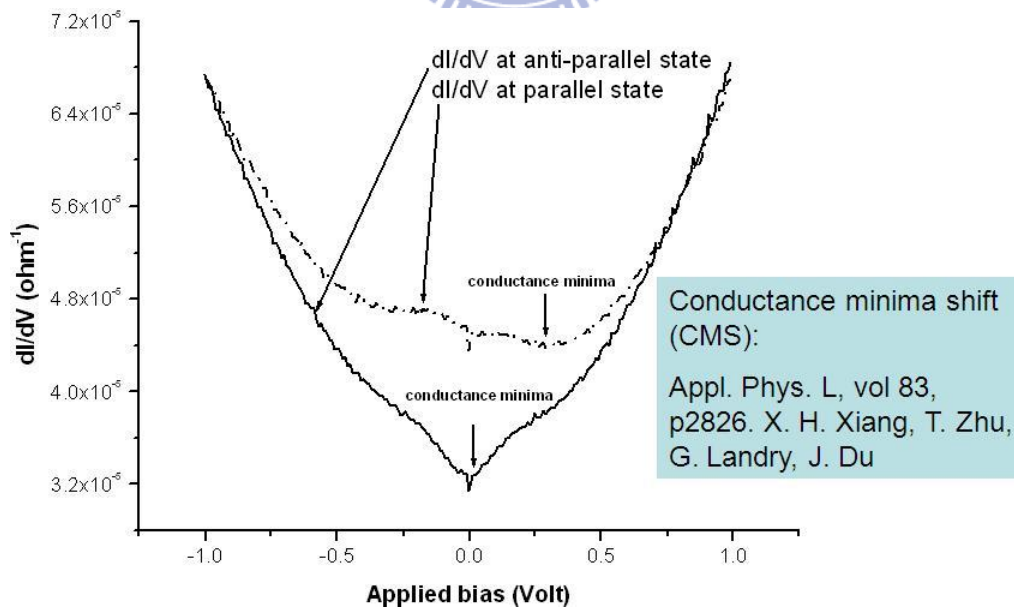


Figure 4.2-12 Dynamic conductance dI/dV . Derived from Figure 4.2-11 by differentiating I with V.

By extracting the resistance from Figure 4.2-11, the resistances for AP and P configurations are derived (Figure 4.2-13). Consequently, the asymmetry also exists in the bias dependence of resistance, and MR ratio, too. However, unlike the conductance or resistance dependence on bias, the highest value of MR ratio (Figure 4.2-14) is roughly at zero bias, although the MR-V curve for the full voltage range behaves slightly asymmetry. We then further measured a series of I-V curves with changing temperature (Figure 4.2-15), and the dynamic conductance, resistance, and MR ratio are also derived and shown in Figures 4.2-16, 4.2-17, and 4.2-18, respectively. The results indicate that the shapes of dI/dV -V and R-V curves remain unchanged with increasing temperature, but just shift towards higher (for conductance) and lower (for resistance). For MR%-V curve, however, the shape is sharper at low temperature than that at high temperature in the range from 25 ~ 140°C. In order to confirm the asymmetry of dynamic conductance, the polarities of applied bias were reversed, and the resulted dI/dV -V curves also reversed about zero bias (Figure 4.2-19). Finally, we depict an MR % (T,V) function by using the measured data to give an image describing the MR dependence on temperature and bias voltage (Figure 4.2-20).

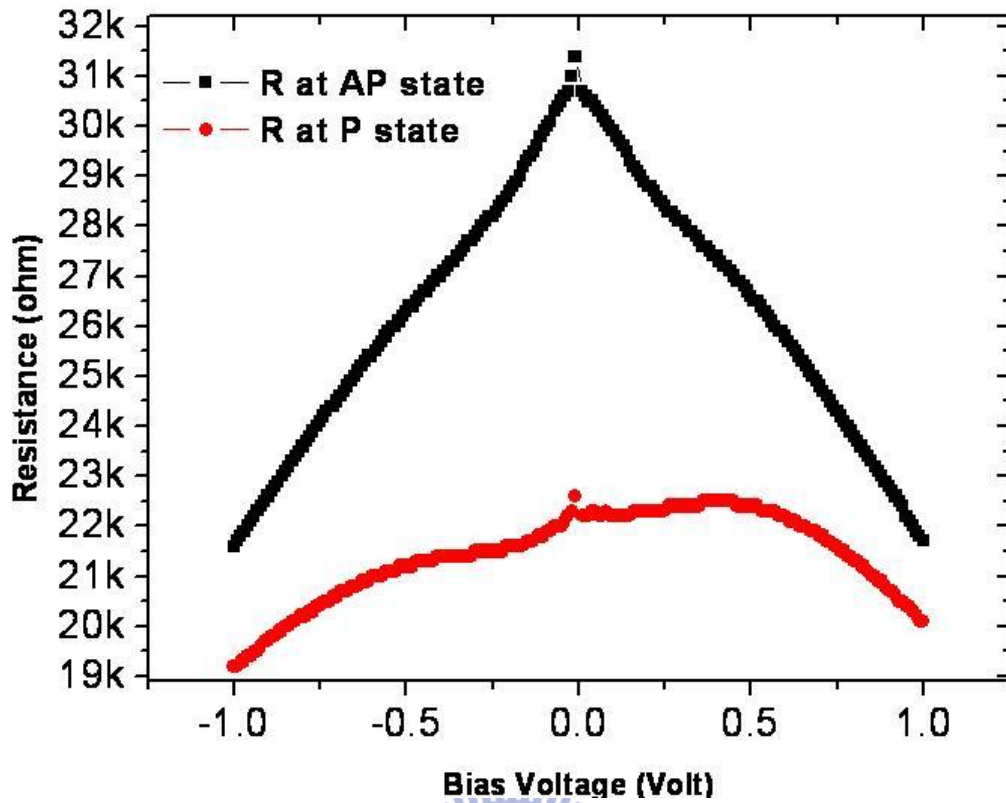


Figure 4.2-13 Bias dependence of resistance.

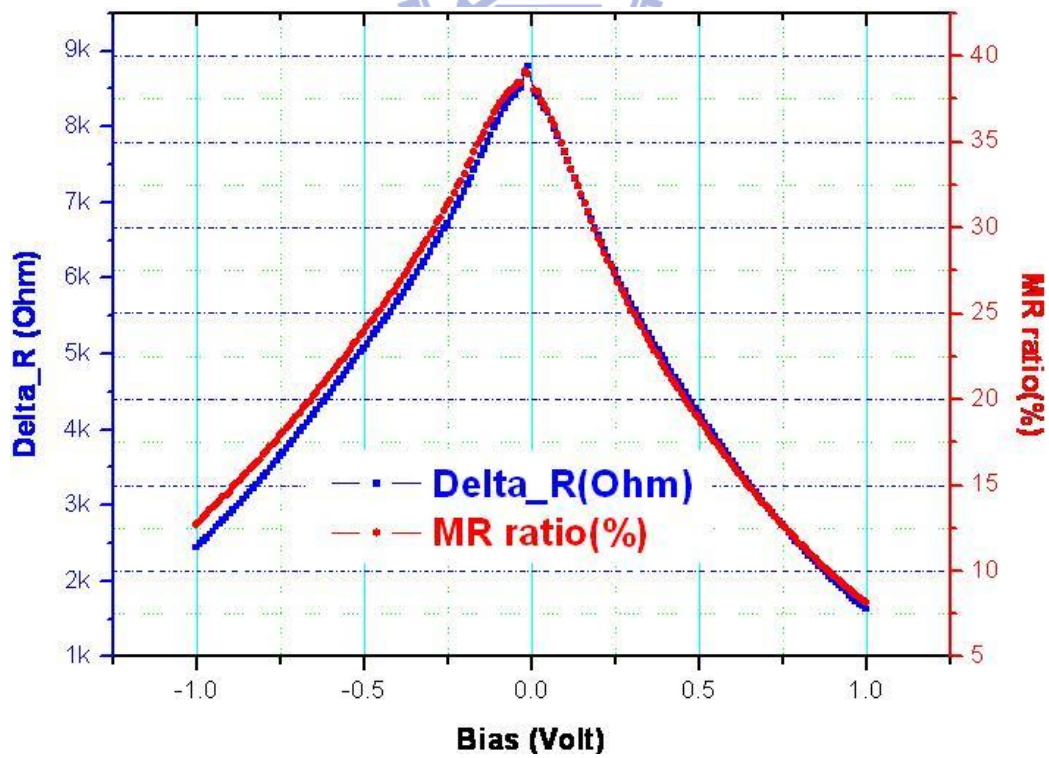


Figure 4.2-14 Bias dependence of ΔR and MR ratio. Derived from Figure 4.2-17.

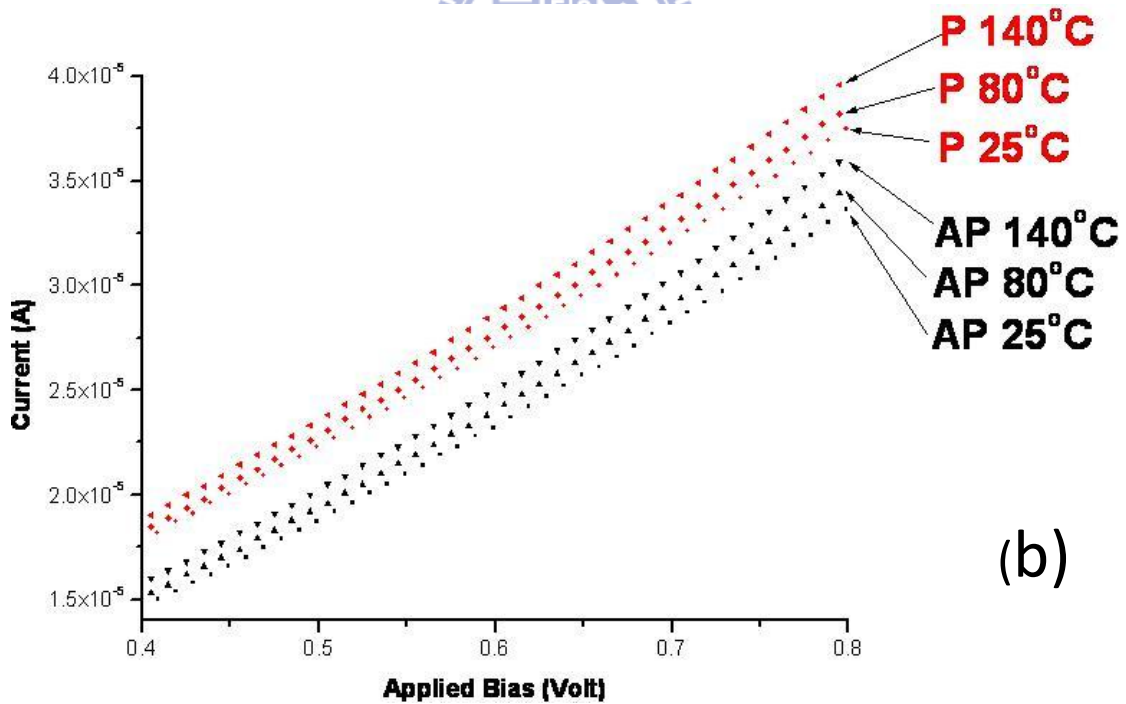
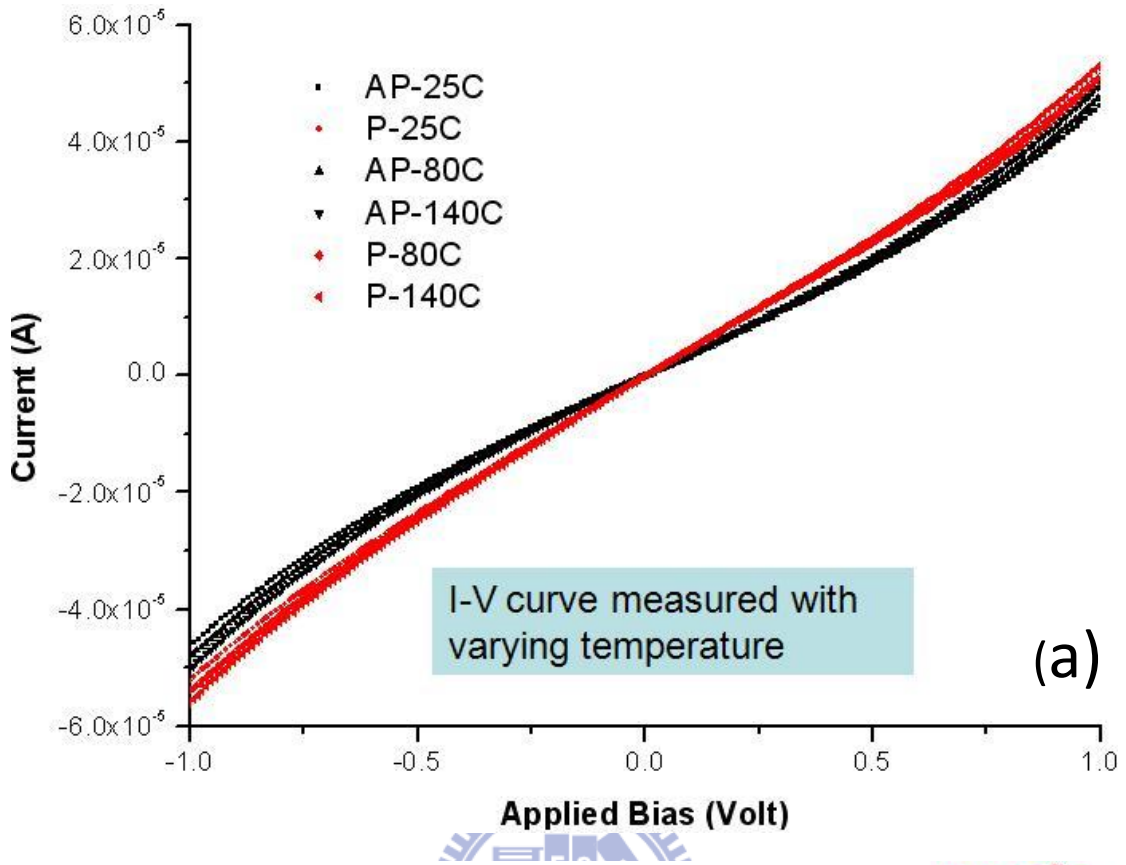


Figure 4.2-15 I-V curve dependence on temperature. (a) Full range (b) zoom in range from 0.4 V to 0.8 V.

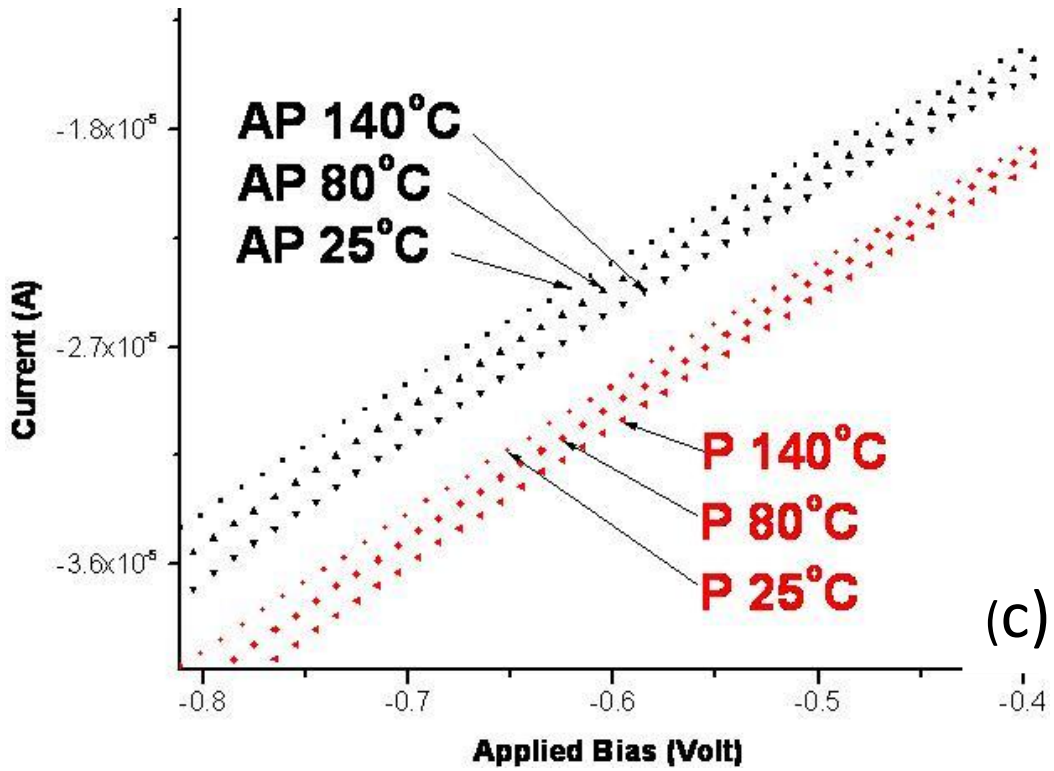


Figure 4.2-15 (c) zoom in range from -0.4 V to -0.8 V.

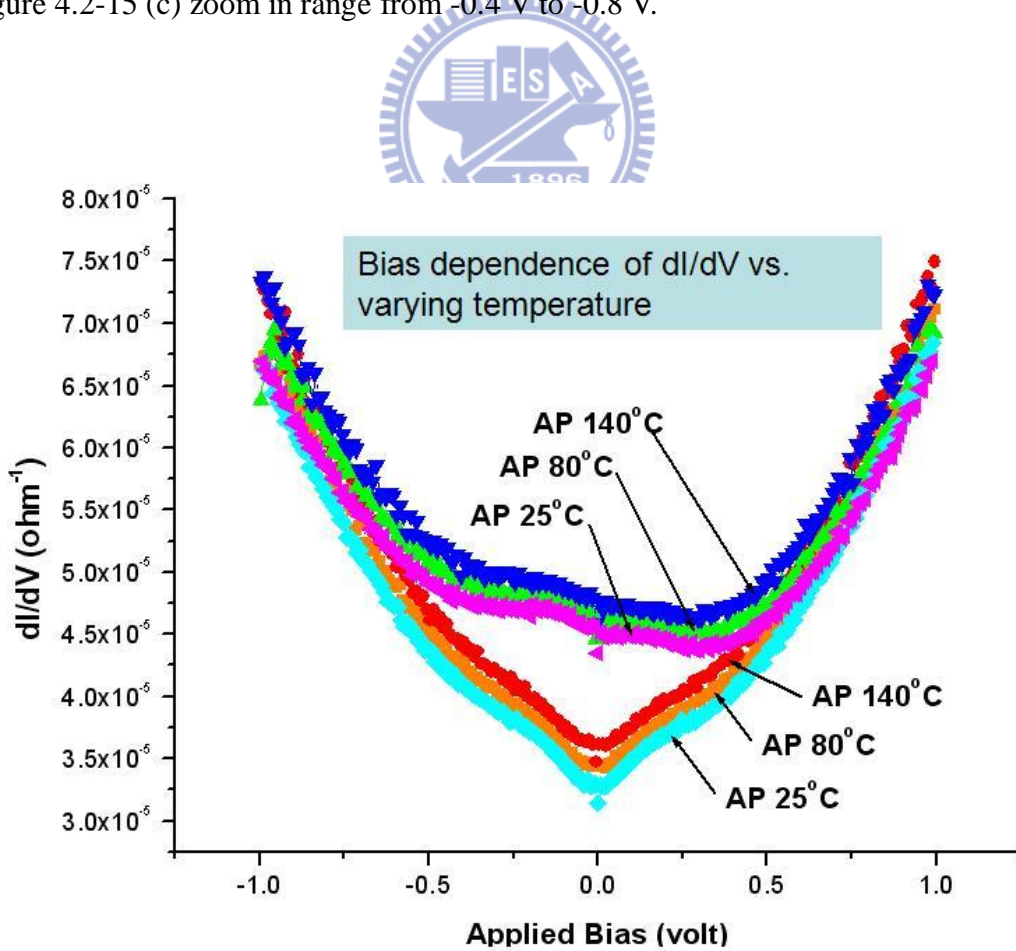


Figure 4.2-16 Temperature dependence of dynamic conductance.

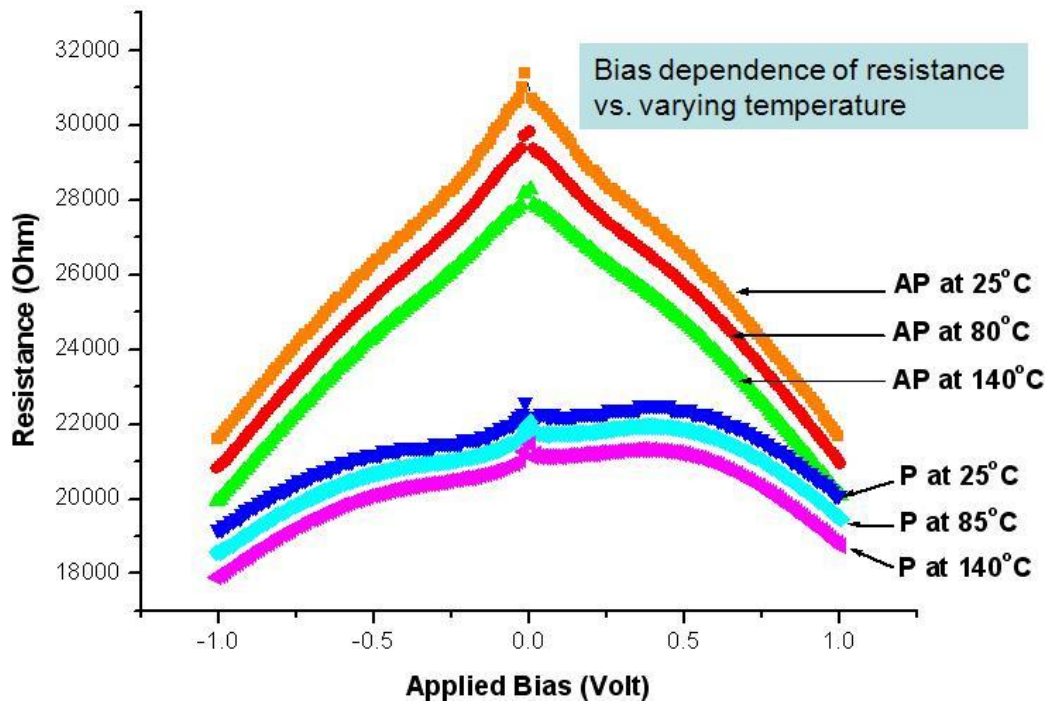


Figure 4.2-17 Temperature dependence of resistance.

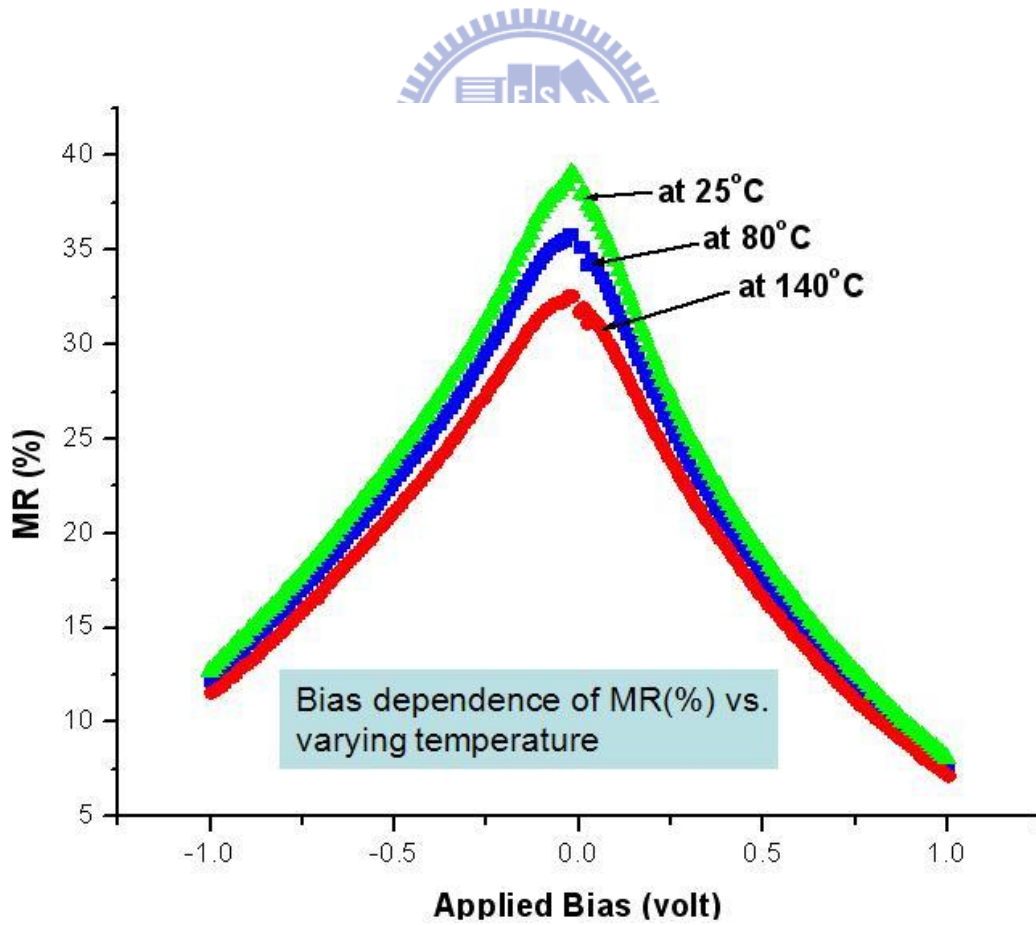


Figure 4.2-18 Temperature dependence of MR ratio.

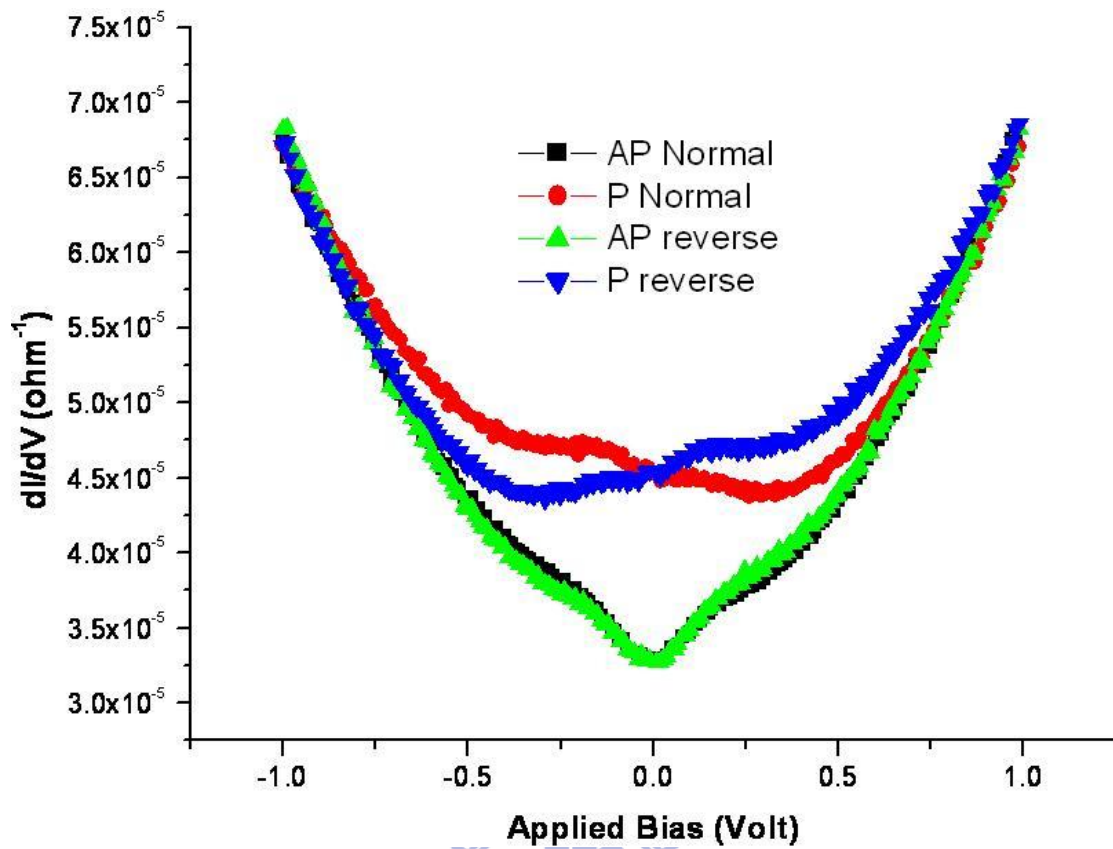


Figure 4.2-19 Comparison between positive and negative voltage polarities of dynamic conductance.



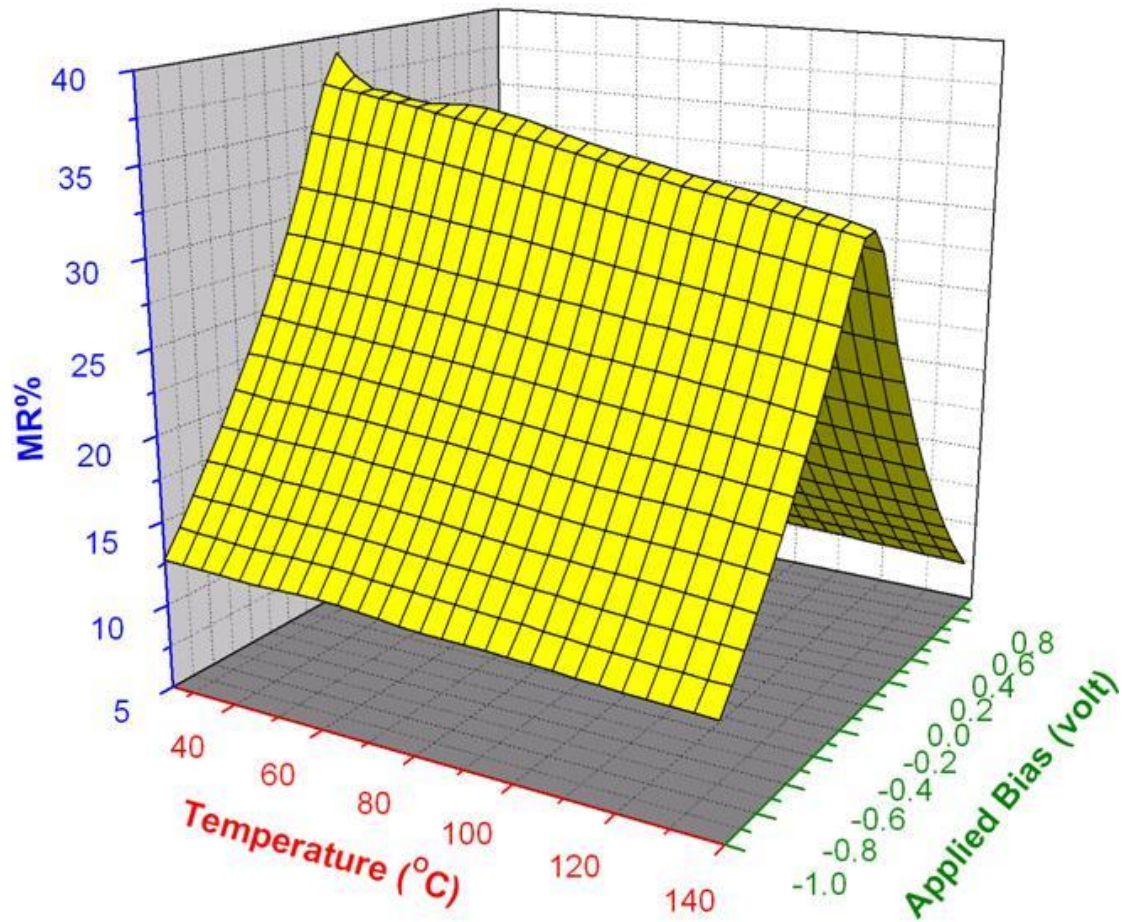


Figure 4.2-20 MR ratio dependence on temperature and bias voltage.

4.3 Magnetic reversal process and current-induced domain wall motion in ferromagnetic curve- and ring- shape structure

4.3.1 AMR behavior and current-induced domain wall motion of single-layered FM ring

We explored the AMR behavior of the single-layered Py ring (Figure 4.3-1) by introducing the current from I+ to I- and the sensing voltage between V+ and V- (labeled in the inset). Here I+ and V+ are in the same electrode. With this probing arrangement, the AMR signal would be more sensitive than that with only two terminals since the ratio of domain wall area to the region between the two voltage probes is larger, and hence such arrangement is especially useful for domain wall detection. The whole MR loop exhibits a typical AMR behavior of an FM ring as mentioned previously in Chapter 2.

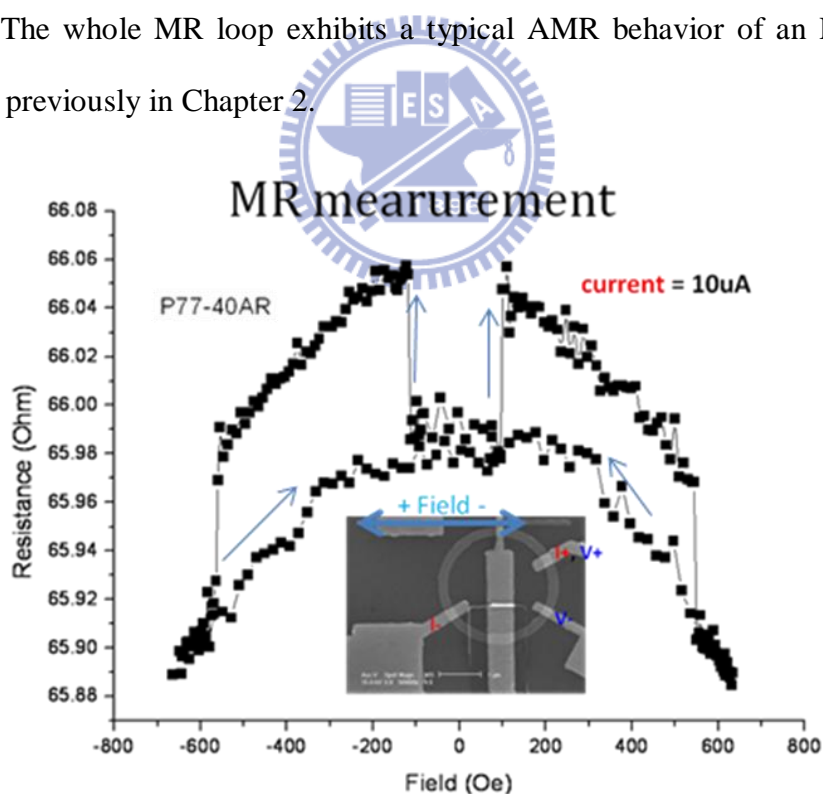


Figure 4.3-1 AMR measurement of a single-layered Py ring with thickness 40 nm and width 225 nm. The measuring current was $10\mu\text{ A}$ at room temperature. The inset is the SEM image of the sample and the direction of applied field is indicated by the double-head arrow.

The minor loop is shown in Figure 4.3-2. After switching from onion state to vortex state (around -120 Oe), the applied field was swept back to the zero field, and the resistance maintains in the same high level with the vortex state. Onion state is before -120 Oe. After magnetization transformed to vortex state, the vortex state exists ranging 0 ~ -400 Oe in the present result. Thus the vortex can be examined as a stable state after its formation. Actually, it is believed that vortex state can exist in +550 ~ -550 Oe according to the previous data (Figure 4.3-1).

MR measurement – minor loop

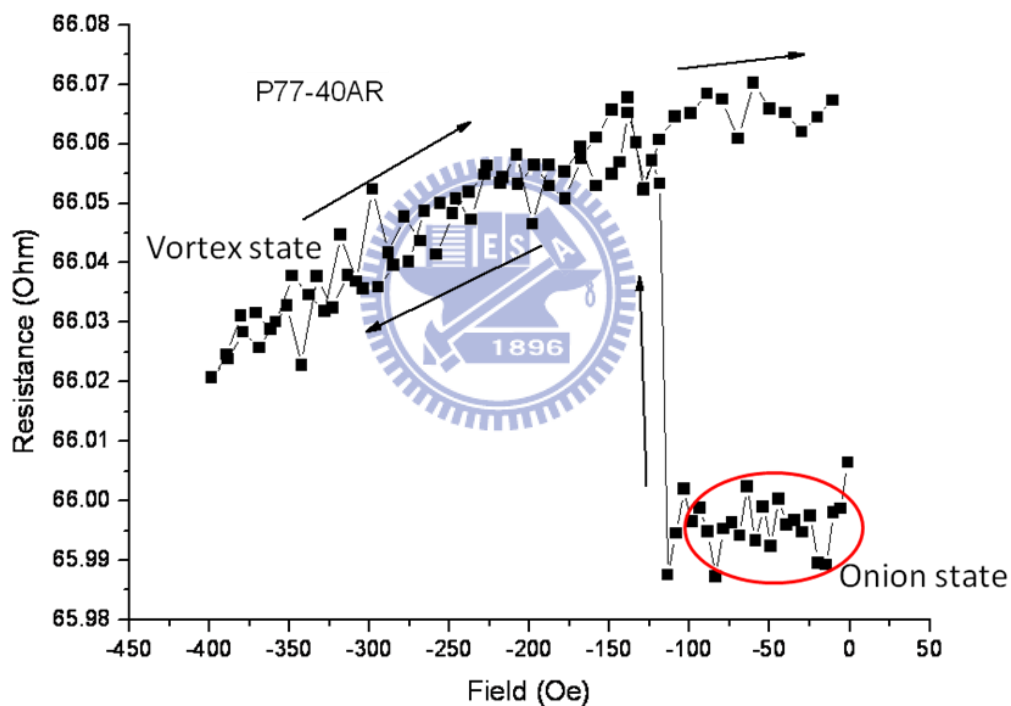


Figure 4.3-2 The AMR minor loop. The arrows indicate the direction of field sweeping.

We then observed the current-induced domain wall motion, by introducing a pulse current with duration time 5 ms in advance, which is considered far from the dynamic scale (less than tens of ns). The magnitude of pulse current is from 100 μ A to several mAs. Each pulse current was followed by a resistance record by applied a measuring

current of $10\mu\text{ A}$. Figure 4.3-3 shows the results of current-induced measurement dependent on the magnitude of pulse current. The state was initially from onion at a constant applied field, and then switched to vortex by pulse current. For each constant field, the pulse-current dependence of resistance was recorded. For the present case, the onion-to-vortex switching field is around -120 Oe . The critical current required to switch the state increase with the increasing difference between the held filed and the switching field. The results are shown in Figure 4.3-4. The critical current density J_c is of the order 10^7 A/cm^2 which is in agreeemt with the typical results [80-85].

Current-driven measurement

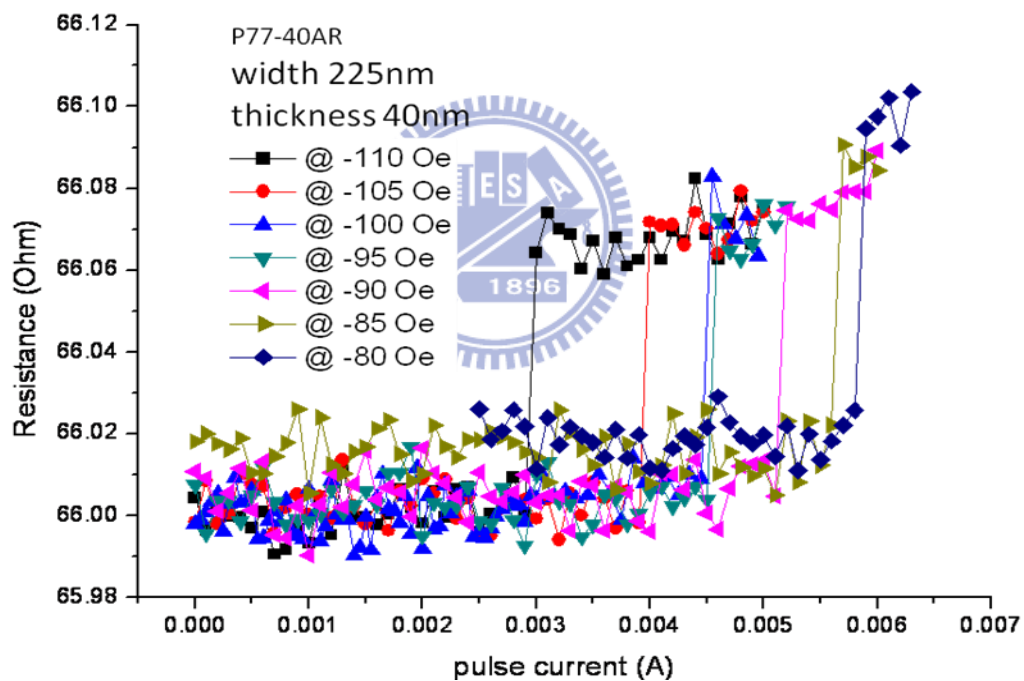


Figure 4.3-3 Field-dependent current-induced domain wall motion measurement.

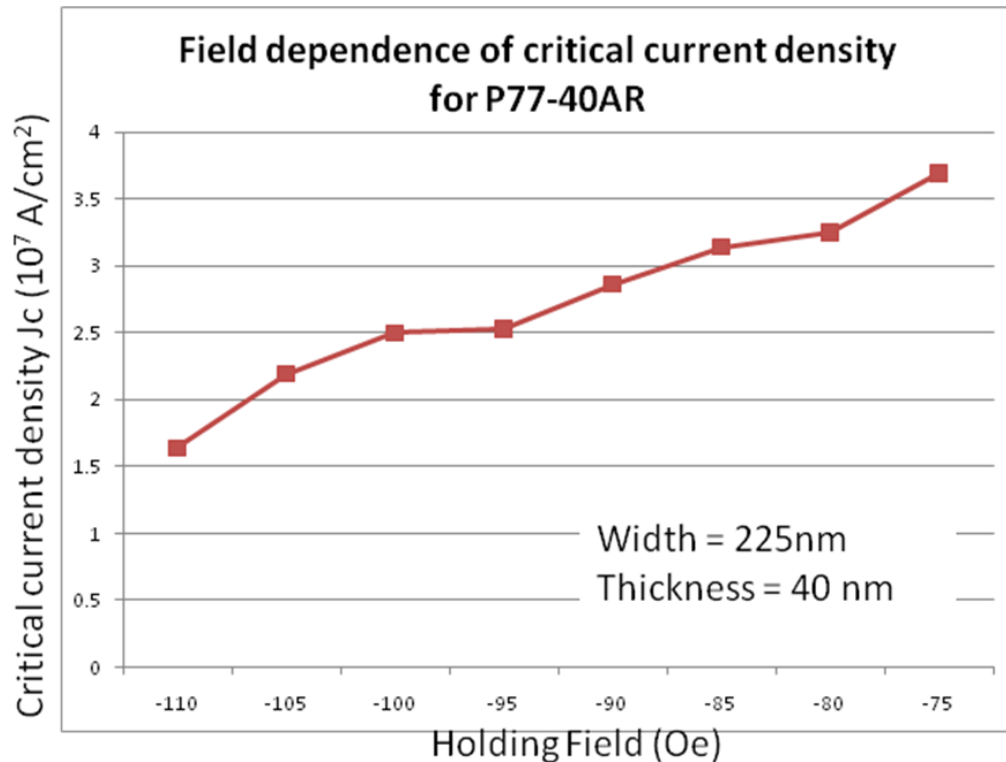
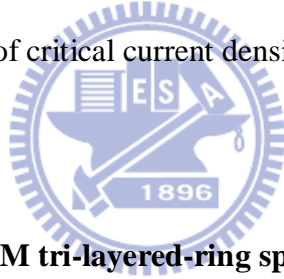


Figure 4.3-4 Field dependence of critical current density J_c .



4.3.2 MR behavior in FM/N/FM tri-layered-ring spin valve

The MR measurement of a tri-layered spin valve in ring shape with structure Py(10nm)/Cu(9nm)/Py(20nm) is shown Figure 4.3-5. The width is 200 nm and diameter is 3 μ m. The applied field transverses to the current contacts (I+ and I-). The full MR loop (inset in Figure 4.3-5(a)) exhibits a roughly symmetry in macroscopic scale.

The main panel shows a zoom in part (-100 ~ +200 Oe) of half loop from negative field to the positive. The resistance gradually increase from the larger magnitude of field to the smaller one (before zero) without a drastic change. This behavior can be reasonably understood with the AMR effect, since both Py layers are from saturation gradually to the onion state and maintain parallel configuration. We define this region as configuration **1** (labeled in Figure 4.3-5). For the present case, the resistance

increases drastically at the field magnitude near zero and reaches the highest at the field near 32 Oe. The resistance changed immediately till 147 Oe. We label this highest level as configuration **2**.

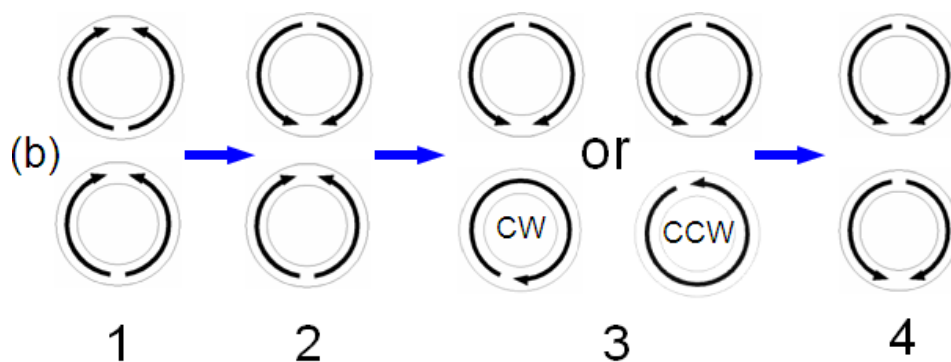
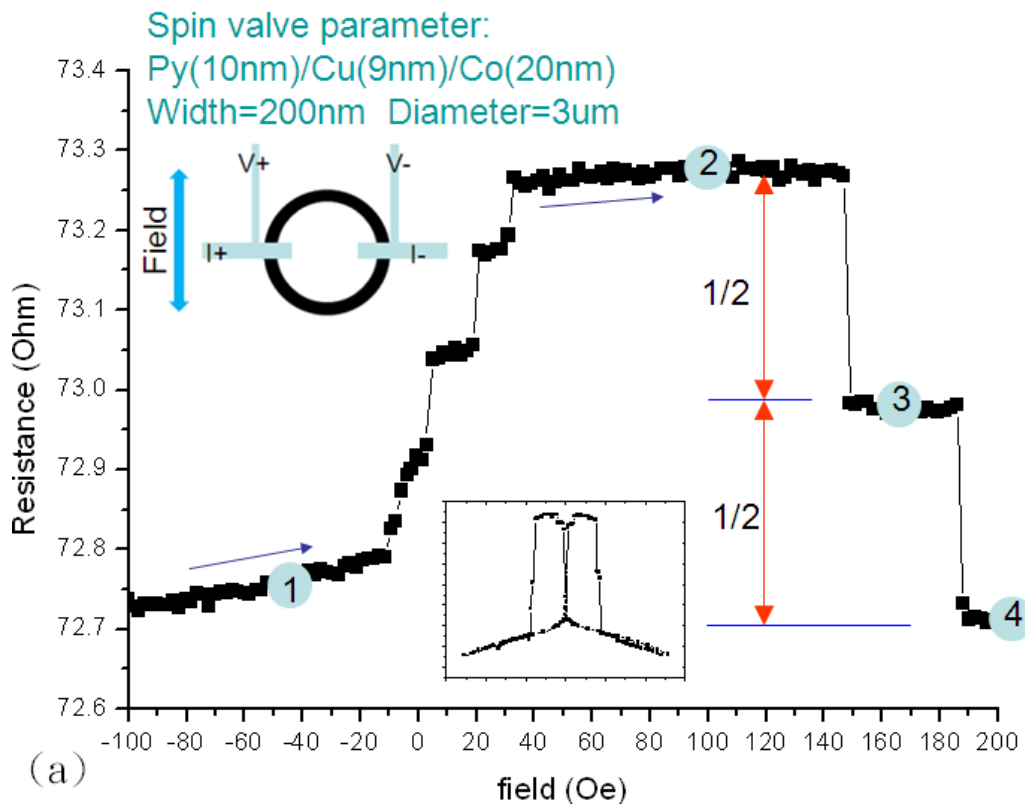


Figure 4.3-5 (a) MR measurement of Py/Cu/Py tri-layered-ring Spin valve. The inset is the full loop. Each circle labeled with number represents a magnetic configuration (or state) which is shown in (b). The single-head arrows indicate the sweep direction. (b) Illustration of each magnetic configuration. The numbers correspond to the labeled circles in (a). The upper ring represents the Py-10nm layer (soft layer), and the bottom one the Py-20nm (hard layer).

With field exceeding 150 Oe, the resistance drastically drops to configuration **3**, and then decrease again at 188 Oe. After 190 Oe (configuration **4**), the resistance shows a gradual decline with field magnitude increasing and without drastic change. The configuration **4** is in the same magnetic process with the configuration **1** that can be explained by AMR, but in the opposite direction. The alignments of the spin valve are also the same (parallel) for configurations **1** and **4**, but opposite to each other. By evaluating the resistance differences among configurations **2**, **3**, and **4**, we found the resistance value of configuration **3** is roughly half the total resistance change between configurations **2** and **4**. Since the MR behavior within this range is dominated by CIP GMR, the highest level, configuration **2**, is consequently recognized as anti-parallel (AP) alignment. According to the results from Nam et al. [100, 103], we considered the magnetic state as reverse onion for the 10nm-Py layer, and forward onion for the 20nm-Py layer. Another possible configuration could be the two opposite vortices (CW-CCW and CCW-CW) for the two Py layers. In the major loop sequence, however, the two opposite vortices cannot be formed, hence the configuration **2** is most likely the two opposite onion states in the two Py layers. The configuration **3** is then determined as reverse onion for the 10nm-Py layer, and vortex for the 20nm-Py one, since both P and AP alignments occupy half of the area of the whole spin valve. However in present measurement, there is no crucial information to determine the chirality of the vortex and hence the 20nm-Py layer could be either in CW or CCW as shown in Figure 4.3-5(b).

As to the region between configurations **1** and **2**, there exists some metastable states that occur occasionally during the major loop processes and are difficult to be confirmed as certain states. Among these states, an intermediate state similar to configuration **3** can roughly be identified. It is recognized as a configuration in which the 10nm-Py ring is in vortex state and the 20nm-Py one the forward onion state as

shown in Figure 4.3-6.

This intermediate configuration (or state) was observed by Nam et al. [100, 103] and considered as a certain state existing in the major loop sequence. The size effect is most suitable to explain the occurrence of this unstable intermediate state. According to the phase diagram of the magnetic switching of ferromagnetic rings [93], a small aspect ratio of the diameter (or radius) to the width of a ferromagnetic ring favors the existence of the vortex state. As to the perpendicular size, large thickness also tends to form the vortex state. In a ring-shaped spin valve, the dipole interaction between the two FM layers favors the AP configuration in which the two FM layers are in the two opposite onion states to each other at low field.

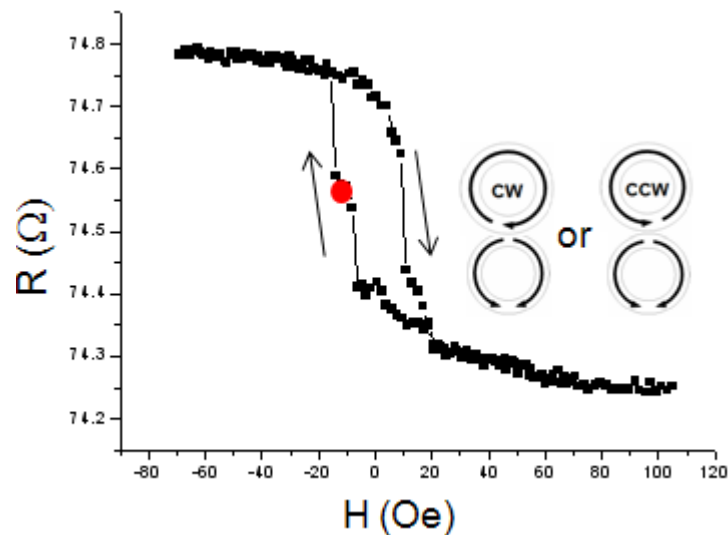


Figure 4.3-6 Minor loop of the measurement of Py/Cu/Py tri-layered-ring spin valve initially saturated in positive field. The arrows indicate the field sweep directions. The circle represents the intermediate state illustrated in the inset. The upper ring represents the Py-10nm layer (soft layer), and the bottom one the Py-20nm (hard layer).

Now we compare the size parameters in the present work with that of ref. [100, 103]. The aspect ratio of diameter/width in the present work is 15, and that in ref. [100, 103] is 13.5, which has more stability of the vortex formation than our sample.

Furthermore, the thicker FM ring film produces stronger stray field at both domain walls in the onion state, and then causes stronger dipole interaction between the two FM layers in a ring spin valve. The thicknesses of FM layers are 4 nm for Py, and 5 nm for Co in refs. [100, 103], whose dipole interaction is relative low to the present device (10 nm, and 20 nm for Py). Therefore, the unstable intermediate state, which occasionally exists between the configurations **1** and **2** in the present work, can be attributed to the critical size between the formations of vortex and onion of the softer FM layer in a ring spin valve. As the configuration **3**, soft ring in reverse onion and hard ring in vortex, has been observed and identified [96-100, 103] firmly existing during the major loop. This is also the consequence of size effect since the thicker ring film prefers the formation of vortex.

The minor loop (shown in Figure 4.3-6), starting at the AP configuration (**2**) about -75 Oe then back to the initial saturated direction (positive field), shows no intermediate state. Instead, it directly switches from AP to P configuration at about 10 Oe.

4.4 Determining vortex chirality in ferromagnetic ring by lateral spin valve

4.4.1 Structure of ring-wire lateral spin valve

We used the ring-wire lateral spin valve structure to measure and detect vortex chirality in the ferromagnetic ring. In this structure, a Py ring, a Py narrow wire, and Cu contacts were used as spin injector, detector, and the normal-metal spin diffusive channel, respectively. E-beam lithography and lift-off technique were used to fabricate the structure. The ring and the narrow wire with an empty space separating them were first deposited on SiO₂ / Si substrate by using dc magnetron sputtering in which the base pressure and the working pressure were 5×10^{-7} and 1.1×10^{-3} Torr, respectively. Before depositing Cu contacts, the Py surface was well cleaned by means of ion milling at a discharge bias of 3 kV for 3.5 min and at the working pressure of 1×10^{-5} Torr. Then, without breaking the vacuum, the Cu contacts were fabricated to connect the ring and the wire to the pad leads by means of the same fabrication process used for patterning Py ring and wire films. The MR measurement was performed by introducing either DC or AC current source. The DC and AC source equipments we used were mentioned in Chapter 3. A sweeping magnetic field was applied parallel to longitudinal direction of the Py wire to alter the magnetizations of the ring and the wire during MR measuring. The SEM image of a ring-wire lateral spin valve is shown in Figure 4.4-1.

In sections 4.4.2 and 4.4.3, we will discuss the results from the same one lateral spin valve device, and nonlocal measurements were used to detect vortex chirality, i.e., nonlocal spin valve (NLSV) measurement. The size information of the spin valve structure in present discussion are as follow: thickness of Cu and Py is 60 nm and 30 nm, respectively. Width of Py wire is 100 nm, Py ring 300 nm, and Cu diffusive channel 100 nm. Lateral space between the ring and wire is 350 nm. The

measurement parameter is AC current 0.5 mA at 44K with sampling step of 30e.

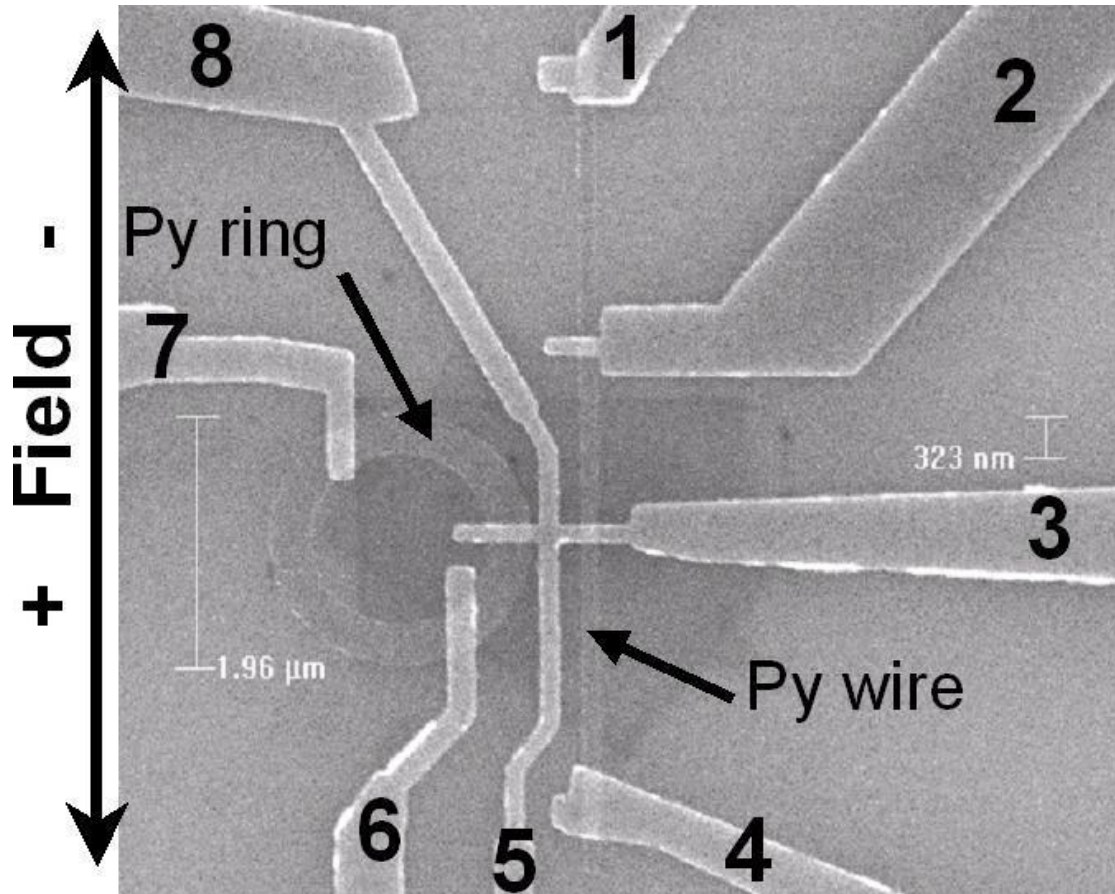


Figure 4.4-1 SEM image of the lateral spin-valve structure. The pre-malloy (Py) ring and the Py narrow wire are indicated by the arrows. Cu contacts are labeled as 1 through 8. The double-headed arrow on the left side defines the direction of applied field.

4.4.2 AMR measurement of the individual ring

To compare with NLSV signals, the AMR of the individual Py ring was also measured by employing Cu contacts 7 and 5 as voltage probes and contacts 6 and 8 as current probes. Here the arrangement of current probes and the amplitude of the current were respectively set identical to that in NLSV measurement. Therefore, the reversal processes of the Py ring at the two different measurements (NLSV and AMR) would not be obviously varied due to possible current induced effect. The AMR loop for the ring is shown in Figure 4.4-2(a). Since the current flows along the perimeter of the ring, the MR would be at the highest resistance while all magnetic moments are aligned to the perimeter direction (current parallel to moment), and at lower resistance while some or even most of the moments are out of the perimeter direction. Furthermore, the vector components of magnetic moments with higher magnitude are aligned along the direction of stronger applied field (near saturation). At the weaker field, however, components with higher magnitude are aligned to the perimeter direction of the ring (onion state or vortex state) since the field is no longer strong enough to overcome the shape anisotropic field of the ring. Hence, the AMR behavior of the ring reveals that the resistance is relatively low at stronger field and high at weaker one. However, the detailed reversal process behaves in a more complicate manner during the switching of magnetization states. At the field $-50 \sim -80$ Oe, a dramatically decrease and the subsequent increase in resistance separately appear due to the expansion and annihilation of the two walls in onion state (state **1** in Figures 4.4-2(a) and (b)). After completing the annihilation of the two walls, the magnetization reversal process goes into vortex state (state **2**) in which all of the moments are parallel along the perimeter direction of the ring, and the resistance increases to higher than that at onion state. With the field exceeding -300 Oe, the vortex state changes into reverse onion state (state **3**). Hence, the MR shows an abrupt

drop at -300 Oe and decrease with field increasing toward negative direction. At vortex state, however, CW and CCW vortices occupy the common resistance level. Therefore, the AMR loop of the individual ring provides no crucial information to distinguish the chiralities of the vortex state. The AMR loop of the ring in the present study reveals a tendency in accord with that in the ref. [101].

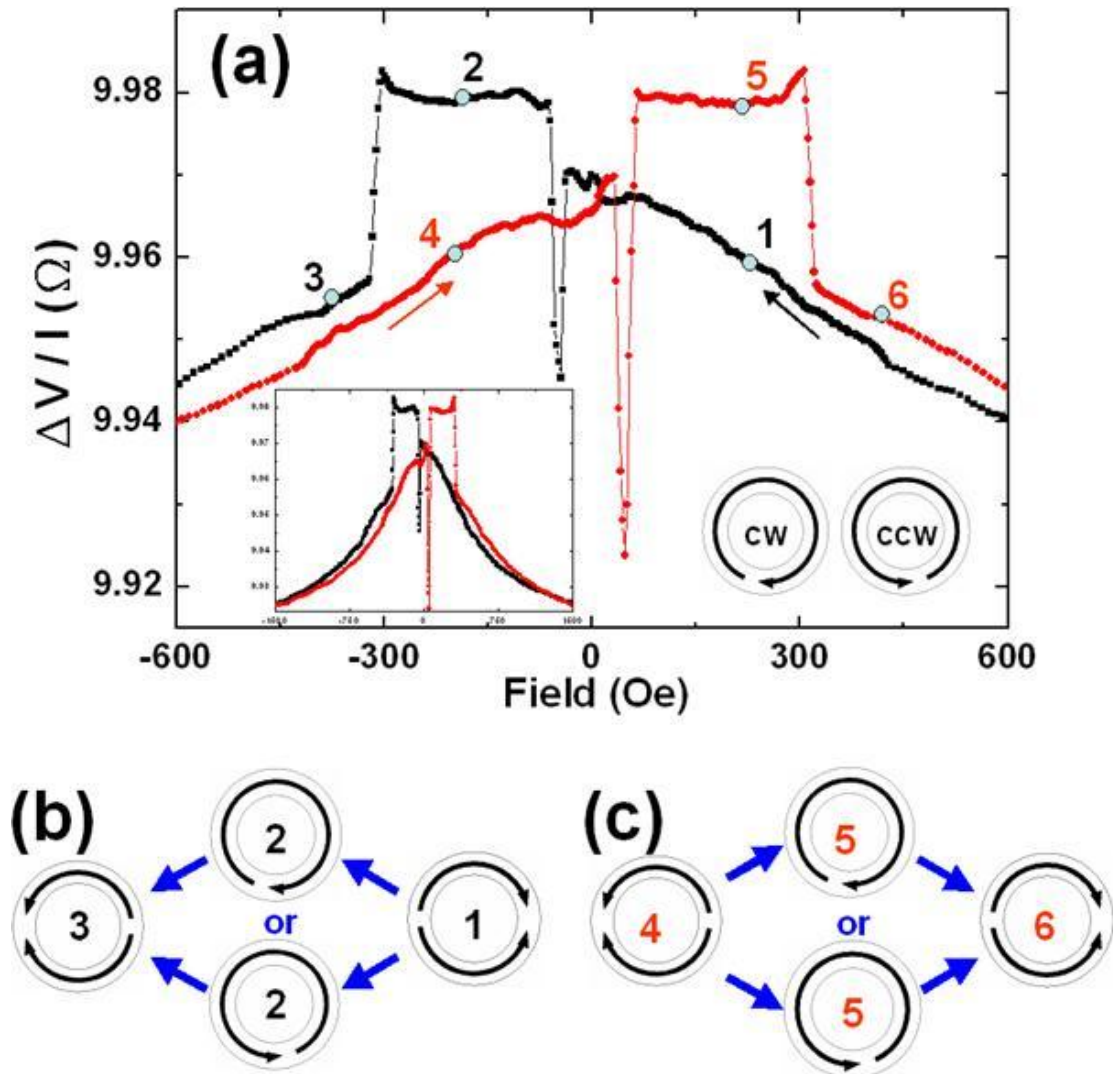


Figure 4.4-2 (a) The AMR loop of the ring. The arrows indicate the direction of the proceeding process on the loop. The left inset shows the full range of field -1500 ~ +1500 Oe. Vortex directions are schematically indicated in the right inset. Each number with its solid circle is employed to represent each magnetization state and the sequence in process, which is also shown in schematic diagram (b) and (c), in which, the magnetization reversal process is schematically represented.

4.4.3 NLSV measurement and comparison with AMR result

To perform NLSV measurement, current probes were set at 6 and 8, and voltage probes at 5 and 2. An NLSV MR full loop (field exceeding the switching field of the Py wire) is shown in Figure 4.4-3(a) (top curve). It reveals a clear spin-valve signal without other AMR effect. Starting with the sweeping from the positive field to negative one (forward sweep), the resistance is at low level during the process from the onion state (spin-valve configuration **1** in Figures 4.4-3(a) and (b)) to -300 Oe. Here the field -300 Oe is in accord with that in the previous AMR loop of the individual ring. This indicates the magnetizations of the narrow wire and the region near the Cu/ring interface is maintained at parallel configuration till the switching for vortex state to reverse onion state. Hence, the vortex state (configuration **2**) would be CW direction. After the vortex state switches at -300 Oe into the reverse onion state, the configuration of the spin-valve magnetizations switches to anti-parallel state and results in an increase in resistance with a clear step at -300 Oe. The high resistance level remains till -510 Oe (configuration **3**). After -510 Oe, the magnetization of the narrow wire switches to the opposite direction, and spin-valve configuration switches to parallel state (configuration **4**). The resistance consequently changes back to the originally low level, hence a plateau from -300 to -510 Oe forms in the NLSV loop. At the reverse sweep (from negative to positive field), however, the NLSV signal shows asymmetric with the former. Since the plateau (high resistance level) is from 80Oe (correspondent with that in the ring AMR) to 510 Oe, the spin-valve configuration would be AP during the vortex state. Consequently, the vortex state must be in CW (configuration **6** in Figures 4.4-3(a) and (c)) so that the magnetization near the Cu/ring interface would be anti-parallel to the narrow wire. Furthermore, the reverse onion state still keeps the spin valve in AP configuration (configuration **7**). Hence, the resistance remains at high level till the switching of the Py wire at 510 Oe.

The measurement of minor loop was also performed to confirm the MR behavior of NLSV as shown in Figure 4.4-3 (a) (middle and bottom curves). The result shows the same switching fields and the same vortex chiralities with that of the full loop (up curve).

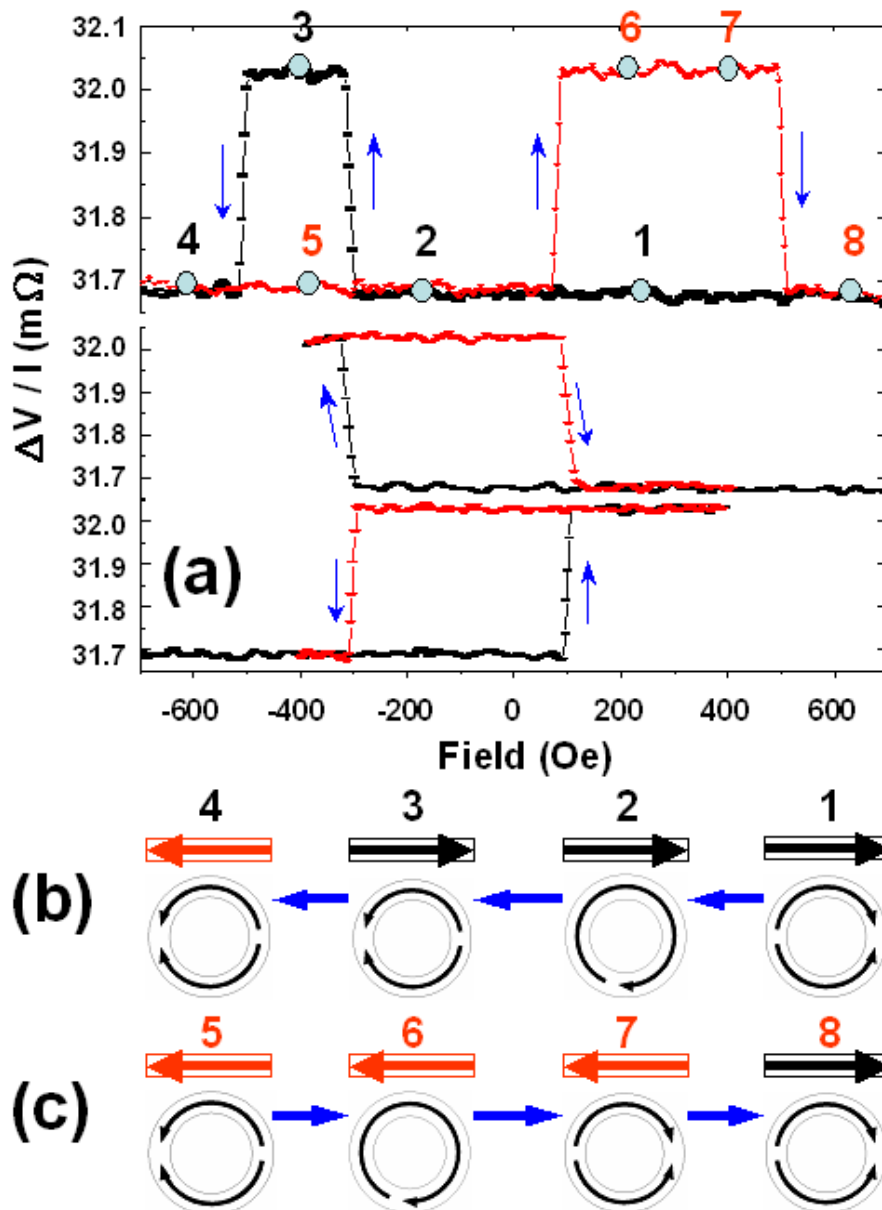


Figure 4.4-3 (a) The full MR loop of the NLSV device (top curve) and the minor loops (middle and bottom curves). The arrows indicate the direction of the proceeding process on the loops. The numbers (correspondent with that in (b) and (c)) represent the sequence in reversal process and the magnetic configurations of the NLSV. (b) Magnetic configurations in the reversal process from positive field to negative. (c) The same as (b) but in reverse sweep.

The other kind of NLSV loops for the present probe arrangement shows different behavior of reversal process (Figure 4.4-4). The two plateaus form at the regions $-150 \sim -510$ Oe and $300 \sim 510$ Oe in the forward sweep and reverse sweep, respectively. It is inferred that the vortex states are both CCW for both sweep processes. Furthermore, the switching field for onion state to vortex state changes to -150 Oe in the forward sweep. For present probe arrangement, full loop was repeated for five times, and minor loop (applied field lower than switching field of the Py wire) also five times for each of the two directions at which the magnetization of Py wire were held. The result of the ten minor loops (twenty sweeps) indicates that the chiralities are all CW regardless of the sweeping direction (forward or backward sweep) and the direction at which the magnetization of Py wire was held. For the five full loops, three of them are CW-CW loop (CW in forward sweep and CW in backward sweep) as shown in Figure 4.4-3(a) (up curve), and the other two are CCW-CCW loop (CCW in both forward and backward sweeps) as shown in Figure 4.4-4. Another NLSV measurement was also performed with replacing current probe 6 by 7 and maintain the others unchanged. The number of NLSV loops repeated is identical to that in the previous probe arrangement.

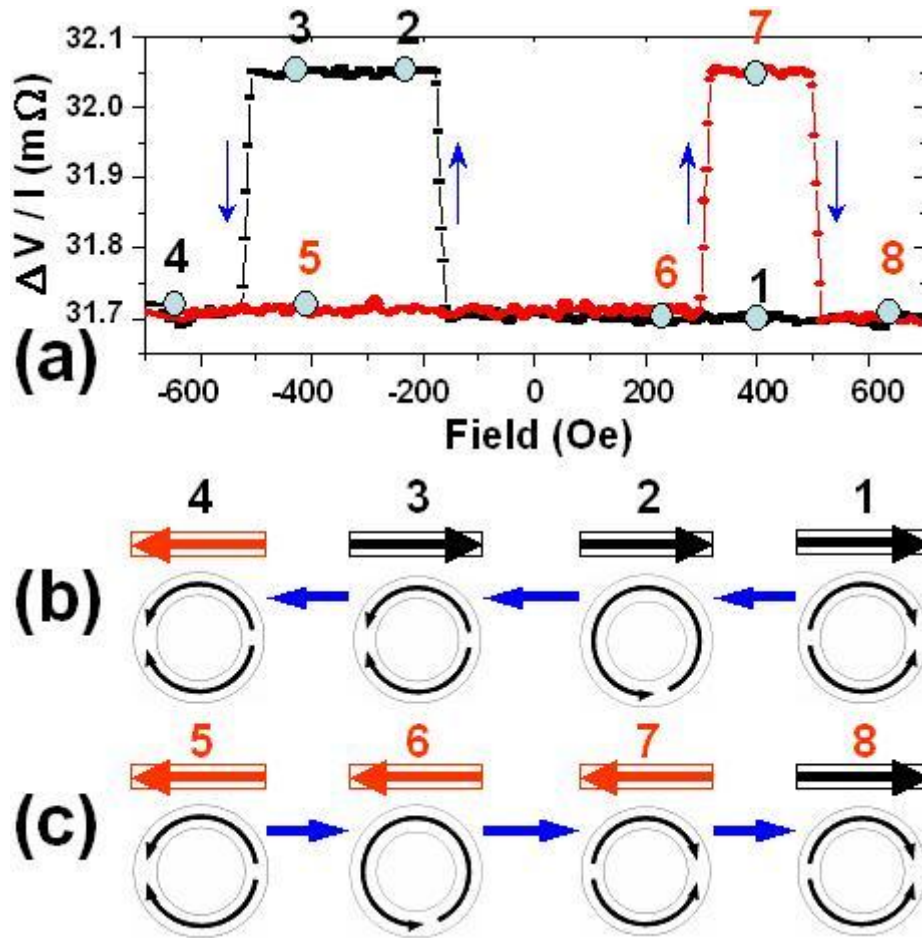


Figure 4.4-4 Another NLSV loop for the same probe arrangement as in Fig. 3. The depiction for the numbers and arrows are the same as in Figure 4.4-3.

Within the five full loops, four loops exhibit CCW-CW loop shown in Figure 4.4-5(a), and the other one behaves CCW-CCW loop in Figure 4.4-5(b). For the four CCW-CW loops, both plateaus are 150 ~ 510 Oe in absolute value. This means the switching field for onion state to vortex state is 150 Oe different from that (80 Oe) in the previous probe arrangement. In the CCW-CCW loop, the plateaus are -150 ~ -510 and 315 ~ 510 Oe for forward and backward sweeps, respectively. Hence, the switching field for vortex state to reverse onion state is about 315 Oe higher than that in the previous probe arrangement. According to the results from the minor loop measurement, ten loops are all CCW-CW regardless of the sweeping direction and the direction at which the magnetization of Py wire was held. Table 4.4-1 lists the

statistics of the distribution of the vortex chiralities.

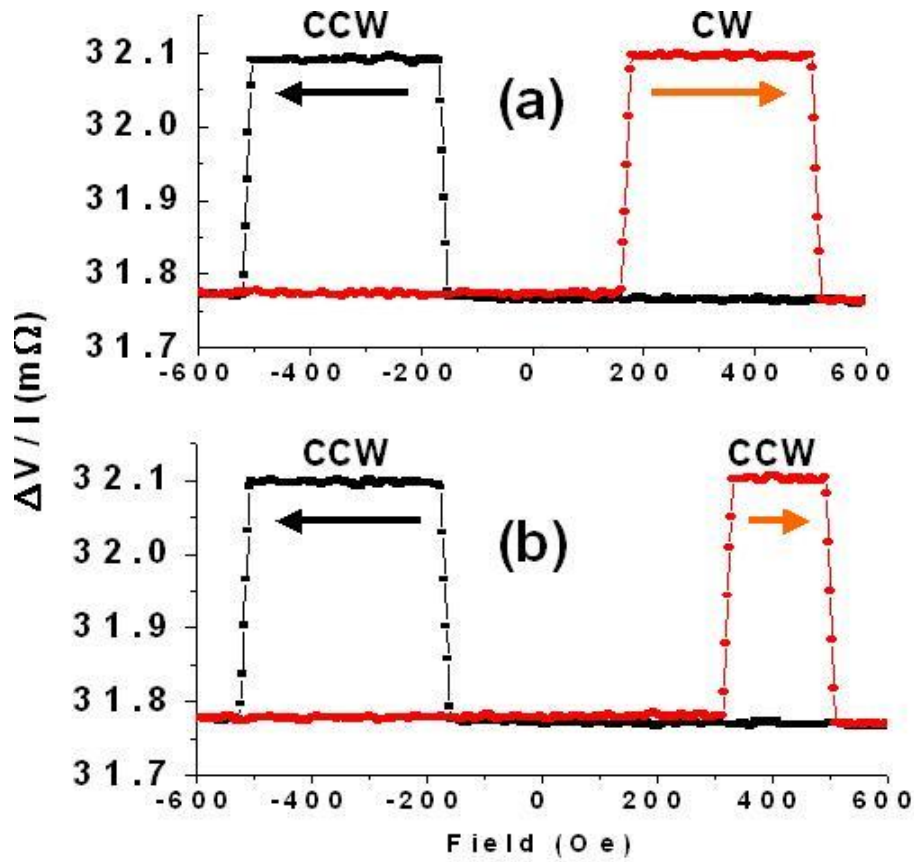


Figure 4.4-5 The NLSV loops for the probe arrangement in which the current probes were set as 7 and 8. The depictions for the arrows are the same with that in Figure 4.4-3 and Figure 4.4-4. (a) The CCW-CW loop: CCW in sweep from positive to negative field (forward sweep); and CW in the opposite (backward) sweep (b) The CCW-CCW loop: CCW in both forward and backward sweeps.

Here we briefly summary the observed results. In the same one probe arrangement, the switching fields of the onion-to-vortex transition are roughly near a certain value with small deviation. The current probes connected to Py ring are not arranged at symmetric positions on the ring, and hence the current distribution is not uniform over the entire Py ring. Consequently, the heat generated by current could not be uniform. Therefore, the occurrence of CW and CCW vortex could not occupy the same possibility. Besides, the two different current probe arrangements generate different

thermal distribution over the ring. This could account for the dependence of switching field and chirality upon current probe arrangement.



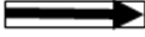

	Full loop	Minor loop	
Measurement 2	# of total acquired loops: 5	Magnetization of Py wire held at positive direction (+) 	Magnetization of Py wire held at negative direction (-) 
		# of total acquired loops: 5	# of total acquired loops: 5
	Three loops exhibit CW-CW loop.	Two loops exhibit CCW-CCW loop.	All loops exhibit CW-CW loop.
Measurement 3	# of total acquired loops: 5	Magnetization of Py wire held at positive direction (+) 	Magnetization of Py wire held at negative direction (-) 
		# of total acquired loops: 5	# of total acquired loops: 5
	Four loops exhibit CCW-CW loop.	One loop exhibit CCW-CCW loop.	All loops exhibit CCW-CW loop

Table 4.4-1 List of distribution of vortex chiralities

4.4.4 Comparison with the wire spin injector

Another wire-ring lateral spin valve was measured as well (Figure 4.4-6), in which the Py wire was set as spin injector, i.e., spin-polarized current was injected from the wire contrary to the previous case discussed. The current direction is indicated by the white arrow shown in Figure 4.4-6. The positive voltage probe was set at 16, and the negative one at 15 ~ 10. Therefore, we can compare the vortex chirality distribution with the previous case. The result (Figure 4.4-7) shows invariant for different probe arrangements.

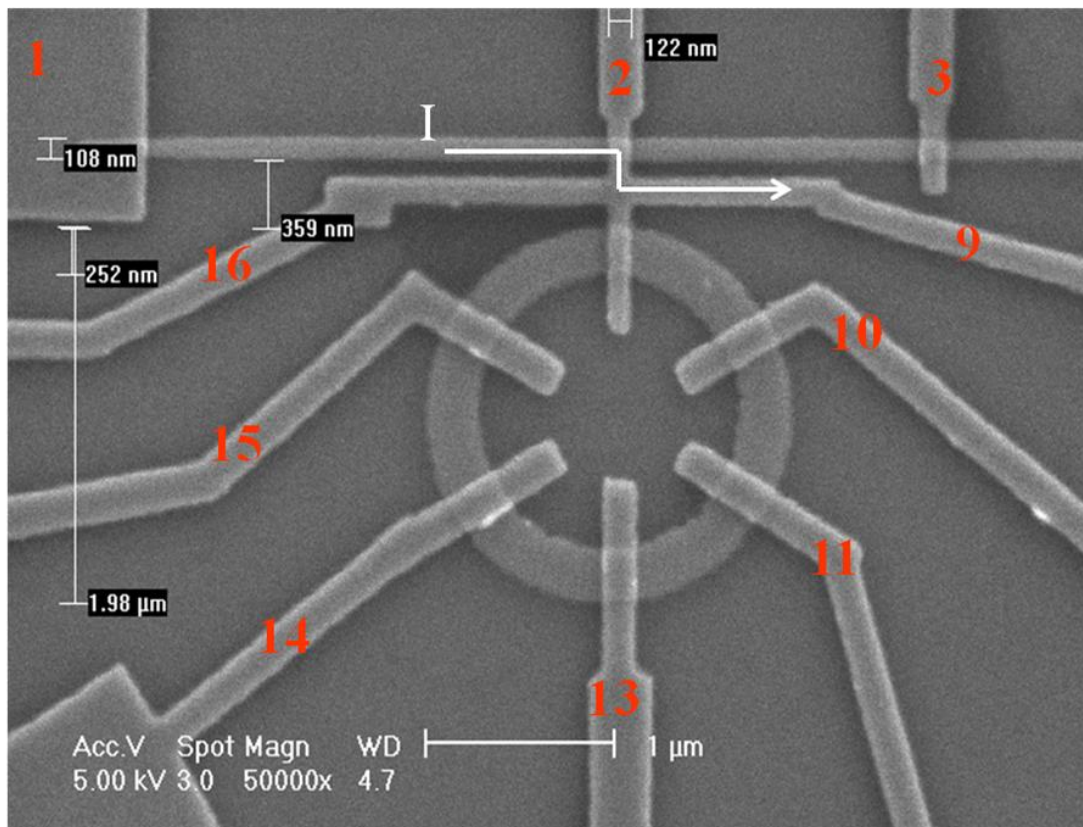


Figure 4.4-6 SEM image of a wire-ring lateral spin valve with multi terminals.

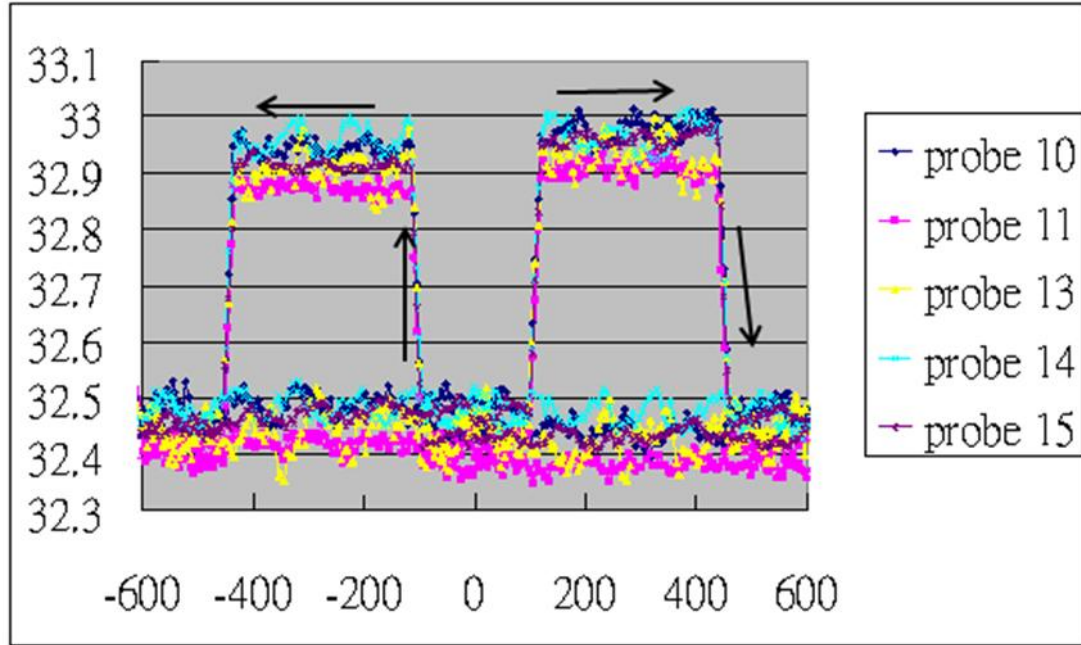


Figure 4.4-7 Results of NLSV measurement for device in Figure 4.4-6. The arrows indicate the sweeping directions.

4.4.5 Vortex chirality detection by local lateral spin valve

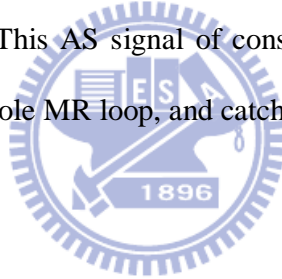
To enhance the spin accumulation signal, we shorten the spin diffusive channel by removing the normal-metal cross inserted between the spin injector and detector. By doing so, the geometry of nonlocal measurement is then equivalent to these cases [2-4]. Unfortunately, the closed-curve feature of ring complicates the fabrication to connect one of the two voltage probes with spin-diffusive channel. One solution, which is no longer in nonlocal one, is to connect a voltage probe with the ferromagnetic wire (spin injector) instead of directly with the diffusive channel, i.e., the spin injector itself serves as a voltage probe (Figure 4.4-8(b)). Hence, the signal of spin accumulation can still be indirectly sensed through one more F/N contact region within the charge current flows. To simplify the description, we temporarily name this electrode configuration as “alternative” device to distinguish it from the nonlocal one.

Figure 4.4-9 shows the MR measurement of an alternative device. To characterize the

respect switching fields of the wire and the ring, conventional AMR (Figure 4.4-9(b)) of the individual ring were also measured to compare with Figure 4.4-9(a). Although detailed comparison and magnetic reversal process of the wire-ring device has been discussed in the previous section and in its references, here we still give a brief description. From AMR curve in Figure 4.4-9(b), the onion-to-vortex switching is about 150 Oe which is indicated by vertically dotted lines in Figure 4.4-9(a) in which the MR loop reveals only two switching fields 420 Oe and 465 Oe. Since the vortex-to-reverse-onion switching was not clearly in full AMR loop, we also measured minor loops (Figures 4.4-9(c) and (d)) to approach the switching field. The results suggest that the vortex-to-reverse-onion switching field is 465 Oe, so that of the wire is 420 Oe. The whole reversal process of the device is sequentially shown in Figure 4.4-9(e). After released from positive saturation, state 1 is in **P** configuration. When field sweeps to -150 Oe, the ring changes into vortex state in counter clockwise (CCW) with the wire not reversed (state 2), hence the spin valve is still in **P** configuration and the resistance maintains unchanged. The MR then increases by $0.275 \pm 0.04 \text{ m}\Omega$ after the wire reversed (-420Oe) with the ring maintaining CCW, and is in **AP** configuration. (state 3) After field exceeding -465 Oe, the ring switches to reverse onion state. MR then changes back to **P** (state 4), and the resistance increases by $0.256 \pm 0.045 \text{ m}\Omega$. For the negative sweep, the observed switching fields are roughly the same with the former, and the vortex can be determined as clockwise (CW) at states 5 and 6. The resistance change is $-0.52 \pm 0.045 \text{ m}\Omega$ from state 5 to 6, and $0.2 \pm 0.04 \text{ m}\Omega$ from state 6 back to 1. Since the switching from state 6 to 1 and 3 to 4 both indicate from **AP** to **P** and has roughly the same MR change, we could roughly consider the spin accumulation signal as 0.2~0.256 mΩ. Besides, both two switches of **AP** to **P** do not contain the switching of spin injector; hence the signal of $0.52 \pm 0.045 \text{ m}\Omega$ could be caused by the reverse of the injector. Therefore, we can evaluate other figures with the above results. From state 2 to 3, the

resistance was to decrease by $0.2\sim 0.256\text{ m}\Omega$ due to spin accumulation, to increase by $0.52 \pm 0.045\text{ m}\Omega$ caused by injector switching from positive to negative direction. The summation is $0.264\sim 0.32\text{ m}\Omega$, roughly fits the measured figure $0.275 \pm 0.04\text{ m}\Omega$. The other evaluation for that from state 5 to 6 is also in agreement. Despite of a minor AS difference about $50\sim 60\ \mu\Omega$, we could still roughly characterize a major AS signal ($0.52\text{ m}\Omega$) caused by the spin injector reverse and a major symmetric spin valve signal ($0.2\sim 0.256\text{ m}\Omega$) originated by spin accumulation in the present alternative device.

In this section, we have demonstrated the measurement of lateral spin valve in an alternative geometry, and clearly determine the vortex chiralities of the magnetic ring. Beside the spin accumulation signal, an AS Hall-like signal related to the switching of spin injector is sensed as well. This AS signal of considerable magnitude contributes a significant constitution of the whole MR loop, and catches our intention to explore.



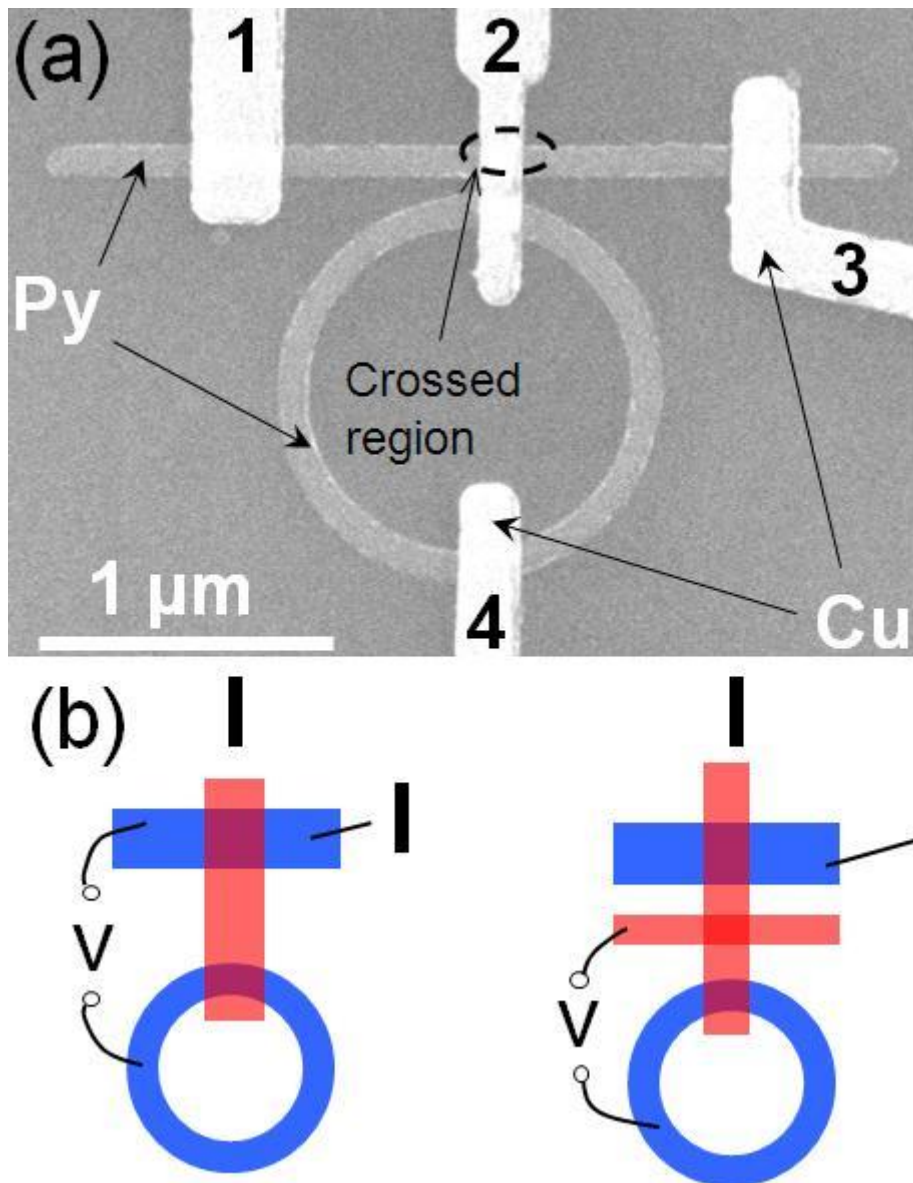


Figure 4.4-8 (a) SEM image of wire-ring spin valve. The numbers indicates the four terminals. (b) Schematic illustrations of the two different voltage probe arrangements. Left: alternative geometry, right: the conventional nonlocal geometry as in the previous section.

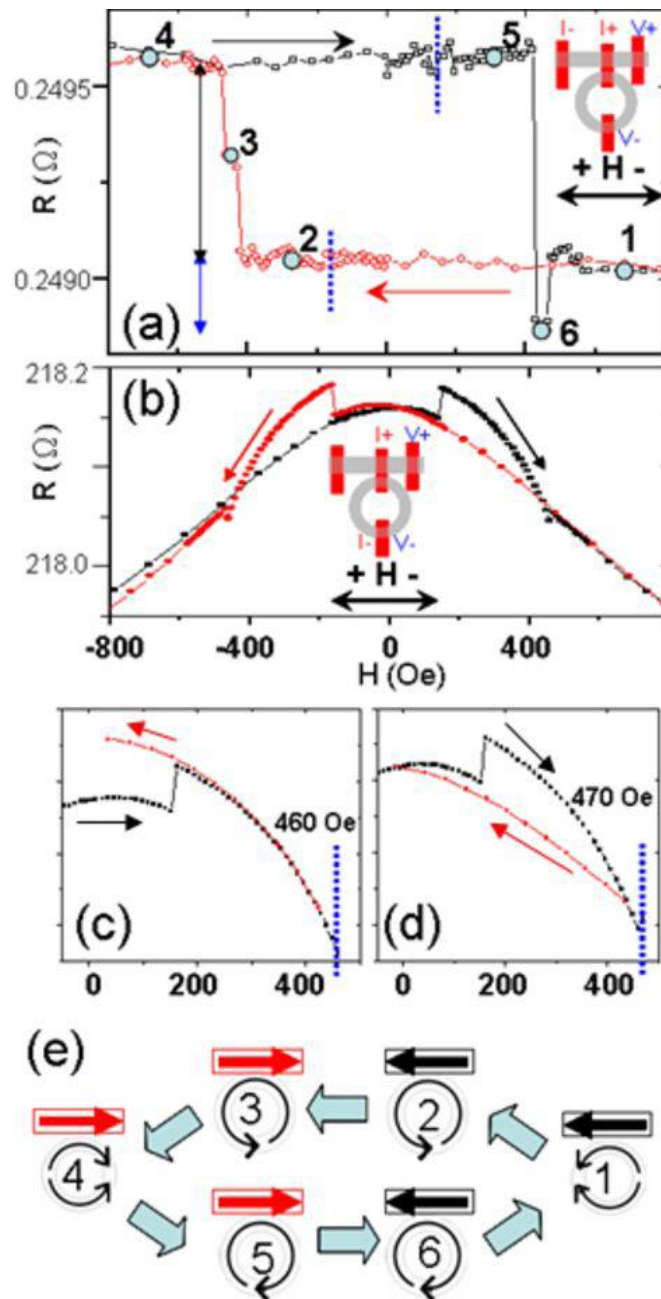


Figure 4.4-9 MR measurement of a wire-ring device. The thickness is 22nm for Py, and the width is 120 nm for the wire and 150 nm for the ring with an outside diameter of 1.7 μm . The wire-ring space is about 40nm, and is bridged by a diffusive channel (Cu) with 170nm in width and 50nm in thickness. (a) Measurement in alternative arrangement with DC current $500 \mu\text{A}$. The numbers indicate each magnetic state in accordance with that in (e). The inset illustrates electrodes arrangement and the relative direction of applied field. (b) Measurement of conventional AMR for the ring, with DC current $20 \mu\text{A}$. (c) and (d) Minor loops to approach the switching field from vortex state to reverse vortex state. Before switching (c), and after switching (d). (e) schematic illustrations for the reversal process of the device. The numbers are in accordance with that in (a).

4.5 Observation of Hall-like signal in all-metal lateral spin valve

At the end of section 4.4, we encountered a considerable magnitude of asymmetric signal mixed with spin accumulation one that we purposely explored and observed. This measurement geometry is, actually, no longer the nonlocal arrangement, since charge current flows through the crossed region and the two electrodes are just in contact in this region through which electric current flows. To further explore the hybrid phenomena, we simplified the device by replacing the ring by another FM wire, and three sorts of voltage arrangements were applied to the measurements. The narrower FM wire with higher switching field was chosen as spin injector, and the wider one as detector. The first arrangement is typically nonlocal geometry which was supposed to show only symmetric spin valve signal from spin accumulation. As the result shown in Figure 4.5-1(a), on the contrary, it reveals not only symmetric spin valve MR loop, but combined with a minor AS signal. The spin valve signal is about $0.342 \pm 0.02 \text{ m}\Omega$, and the minor AS signal $0.041 \pm 0.02 \text{ m}\Omega$ is caused by the switching of the detector. The second arrangement was to change one voltage probe from the detector to the injector, and the result (Figure 4.5-1(b)) shows almost only major AS loop. The two obvious switching fields indicate the reverse of the spin injector. Cause of the noisy frustration, however, we could not be sure if there are any other signals caused by the reverse of the spin detector. The major AS signal in this arrangement is $0.212 \pm 0.02 \text{ m}\Omega$. We finally discuss the case of the alternative arrangement (Figure 4.5-1(c)). Not surprisingly, both a major AS signal and a major symmetric spin valve one are detected, and a minor AS signal is accompanying like that for the wire-ring devices mentioned previously. Referring to the results from the first two arrangements, we can make a more clear evaluation for this arrangement. At the switching from state 1 to 2, the MR value was supposed to decrease by $0.342 \pm 0.02 \text{ m}\Omega$ due to spin valve from **P** to **AP**, and to increase

by $0.041 \pm 0.02 \text{ m}\Omega$ due to the reverse of the detector from positive to negative. The summation is to decrease by $0.301 \pm 0.02 \text{ m}\Omega$ in accord with the measured $0.296 \pm 0.025 \text{ m}\Omega$. From state 2 to 3, it was to increase by $0.342 \pm 0.02 \text{ m}\Omega$ caused by switching from **AP** to **P** and $0.212 \pm 0.02 \text{ m}\Omega$ due to the reverse of the injector from positive to negative direction. The summation is $0.554 \pm 0.02 \text{ m}\Omega$ roughly in accordance with $0.548 \pm 0.035 \text{ m}\Omega$ measured. The other evaluations are also roughly in good agreement. Therefore, it is reasonable to explain that the minor AS signal roughly $50\sim 60 \mu\Omega$ in the previous wire-ring devices is caused by the switching of the detector. Since a major AS signal is only caused by the spin injector in lateral spin valve when the injector itself serves as a voltage probe, we then removed the detector, and leaved only injector to compare with the spin vale. The result (Figure 4.5-1(d)) fits our speculation, showing the same AS MR loop as in Figure 4.5-1(b).

In this section, we have successfully extracted the AS signals from the combined lateral spin valve, although the physical origin for these AS signals is still not clear. Since the major AS signal is caused by switching of single FM wire only, it is our interest to further explore this phenomenon by changing widths of FM and Cu (in section 4.6). As the minor AS signals existed in nonlocal measurement, it is doubted that the interface between FM and Cu is clean enough in our fabrication process, since many studies on this arrangement of nonlocal measurement have been achieved and such minor AS signal has not been repoted.

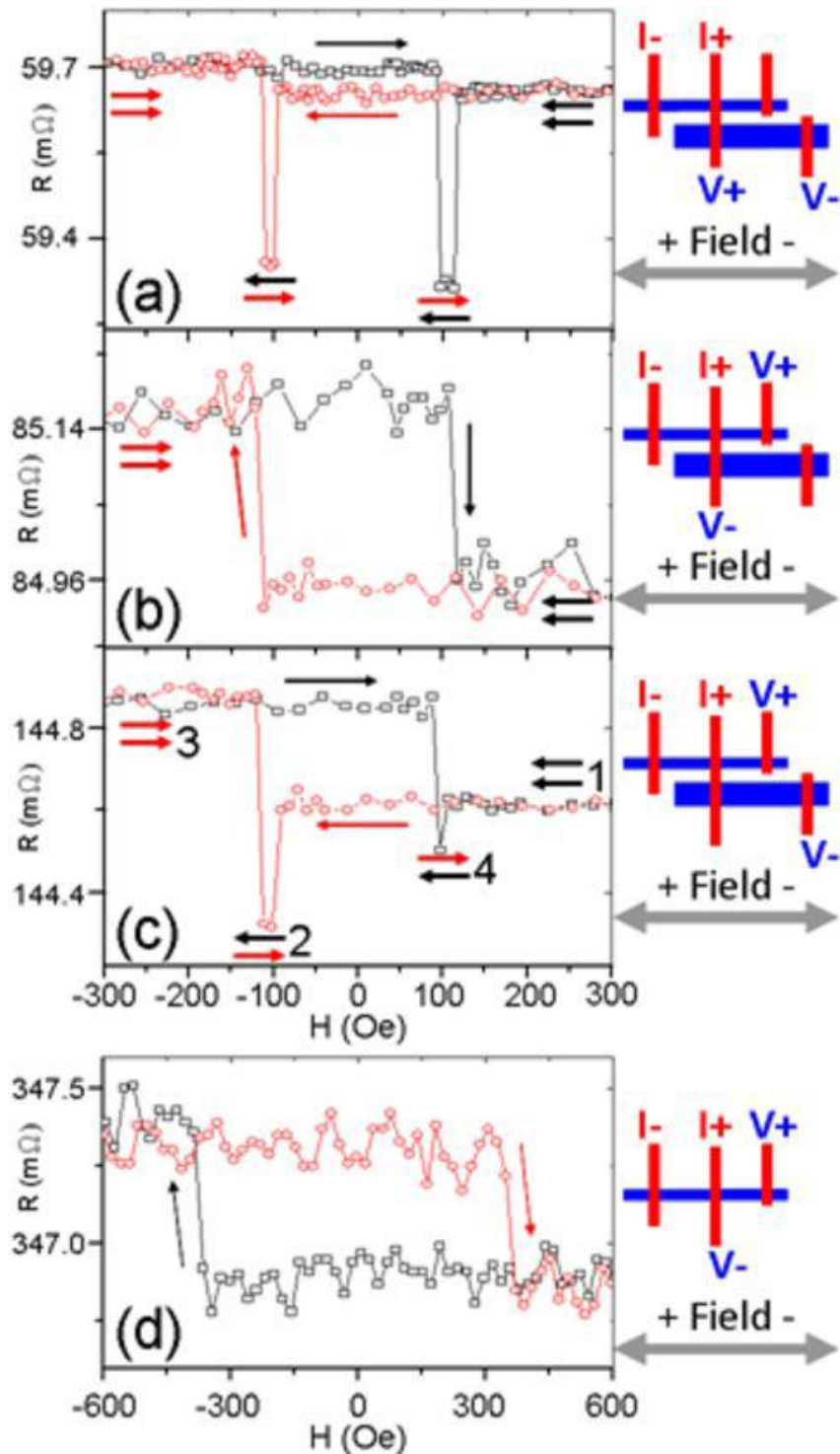


Figure 4.5-1 MR measurement of the same one two-wire device [(a)~(c)] with DC 500 μ A. The thickness is 20nm for Py, and the width is 110 nm for the injector and 200 nm for the detector. The space is about 85nm. The diffusive channel is 210 nm in width and 66nm in thickness. (a) Nonlocal arrangement. (b) Arrangement without voltage probe contact on the detector. (c) Alternative arrangement. (d) MR measurement of single Py wire with AC 150 μ A. The Py wire is 30 nm in thickness and 220 nm in width. Diffusive channel is 44 nm in thickness and 200 nm in width.

4.6 Observation of Anomalous Hall effect in Cu-Py-crossed structure with in-plane magnetization

4.6.1 Proposal of Cu-Py-crossed four-terminal Hall device

As mentioned at the end of section 4.5, the MR loop of the “alternative” arrangement contains an extra and odd-symmetric hysteretic loop that is not observed in NLSV arrangement. It is reasonable to understand that this extra signal is from the Cu/Py contact area, in which, charge current flows through and some related effects such as AMR, PHE, and Hall effect may be sensed. The similar odd-symmetric hysteretic loop has been observed and named by Jedema et al. [47] as “contact” MR. The authors attributed this MR behavior to the local Hall effect at Cu/Co contact area, but the detailed geometry describing how the Hall voltage is generated and detected is not clear. In this work, taking the advantage of simplicity of fabricating Cu-Py-crossed structure, we extend the concept of Jedema’s “contact” MR to propose a four-terminal bipolar device, which is an identical geometry with the “contact” one in MR measurement and detects Hall signal based on in-plane magnetization in Py wire. We also propose a detailed geometry on how the Hall voltage is induced and detected. The variation of resistance change, ΔR , was examined by changing size of Cu and Py wires. By considering the current shunt in the proposed geometry, Hall resistance was estimated by referencing ordinary Hall coefficient of Cu and anomalous Hall coefficient of Py, and was compared with the measured ΔR .

Figure 4.6-1(a) shows the three-dimensional geometry of the Cu-Py-crossed structure. In the original geometry of Jedema’s “contact” measurement illustrated in Figure 4.6-1(b), the direction of applied field is defined opposite to that of the present work; and the ferromagnet wire itself serves as negative voltage electrode, also opposite to the present work. Hence, the measured polarities of voltage are in the

same sign for the two geometries. That is, these two geometries are identical in MR measurement, and exhibit the same configuration of MR loop. The only difference is that an extra charge-current-induced voltage drop across a length of Cu is detected in the original “contact” geometry, but the voltage drop does not contribute to the magnitude of ΔR .

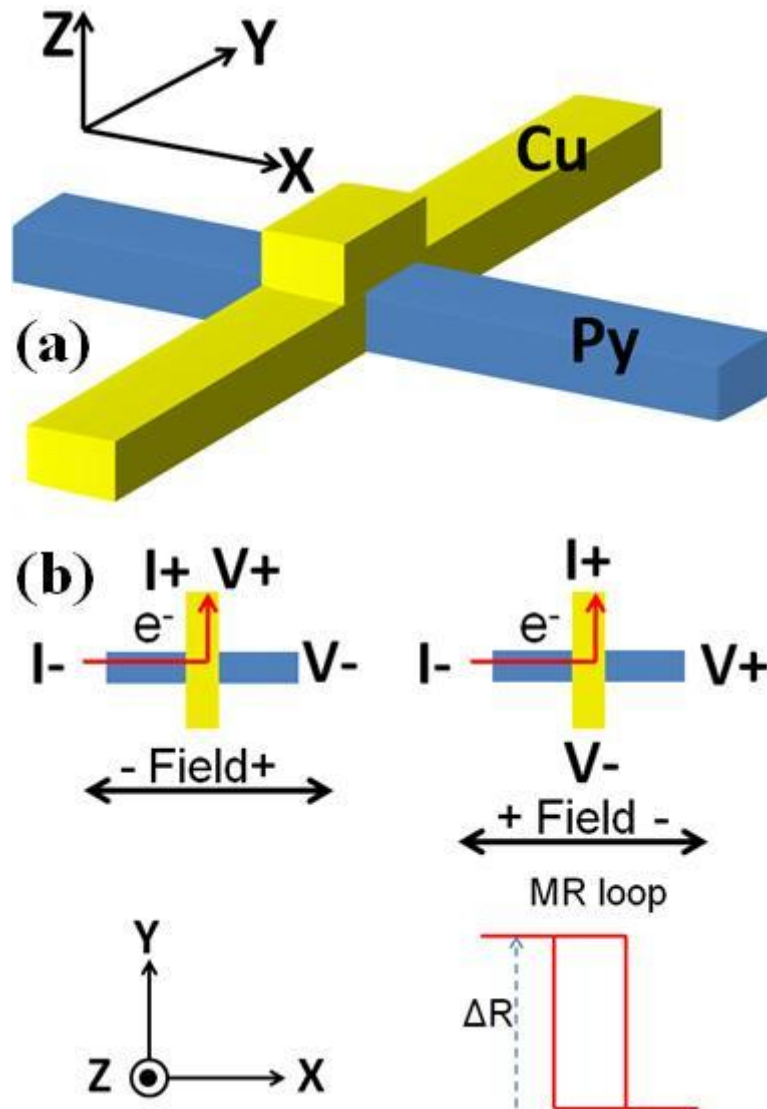


Figure 4.6-1 (a) 3D geometry of Cu-Py-crossed structure. The direction is denoted by the 3D coordinate. (b) Top view of the device. Upper-left: the original geometry of Jedema’s “contact” measurement. Upper-right: geometry in the present work. All the directions are relative to the coordinate (bottom-left). Bottom-right: Schematic MR loop. Both geometries exhibit the same configuration of this MR loop. ΔR is defined as the difference in resistance between positive and negative magnetization at 0 Oe.

4.6.2 Observation of size-dependent ΔR

The typical MR loop of the 4-terminal bipolar device with applied field aligned to Py wire is shown in Figures 4.6-2(a) and (b). With the direction of current reversed, the polarity of measured voltage also reverses. The clear switching indicates the reverse of magnetization of Py wire, and the difference in resistance between both remnant states (ΔR) is nonzero. To confirm the nonzero ΔR , resistance was recorded only at 0 Oe with successively alternating the magnetization of Py wire in longitudinal direction. As shown in Figure 4.6-2(c), high and low resistances present in turn with magnetization successively alternated. Current-dependent measurement was also performed to explore the change of ΔR . In Figure 4.6-2(d), the resistance shows no obvious change with current increasing from 75 μA to 500 μA . Hence, the nonzero ΔR exhibits a high reproducibility and linear relationship between current and measured voltage in the current range of 75 μA ~ 500 μA .

Further exploration of the physical origin of nonzero ΔR was to change widths of Cu and Py wires. Figures 4.6-3(a), (b), and (c) show Cu-width-dependent ΔR s for Py wires at three different widths. For all the three widths of Py wires, ΔR presents negative relationship with respect to width of Cu. With merging the three sets of data together (Figure 4.6-3(d)), it shows a roughly reciprocal relation between ΔR and width of Cu without obvious dependence on width of Py wire. Figure 4.6-3(e) shows that ΔR is irrelevant to the width of Py wire for each individual width of Cu, and ΔR s for narrower Cu are higher than that for wider one. This is in agreement with the trend depicted in Figure 4.6-3(d).

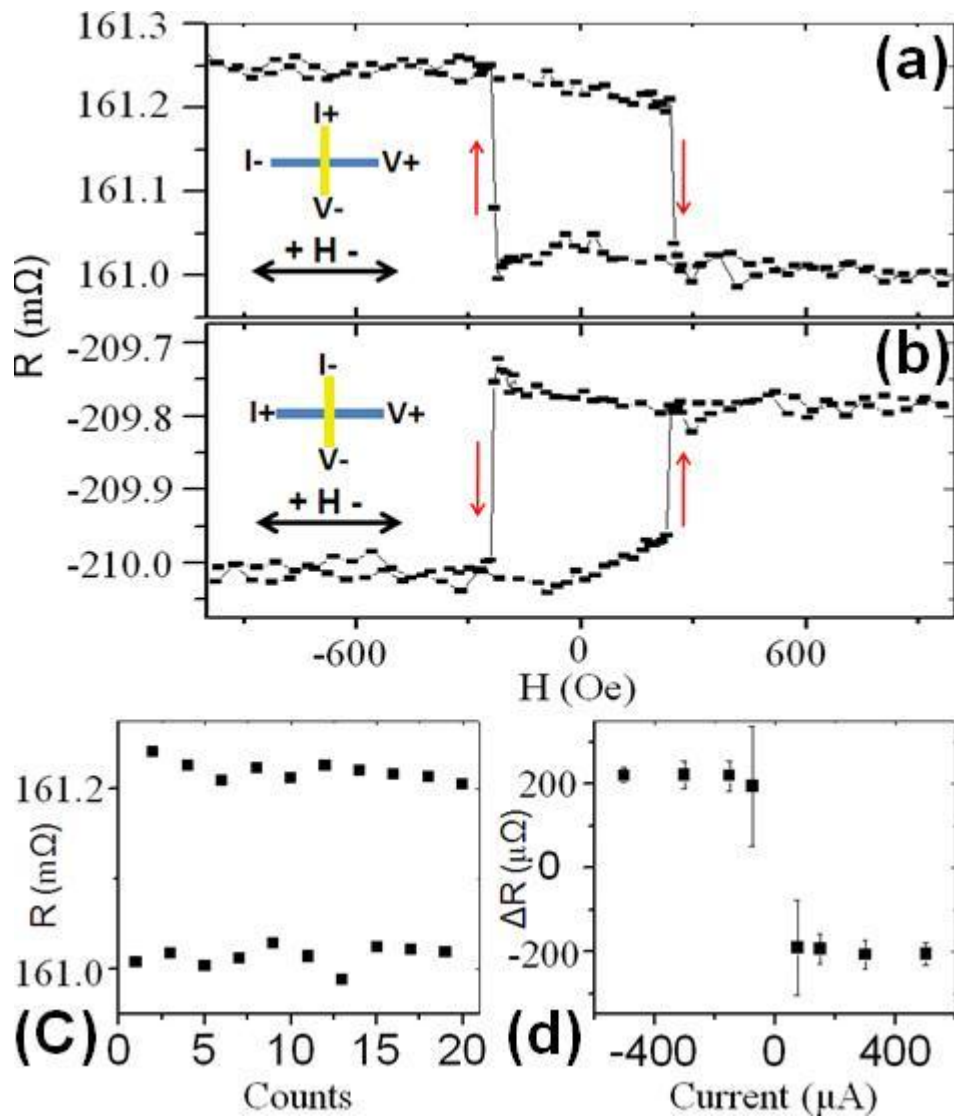


Figure 4.6-2 Measured MR loops of device for positive (a) and negative (b) current. The thickness is 65 nm for Cu, and 31 nm for Py. The insets denote the arrangements of current and voltage probes, and direction of applied field. To clearly present the polarity of measured voltage, resistance is calculated by dividing the measured voltage by the **absolute** value of current, $R=V/|I|$. (c) Resistance recorded at 0 Oe, with successively alternating magnetization of Py. The odd numbers represent positive magnetization, and the evens represent negative one. (d) Current-dependent ΔR .

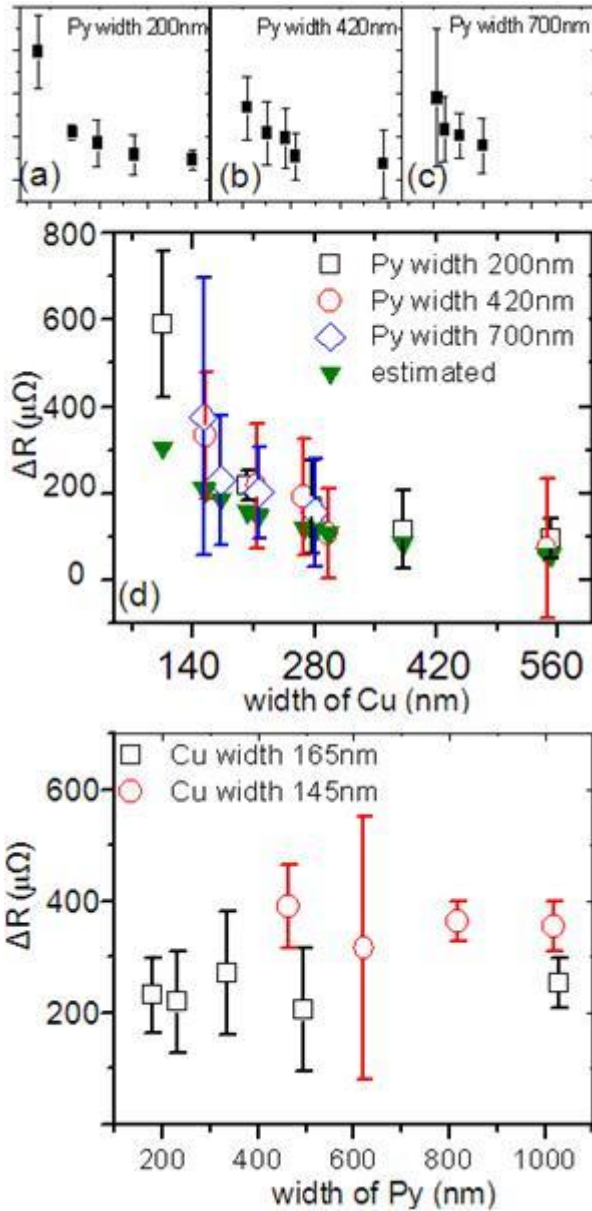


Figure 4.6-3 Cu-width-dependent ΔR s for differently constant widths (a) 200 nm (b) 420 nm and (c) 700 nm of Py wires. (d) Merging all data of (a), (b), and (c). The solid-down triangles represent the estimated values by our roughly simple model. (e) Py-width-dependent ΔR s for differently constant widths (165 nm and 145 nm) of Cu. All the thicknesses are 50 nm for Cu, and 20 nm for Py.

4.6.3 Proposal of the detailed geometry explaining the origin of ΔR

Now we consider the most possible physical origin of ΔR as Hall-like effects. The phenomenological form combining ordinary and anomalous Hall effects for ferromagnet is expressed as [113-115],

$$\rho_H = \alpha_{Hall} H + \alpha_E M(H), \quad (4-1)$$

where ρ_H is the Hall resistivity, B the magnetic induction, and M the magnetization. α_{Hall} is the ordinary Hall coefficient and α_E is the anomalous Hall coefficient which usually is much larger than α_{Hall} . To relate the measured ΔR to the size of Cu and Py, the relation, $\rho_H = R_H t$, is considered. Here R_H is Hall resistance and t the size parameter parallel to H or M . Hence, in the present work, t is the width of Cu. Hall geometry of the device is illustrated in Figure 4.6-4. It should be noticed that, the plot only indicates the **net** charge current components in X, Y, and Z directions at the Cu-Py crossed region (or Cu/Py contact area), but not the real distribution of current density. We propose this assumption based on that the totally combined effect can be considered as a simply linear summation of each local effect caused by the individual current components in all directions per unit volume. In present case, the effective direction is +Y, or -Y. Besides, the ΔR is defined at 0 Oe of external field, and hence the term $(\alpha_{Hall} H)$ in Eq. (4.1) is canceled. Therefore, the Hall relation can be qualitatively described as,

$$\Delta R \propto \frac{1}{W_{Cu}} M_X, \quad (4-2)$$

where W_{Cu} is width of Cu, M_X the magnetization component in X direction at remnant state and slightly smaller than saturation magnitude M_s . As illustrated in the left plot of Figure. 4.6-4, with electron flow in +Y and M_x in -X, positive and negative charges are respectively induced on top and bottom surfaces of Py layer. Hence, the Hall voltage can be measured between Cu electrode on top surface and Py

electrode itself, and the measured resistance is in low level. With magnetization reversed, the Hall voltage changes its sign and resistance switches to high level (Figure. 4.6-4 right). The same effect of sign switching also presents when current is reversed. Note that the induced charges on bottom surface of Py are not detected and hence only half of the generated Hall voltage can be sensed. Moreover, since ΔR is defined as the difference in resistance between positive and negative remnant states, M_x must time a factor of 2 in Eq. (4-2). Therefore, the original form of Eq. (4-2) was $\Delta R \propto \frac{1}{2W_{Cu}} 2M_x$. This detailed geometry clearly indicates that the physical origin of ΔR is mainly caused by AHE in Py at the crossed region (or Cu/Py contact area), and reveals how the induced Hall voltage is measured. To verify this explanation, we performed a simple estimation to examine the measured data.

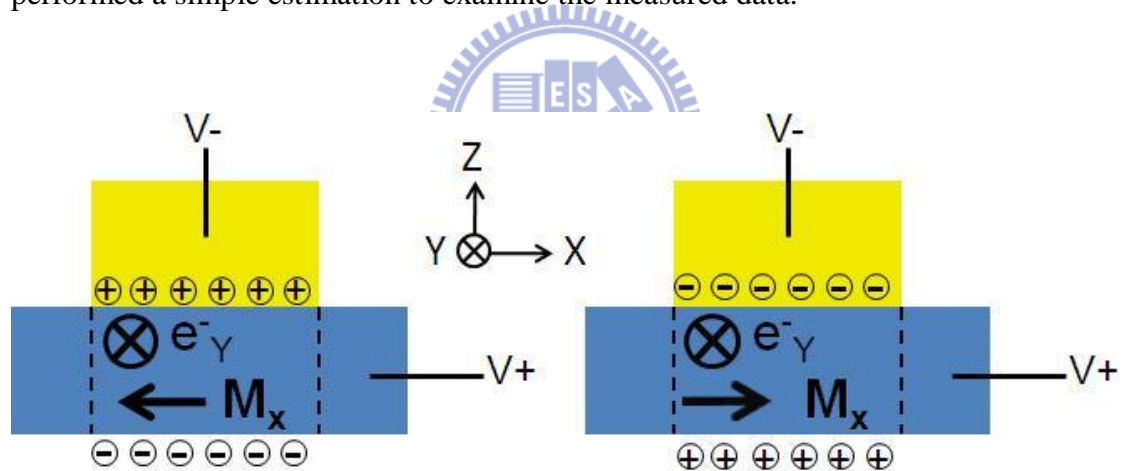


Fig. 4.6-4 Detailed geometry to explain the generated AHE. Left: with electron flow in +Y and M_x in $-X$, positive and negative charges are respectively induced on top and bottom surfaces of Py layer. Right: with M_x reversed, the polarity of charge accumulation also reverses. The horizontal distance between the two vertical dashed lines denotes the width of Cu.

4.6.4 Estimation of AHE in Py

Estimation of Hall resistance is mainly based on the current distribution in the cross region. The very rough but simple model is to consider a parallel resistance including Cu and Py layers, and current distribution simply depends on the widths and the resistivity of both Cu and Py. The ratio of current distributed in the two layers is expressed as,

$$I_{Py}/I_{Cu} = (t_{Py}/t_{Cu})(\rho_{Cu}/\rho_{Py}). \quad (4-3)$$

Here t_{Py} and t_{Cu} are thickness of Py and Cu, respectively. The resistivity, ρ_{Py} and ρ_{Cu} , we measured are about $25 \mu\Omega\text{cm}$ for Py and $3\mu\Omega\text{cm}$ for Cu, respectively. According to Ref. [6], the anomalous Hall coefficient R_s is about $700 \text{ m}\Omega\text{-nm}/\mu_0 M_s$. Here M_s is saturated magnetization of Py.) In present device, by considering Eq. (4-2), the Hall resistance is,

$$R_H = \frac{1}{W_{Cu}} \alpha_E M_s \left(\frac{I_{Py}}{I_{Py} + I_{Cu}} \right). \quad (4-4)$$

Now we estimate an example in Figure 4.6-3, of Cu(50nm)/Py(20nm) and Cu width of 150nm. The estimated value, $(700\text{m}\Omega\text{-nm}/150\text{nm})(1/21)$, is about $0.22 \text{ m}\Omega$, roughly in the same order with the measured $\Delta R = 0.38 \text{ m}\Omega$. Other estimated values were also shown in Figure 4.6-3(d) (the solid-down triangles) to compare with the measured ones. The estimations roughly agree with the measurement at wider Cu, but diverge from that with decreasing width of Cu. This discrepancy indicates that the current fraction in Py does not obey the simple model of parallel resistance. Actually, the current fraction in Py increases with decreasing width of Cu, and one can perform more precise calculation by using finite element model (FEM). The simple model described by Eqs. (4-2) ~ (4-4) provide a qualitative understanding of physical origin of ΔR , and the estimation is roughly in agreement with the measurement (Figure 4.6-3).

4.6.5 Estimation of ordinary Hall effect in Cu

As to the ordinary Hall effect in Cu, we measured the Hall coefficient by applying a perpendicular field to a 50 nm thick Hall cross of Cu, and obtained the coefficient about 1.2 mΩ/10kOe (Figure 4.6-5 left). With the same example mentioned in section 4.6.3, for ordinary Hall effect to result in the ΔR of 0.38mΩ in the Cu of width 150 nm, it required an effective field of magnitude larger than 4500 Oe in positive and negative directions (Figure 4.6-5 right). In spite of the fact that ion-beam milling to clean surface of Py before depositing Cu results in the Cu a little sunk into Py (depth less than 1nm), it is still doubted that the stray field emitted from edges of the trench on Py at the crossed region could reach this magnitude at 0 Oe of external field. Hence, the local Hall effect [117-119] caused by fringe field did not contribute to ΔR in the present device.

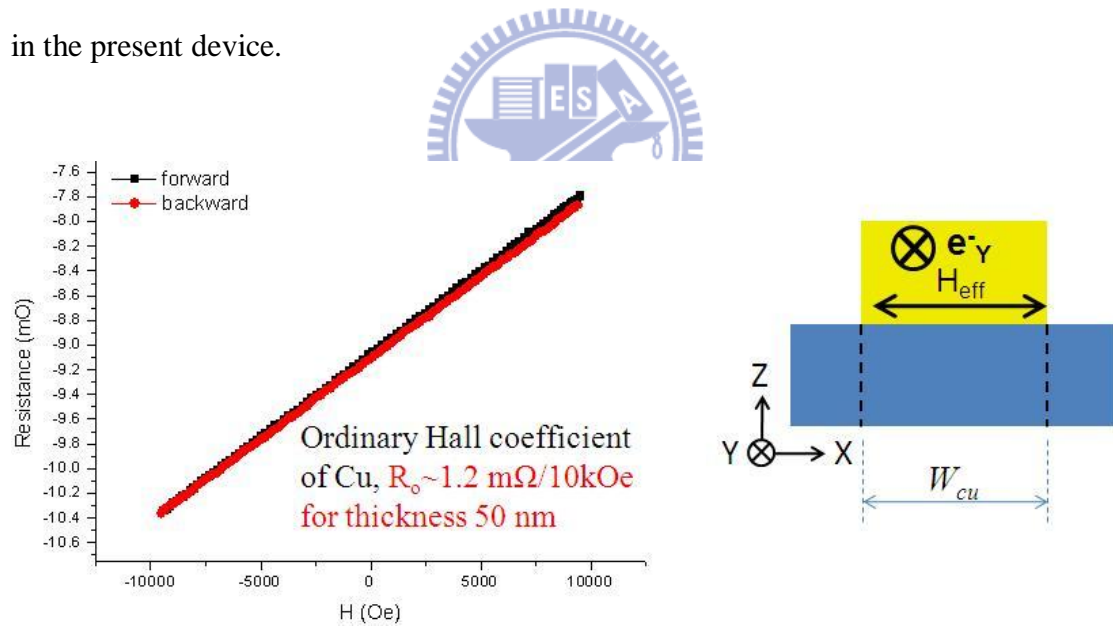


Figure 4.6-5 Left: Measurement of Hall effect of Cu. Right: Geometry illustrating the required effective field for ordinary Hall effect to induce ΔR in Cu.

4.6.6 Estimation of inverse Spin Hall effect (ISHE) in Cu

Figure 4.6-6 (a) shows the top view of the crossed device. Since spin diffuses and relaxes in both +Y and -Y directions, it is reasonable to understand that the decline rate of spin polarization in both directions are roughly equal. Hence, the net value of spin current in Y direction is near zero over the crossed region, and does not contribute to ΔR . Although the Hall angle of Cu is relatively small compared with Pt and Au, the distance (original geometry in Figure 4.6-7) for spin to diffuse from Py and to be measured by voltage electrodes is near zero (Figures 4.6-6 (b) and (c)). This could induce a considerable magnitude of Hall resistance generated by inverse spin Hall effect (ISHE) in Cu. According to Ref [67], the Hall resistance for the present device can be expressed as,

$$\Delta R_{ISHE} = 2\alpha_H \frac{\rho_{Cu}}{W_{Cu}} P \exp(-d/\lambda_{Cu}). \quad (4-5)$$

Here, α_H is the Hall angle, ρ_{Cu} is the resistivity of Cu, W_{Cu} is the width of Cu, P is the effective polarization of spin current (injecting from Py into Cu), d is the distance for spin to diffuse from Py and to be measured by voltage electrodes, and λ_{Cu} is the spin diffusion length in Cu. Again, we estimate the same example mentioned previously. By using P=2%, d=0 (to consider the maxima effect that ISHE could cause), $\rho_{Cu}=3\mu\Omega\text{cm}$, $W_{Cu}=150\text{ nm}$ and $\alpha_H=0.004$, since only half of Hall voltage can be measured, the estimated ΔR_{ISHE} is about $16\ \mu\Omega$, roughly 10 times smaller than that generated by AHE in Py ($220\ \mu\Omega$ for estimated and $380\ \mu\Omega$ for measured).

As a suggestion, one could use materials of high Hall angle such as Pt, Au, or other impurity-doped materials [120] to serve as normal metal in the present device. This normal-metal-ferromagnet-crossed structure can then be a potential tool to study phenomena of spin injection and SHEs with very simple process of lithography to fabricate devices.

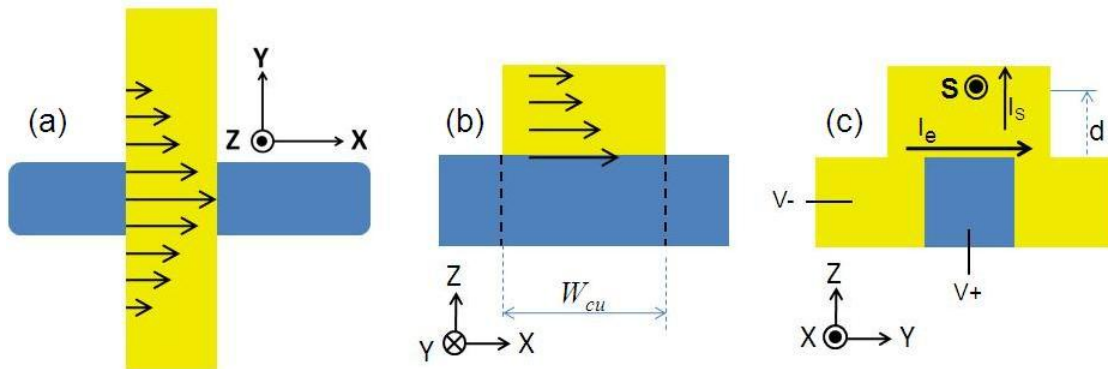


Figure 4.6-6 Geometry of ISHE. (a) Top view. (b) View in X-Z plane. (c) View in Y-Z plane.

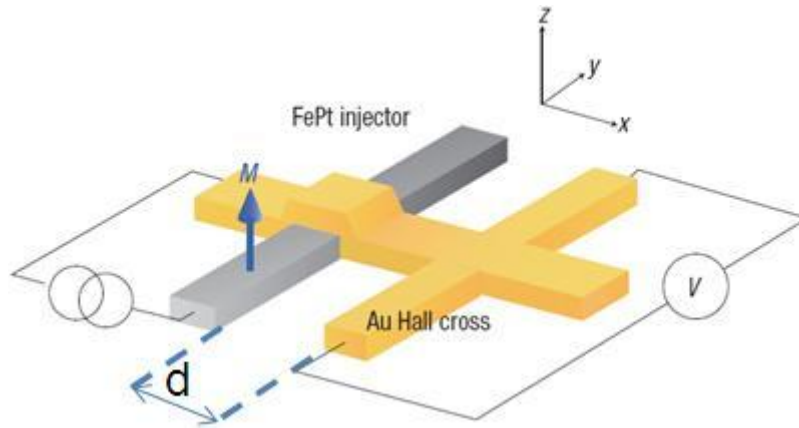


Figure 4.6-7 Geometry of ISHE with perpendicular magnetization and spin-current transport in plane. The \mathbf{d} in plane denotes the distance for spin to diffuse from ferromagnet into diffusive channel (here is Au) and to be sensed by voltage electrodes. After Seki [67].

CHAPTER 5

Conclusions

This dissertation has presented the results of the studies on the spin transports and magnetic reversal behaviors in submicron- and nano-sized magnetic structures by using MFM quantitative analysis and MR measurement. Although the varieties of reversal behaviors complicate the analysis and the characterization of the magnetic states, we can still identify their common features by the fundamental of the phenomena and theory which we have presented in Chapter 2. For the observation of the reversal behaviors, the critical switching field is strongly influenced by the size effect. By taking the two-different-width magnetic strip as the example, the analysis of the three local regions shows an identifiable tendency that large aspect ratio of length to width prefers more stable energy for the ferromagnet to stay at firm state with uniform formation aligned to the long axis. The same result can also be concluded by the MR measurement of the single-layered and tri-layered rings in which the large aspect ratio enhances the formation of the onion states. Interestingly, when we consider the two apparently different geometric patterns of straight line in uniform state and ring in onion state, reversal behaviors of the two states are dominated by the same shape anisotropy of narrow wires. For the spin transport, however, the understanding of spin-dependent tunneling in MTJ has a considerable discrepancy with the spin-dependent scattering in CIP GMR (as the tri-layered rings). Despite of their common phenomenon of spin polarization in ferromagnet, the transport mechanism still requires a more fundamental understanding. Finally, we summarize some important results as following:

The magnetic behaviors in different local sections of the patterned strip wire can be individually separated and compared with each other. The intensity of the phase-shift

in the wider end is stronger than that in the narrower one. In contrast, the coercive force (defined by the reverse in the signs of the values of phase-shifts) in the narrower end (9 Oe) is larger than that in the wider one (8 Oe). This is due to a strong anisotropic effect, and thus the H_c in the neck section could become strongly affected by the competition of the head-to-tail magnetic configurations in the two parts of the strip wire. This results in a small H_c in the neck section.

For the thermal effect measurement of the MTJs, the MR ratio at 140 °C can still remain roughly 87% of that at room temperature. Generally speaking, in application, the local higher temperature which an electronic equipment can achieve is around 60–80 °C while operating, so the MR ratio of the MTJs at the operating situation maintains a considerable portion (90–95%) of that at room temperature.

The critical current density of current-induced domain wall motion in the single-layered Py ring is about $1.5 \sim 3.5 \times 10^7$ A/cm², roughly the same order with the typical results from others. With the present size, the tri-layered spin valve is possibly in the critical boundary between the formations of vortex and onion, since the intermediate state appears occasionally between configurations 1 and 2. Within this state, the soft ring is in vortex state and the hard one the forward onion state.

The spin polarization induced in Cu diffusive channel of the NLSV devices in the present work can be estimated as about 2%, roughly in agreement with other investigations. The spin signals are also enhanced by shortening the distance of the diffusive channel.

The odd-asymmetric signals related to the switching of the spin injector at the contact region (the Cu-Py cross) are attributed to the anomalous Hall effect of the injector at the contact region. It has been supported by the results of size dependent investigation.

References

- [1] S. A. Wolf, D. D. Awschalom, R. A. Buhrman, J. M. Daughton, S. von Molnár, M. L. Roukes, A. Y. Chtchelkanova, and D. M. Treger, *Science* **294**, 1488 (2001).
- [2] R. K. Watts, H. M. Darley, J. B. Kruger, T. G. Blocker, D. C. Guterman, J. T. Carlo, D. C. Bullock, and M. S. Shaikh, *Appl. Phys. Lett.* **28**, 355 (1976).
- [3] M. Schneider, H. Hoffmann, and J. Zweck, *Appl. Phys. Lett.* **77**, 2909 (2000).
- [4] J. A. Johnson and M. Grimsditch, V. Metlushko, P. Vavassori, B. Ilic, P. Neuzil and R. Kumar, *Appl. Phys. Lett.* **77**, 4410 (2000).
- [5] F. Giesen, J. Podbielski, T. Korn, M. Steiner, A. van Staa, and D. Grundler, *Appl. Phys. Lett.* **86**, 112510 (2005).
- [6] T. Kimura, Y. Otani, and J. Hamrle, *Appl. Phys. Lett.* **87**, 172506 (2005).
- [7] Luc Thomas, Charles Rettner, Masamitsu Hayashi, Mahesh G. Samant, Stuart S. P. Parkin, Andrew Doran and Andreas Scholl, *Appl. Phys. Lett.* **87**, 262501 (2005).
- [8] Ana-Vanessa Jausovec, Gang Xiong, and Russell P. Cowburn, *Appl. Phys. Lett.* **88**, 052501 (2006).
- [9] S. Schnittger, S. Dreyer, Ch. Jooss, S. Sievers and U. Siegner, *Appl. Phys. Lett.* **90**, 042506 (2007).
- [10] T. Kimura, Y. Otani, H. Masaki T. Ishida, R. Antos and J. Shibata, *Appl. Phys. Lett.* **90**, 132501 (2007).
- [11] J. I. Martin, J. Nogues, Ivan K. Schuller M. J. Van Bael, K. Temst, C. Van Haesendonck, V. V. Moshchalkov, and Y. Bruynseraede, *Appl. Phys. Lett.* **72**, 255 (1998).
- [12] U. Welp, V. K. Vlasko-Vlasov, G. W. Crabtree, Carol Thompson, V. Metlushko, and B. Ilic, *Appl. Phys. Lett.* **79**, 1315 (2001).

- [13] Y. Martin and H. K. Wickramasinghe, *Appl. Phys. Lett.* **50**, 1455 (1987).
- [14] Xiaobin Zhu, P. Gutter, V. Metlushko, and B. Ilic, *Appl. Phys. Lett.* **80**, 4789 (2002).
- [15] J. Lohau, A. Carl, S. Kirsch, and E. F. Wassermann, *Appl. Phys. Lett.* **78**, 2020 (2001).
- [16] Y. C. Chen, Y. D. Yao, S. F. Lee, Y. Liou, J. L. Tsai, and Y. A. Lin, *Appl. Phys. Lett.* **86**, 053111 (2005).
- [17] M. Julliere, *Phys. Lett. A* **54**, 225 (1975).
- [18] E. Y. Tsymbal and D. G. Pettifor: in *Solid State Physics*, ed. H. Ehrenreich and F. Spaepen, Vol, 56 (Academic Press, 2001) pp.113-237.
- [19] J. C. Slonczewski, *Phys. Rev. B* **39**, 6995 (1989).
- [20] *Tunneling Phenomena in Solids*, edited by E. Burstein and S. Lundqvist (Plenum Press, New York, 1969)
- [21] S. Zhang, P. M. Levy, A. C. Marley and S. S. P. Parkin, *Phys. Rev. Lett.* **79**, 3744 (1997).
- [22] Xiu-Feng Han, Andrew C. C. Yu, Mikihiko Oogane, Junichirou Murai, Tadaomi Daibou, and Terunobu Miyazaki, *Phys. Rev. B* **63**, 224404 (2001).
- [23] P. LeClair, H. J. M. Swagten, J. T. Kohlhepp, R. J. M. van de Veerdonk, W. J. M. de Jonge, *Phys. Rev. Lett.* **84**, 2933 (2000).
- [24] P. LeClair, J. T. Kohlhepp, H. J. M. Swagten, W. J. M. de Jonge, *Phys. Rev. Lett.* **86**, 1066 (2001).
- [25] P. LeClair, B. Hoex, H. Wieldraaijer, J. T. Kohlhepp, H. J. M. Swagten, W. J. M. de Jonge, *Phys. Rev. B* **64**, 100406 (2001).
- [26] P. LeClair, J. T. Kohlhepp, C. H. van de Vin, H. Wieldraaijer, H. J. M. Swagten, W. J. M. de Jonge, A. H. Davis, J. M. MacLaren, J. S. Moodera, and R. Jansen, *Phys. Rev. Lett.* **88**, 107201 (2002).

- [27] S. Yuasa, T. Sato, E. Tamura, Y. Suzuki, H. Yamamori, K. Ando and T. Katayama, *Europhys. Lett.* **52**, 344 (2000).
- [28] Chang He Shang, Janusz Nowak, Ronnie Jansen, and Jagadeesh S. Moodera, *Phys. Rev. B* **58**, R2917 (1998).
- [29] Rie Matsumoto, Akio Fukushima, Kay Yakushiji, Shingo Nishioka, Taro Nagahama, Toshikazu Katayama, Yoshishige Suzuki, Koji Ando, and Shinji Yuasa, *Phys. Rev. B* **79**, 174436 (2009).
- [30] Edward McCann, Vladimir I. Fal'ko, *J. Magn. Magn. Mater.* **268**, 123–131 (2004).
- [31] L. Yuan and S. H. Liou, Dexin Wang, *Phys. Rev. B* **73**, 134403 (2006).
- [32] Q. L. Ma¹, S. G. Wang^{1,2}, J. Zhang¹, Yan Wang¹, R. C. C. Ward², C. Wang³, A. Kohn³, X.-G. Zhang⁴, and X. F. Han¹, *Appl. Phys. Lett.* **95**, 052506 (2009).
- [33] Casey W. Miller, Ivan K. Schuller, R. W. Dave, J. M. Slaughter, Yan Zhou, and Johan Åkerman, *J. Appl. Phys.* **103**, 07A904 (2008).
- [34] S. G. Wang, R. C. C. Ward, G. X. Du, X. F. Han, C. Wang, and A. Kohn, *Phys. Rev. B.* **78**, 180411 (R) (2008).
- [35] J. WingberMhle, S. Stein, and H. Kohlstedt, *J. Appl. Phys.* **92**, 7261 (2002).
- [36] P. WIŚNIEWSKI, T. STOBIECKI, M. CZAPKIEWICZ, J. WRONA¹, M. RAMS², C. G. KIM, M. TSUNODA, AND M. TAKAHASHI, *MOLECULAR PHYSICS REPORTS* **40** 192-199 (2004).
- [37] W. F. Brinkman, R. C. Dynes, and J. M. Rowell, *J. Appl. Phys.* **41**, 1915 (1970).
- [38] X. H. Xiang, T. Zhu, J. Du, G. Landry, and John Q. Xiao, *Phys. Rev. B.* **66**, 174407 (2002).
- [39] X. H. Xiang, T. Zhu, G. Landry, J. Du, Yuwen Zhao, and John Q. Xiao, *Appl. Phys. Lett.* **83**, 2826 (2003).
- [40] Janusz Nowak, Dian Song, and Ed Murdock, *J. Appl. Phys.* **87**, 5203 (2000).

- [41] Bryan Oliver and Janusz Nowak, *J. Appl. Phys.* **95**, 546 (2004).
- [42] Nguyen Anh Tuan and Do Phuong Lien, *J. Phys: Conf. Ser.* **187**, 012089 (2009).
- [43] Johan J. Akermana, R. Escuderoa, C. Leightona, S. Kima, D.A. Rabsonb, Renu Whig Davec, J. M. Slaughterc, Ivan K. Schuller, *J. Magn. Magn. Mater.* **240**, 86–91 (2002).
- [44] M. Johnson, R.H. Silsbee, *Phys. Rev. Lett.* **55**, 1790 (1985).
- [45] F.J. Jedema, A.T. Filip, B.J. van Wees, *Nature* **410**, 345 (2001).
- [46] F.J. Jedema, H.B. Heersche, A.T. Filip, J.J. Baselmans, B.J. van Wees, *Nature* **416**, 713 (2002).
- [47] F.J. Jedema, M. S. Nijboer, A.T. Filip, and B.J. van Wees, *Phys. Rev. B* **67**, 085319 (2003).
- [48] Y. Ji, A. Hoffmann, J. S. Jiang, and S. D. Bader, *Appl. Phys. Lett.* **85**, 6218 (2004).
- [49] S. O. Valenzuela, D.J. Monsma, C.M. Marcus, V. Narayanamurti, M. Tinkham, *Phys. Rev. Lett.* **94**, 196601 (2005).
- [50] S. Garzon, I. Zutic, R.A. Webb, *Phys. Rev. Lett.* **94**, 176601 (2005).
- [51] Jang-Hae Ku, Joonyeon Chang, and Hijung Kim, *Appl. Phys. Lett.* **88**, 172510 (2006).
- [52] T. Kimura, J. Hamrle, Y. Otani, K. Tsukagoshi, and Y. Aoyagi, *Appl. Phys. Lett.* **85**, 3501 (2004).
- [53] T. Kimura, J. Hamrle, Y. Otani, K. Tsukagoshi, Y. Aoyagi, *Appl. Phys. Lett.* **85**, 5382 (2004).
- [54] T. Kimura, J. Hamrle, Y. Otani, K. Tsukagoshi, Y. Aoyagi, *Appl. Phys. Lett.* **85**, 3795 (2004).
- [55] T. Kimura, J. Hamrle, Y. Otani, *J. Appl. Phys.* **97**, 076102 (2005).

- [56] T. Kimura, J. Hamrle, Y. Otani, Phys. Rev. B **72**, 014461 (2005).
- [57] T. Kimura, Y. Otani, J. Hamrle, Phys. Rev. B **73**, 132405 (2006).
- [58] Ryan Godfrey and Mark Johnson, Phys. Rev. Lett **96**, 136601 (2006).
- [59] T. Kimura, Y. Otani, Phys. Rev. Lett **99**, 196604 (2007).
- [60] T. Kimura, Y. Otani, J. Hamrle, Phys. Rev. Lett. **96**, 037201 (2006).
- [61] M. V. Costache, M. Zaffalon, and B. J. van Wees, Phys. Rev. B **74**, 012412 (2006).
- [62] A. Fert and I. A. Campbell, J. de Physique, Collques **32**, C1-C46 (1971).
- [63] P. C. van Son, H. van Kempen, and P. Wyder, Phys. Rev. Lett. **58**, 2271 (1987).
- [64] T. Valet and A. Fert, Phys. Rev. Lett. **48**, 7099 (1993).
- [65] T. Kimura, Y. Otani, T. Sato, S. Takahashi, and S. Maekawa, Phys. Rev. Lett. **98**, 156601 (2007).
- [66] Laurent Vila, T. Kimura, and YoshiChika Otani, Phys. Rev. Lett. **99**, 226604 (2007).
- [67] Takeshi Seki, Yu Hasegawa, Seiji Mitani, Saburo Takahashi, Hiroshi Imamura, Sadamichi Maekawa, Junsaku Nitta & Koki Takanashi, *Nature Materials* **7**, 125-129 (2008).
- [68] M.I. D'yakonov and V. I. Perel, Phys. Rev. Lett. **35**, 459 (1971).
- [69] J. E. Hirsch, Phys. Rev. Lett. **83**, 1834 (1999).
- [70] S. Zhang, Phys. Rev. Lett. **85**, 393 (1999).
- [71] Stuart S. P. Parkin, Masamitsu Hayashi and Luc Thomas, *Science* **320**, 190 (2008).
- [72] Stuart S. P. Parkin, Masamitsu Hayashi and Luc Thomas, *Science* **320**, 209 (2008).
- [73] D. A. Allwood, Gang Xiong, M. D. Cooke, C. C. Faulkner, D. Atkinson, N. Vernier, and R. P. Cowburn *Science* **296**, 2003 (2002).

- [74] D. A. Allwood, Gang Xiong, C. C. Faulkner, D. Atkinson, D. Petit, and R. P. Cowburn *Science* **309**, 1688 (2005).
- [75] Dorothée Petit, Ana-Vanessa Jausovec, Huang T. Zeng, Emma Lewis, Liam O'Brien, Dan Read, and Russell P. Cowburn, *Appl. Phys. Lett.* **93**, 163108 (2008).
- [76] M. Kläui, C. A. F. Vaz, J. A. C. Bland, W. Wernsdorfer, G. Faini, and E. Cambril, *Appl. Phys. Lett.* **81**, 108 (2002).
- [77] M. Kläui, C. A. F. Vaz, J. A. C. Bland, W. Wernsdorfer, G. Faini, and E. Cambril, *J. Appl. Phys.* **81**, 108 (2002).
- [78] M. Kläui, C. A. F. Vaz, W. Wernsdorfer, E. Bauer, S. Cherifi, S. Heun, A. Locatelli, G. Faini, E. Cambril, L. J. Heyderman, and J. A. C. Bland, *Physica B* **343**, 343 (2004).
- [79] Dennis Ilgaz, Mathias Kläui, Lutz Heyne, Olivier Boulle, Fabian Zinser, Stephen Krzyk, Mikhail Fonin, Ulrich Rüdiger, Dirk Backes, and Laura J. Heyderman, *Appl. Phys. Lett.* **93**, 132503 (2008).
- [80] M. Kläui, C. A. F. Vaz, J. A. C. Bland, W. Wernsdorfer, G. Faini, E. Cambril, and L. J. Heyderman, *Appl. Phys. Lett.* **83**, 105 (2003).
- [81] M. Kläui, C. A. F. Vaz, J. A. C. Bland, W. Wernsdorfer, G. Faini, E. Cambril, L. J. Heyderman, F. Nolting, and U. Rüdiger, *Phys. Rev. Lett.* **94**, 106601 (2005).
- [82] M. Yamanouchi, D. Chiba, F. Matsukura and H. Ohno, *Nature (London)* **428**, 539 (2004).
- [83] A. Yamaguchi, T. Ono, S. Nasu, K. Miyake, K. Mibu, and T. Shinjo, *Phys. Rev. Lett.* **92**, 072205 (2004).
- [84] N. Vernier, D. A. Allwood, D. Atkinson, M. D. Cooke and R. P. Cowburn, *Europhys. Lett.* **65**, 526 (2004).
- [85] A. Yamaguchi, S. Nasu, H. Tanigawa, T. Ono, K. Miyake, K. Mibu, and T.

- Shinjo, Appl. Phys. Lett. **86**, 012511 (2005).
- [86] J. Grollier, P. Boulenc, V. Cros, A. Hamzić, A. Vaurès, A. Fert, and G. Faini, Appl. Phys. Lett. **83**, 509 (2003).
- [87] J. Grollier, P. Boulenc, V. Cros, A. Hamzić, A. Vaurès, A. Fert, and G. Faini, J. Appl. Phys. **95**, 6777 (2004).
- [88] C. K. Lim, T. Devolder, C. Chappert, J. Grollier, V. Cros, A. Vaurès, A. Fert, and G. Faini, Appl. Phys. Lett. **84**, 2820 (2004).
- [89] J. Grollier, D. Lacour, V. Cros, A. Hamzic, A. Vaurès A. Fert, D. Adam, and G. Faini, J. Appl. Phys. **92**, 4825 (2002).
- [90] S. Laribi, V. Cros, M. Muñoz, J. Grollier, A. Hamzić, C. Deranlot, A. Fert, E. Martínez, L. López-Dáz, L. Vila, G. Faini, S. Zoll, and R. Fournel, Appl. Phys. Lett. **90**, 232505 (2007).
- [91] M. Kläui, C. A. F. Vaz, J. A. C. Bland, L. J. Heyderman, C. David, E. H. C. P. Sinnecker, and A. P. Guimarães, J. Appl. Phys. **95**, 6639 (2004).
- [92] T. A. Moore, T. J. Hayward, D. H. Y. Tse, J. A. C. Bland, F. J. Castaño and C. A. Ross, Physica B **372**, 164 (2006).
- [93] M. Kläui, C.A.F. Vaz, L.J. Heyderman, U. Rüdiger and J.A.C. Bland, J. Magn. Mater. **290-291**, 61 (2005).
- [94] J. Rothman, M. Kläui, L. Lopez-Diaz, C. A. F. Vaz, A. Bleloch, J. A. C. Bland, Z. Cui, and R. Speaks, Phys. Rev. Lett. **86**, 1098 (2001).
- [95] C. A. Ross, F. J. Castaño, D. Morecroft, W. Jung, Henry I. Smith, T. A. Moore, T. J. Hayward, J. A. C. Bland, T. J. Bromwich, and A. K. Petford-Long, J. Appl. Phys. **99**, 08S501 (2006).
- [96] F. J. Castaño, D. Morecroft, W. Jung, and C. A. Ross, Phys. Rev. Lett. **95**, 137201 (2005).
- [97] F. J. Castaño, D. Morecroft, and C. A. Ross, Phys. Rev. B **74**, 224401 (2006).

- [98] T. J. Hayward, J. Llandro, R. B. Balsod, J. A. C. Bland, F. J. Castaño, D. Morecroft, and C. A. Ross, *Appl. Phys. Lett.* **89**, 112510 (2006).
- [99] F J Castaño, B G Ng, I A Colin, D Morecroft, W Jung and C A Ross, *J. Phys. D: Appl. Phys.* **41**, 132005 (2008).
- [100] Chunghee Nam, B. G. Ng, F. J. Castaño, and C. A. Ross, *J. Appl. Phys.* **105**, 033918 (2009).
- [101] Mei-Feng Lai, Zung-Hang Wei¹, Ching-Ray Chang, J. C. Wu, J. H. Kuo, and Jun-Yang Lai, *Phys. Rev. B* **67**, 104419 (2003).
- [102] Zhengqi Lu, Yun Zhou, Yuqing Du, Roy Moate, David Wilton, Genhua Pan, Yifang Chen, and Zheng Cui, *Appl. Phys. Lett.* **88**, 142507 (2006).
- [103] Chunghee Nam, B. G. Ng, F. J. Castaño, M. D. Mascaro, and C. A. Ross, *Appl. Phys. Lett.* **94**, 082501 (2009).
- [104] T. Kimura, Y. Otani, and J. Hamrle, *J. Appl. Phys.* **101**, 126102 (2007).
- [105] M. Brands, G. Dumpich, *J. Phys. D* **38**, 822–826 (2005).
- [106] K. J. Kirk, J. N. Chapman, S. McVitie, P. R. Aitchison, C. D. W. Wilkinson, *Appl. Phys. Lett.* **75**, 3683 (1999).
- [107] S. Y. Yuan, H. N. Bertram, J. F. Smyth, S. Schultz, *IEEE Trans. Magn.* **28**, 3171 (1992).
- [108] B. D. Cullity, "Introduction to Magnetic Materials" (1972).
- [109] J. S. Moodera, L. R. Kinder, T. M. Wong, and R. Meservey, *Phys. Rev. Lett.* **74**, 3273 (1995).
- [110] W. Wulfhekel, H. F. Ding, and J. Kirschner, *J. Magn. Magn. Mater.* **242-245**, 47 (2002).
- [111] W. A. Harrison, *Phys. Rev.* **123**, 85 (1961).
- [112] E.H. Hall: "On a New Action of the Magnet on Electric Currents" *American Journal of Mathematics* **2**, 287 (1879).

- [113] M. Volmera, and J. Neamtu, *J. Magn. Magn. Mater.* **272-276**, 1881 (2004).
- [114] F. Y. Ogrin, S. L. Lee, and Y. F. Ogrin, et al., *J. Magn. Magn. Mater.* **219**, 331 (2000).
- [115] A. Gerber, A. Milner, M. Karpovsky, B. Lemke, H. -U. Habermeier, J. Tuaille-Combes, M. Négrier, O. Boisron, P. Mélinon, and A. Perez, *J. Magn. Magn. Mater.* **242-245**, 90 (2002).
- [116] S. P. Li, D. Peyrade, M. Natali, A. Lebib, Y. Chen, U. Ebels, L. D. Buda, and K. Ounadjela, *Phys. Rev. Lett.* **86**, 1102 (2001).
- [117] F. G. Monzon, Mark Johnson and M. L. Roukes, *Appl. Phys. Lett.* **71**, 3087 (1997).
- [118] Jinki Hong, Sungjung Joo, Tae-Suk Kim, Kungwon Rhie, K. H. Kim, S. U. Kim, B. C. Lee, and Kyung-Ho, *Appl. Phys. Lett.* **90**, 023510 (2007).
- [119] Junsaku Nitta, Thomas Schapers, Hubert B. Heersche, Takaaki Koga, Yuuki Sato and Hideaki Takayanagi, *Jpn. J. Appl. Phys.* **41**, 2497 (2002).
- [120] B. Gu, I. Sugai, T. Ziman, G.Y. Guo, N. Nagaosa, T. Seki, K. Takanashi, and S. Maekawa, *Phys. Rev. Lett.* **105**, 216401 (2010).

List of Publications

- [1] “Determining vortex chirality in ferromagnetic ring by lateral nonlocal spin valve” D. C. Chen, Y. D. Yao, J. K. Wu, C. Yu, and S. F. Lee, *J. Appl. Phys.* **103**, 07F312 (2008).
- [2] “Quantitative analysis of magnetization reversal in patterned strip wire by magnetic force microscopy” D. C. Chen, D. P. Chiang, Y. D. Yao*, *J. Magn. Magn. Mater.* **304** 23-26 (2006).
- [3] “High-temperature magnetoresistance study of a magnetic tunnel junction” D. C. Chen, Y. D. Yao, C. M. Chen, James Hung, Y. S. Chen, W. H. Wang, W. C. Chen, M. J. Kao, *J. Magn. Magn. Mater.* **304** e297-e299 (2006).
- [4] “Magnetic switching and reversal process in a tip ring structure” Yung Liou, Dong-Cheng Chen*, Chwen Yu, J. S. Chen, Shang-Fan Lee, Y. D. Yao, C. C. Tzeng, T. Y. Chen, K. W. Cheng, Ron Ma, *J. Appl. Phys.* **95**, 6723 (2004).
- [5] “Variation of magnetization reversal in pseudo-spin-valve elliptical rings” C. Yu, T. W. Chiang, Y. S. Chen, K. W. Cheng, D. C. Chen, S. F. Lee, Y. Liou, J. H. Hsu, and Y. D. Yao, *Appl. Phys. Lett.* **94**, 233103 (2009).
- [6] “Demonstration of edge roughness effect on the magnetization reversal of spin valve submicron wires” T. W. Chiang, L. J. Chang, C. Yu, S. Y. Huang, D. C. Chen, Y. D. Yao, and S. F. Lee, *Appl. Phys. Lett.* **97**, 022109 (2010).
- [7] “Vortex domain wall depinning by polarized current in submicron half-ring wires” Y. S. Chen, K. W. Cheng, C. Yu, S. F. Lee, D. C. Chen, S. H. Wu, M. T. Lin, and Y. Liou, K. T. Wu, Y. D. Yao, *J. Appl. Phys.* **99**, 08G516 (2006).